UCRL-ID-120758

Configuring the National Ignition Facility for Direct-Drive Experiments

July 1995

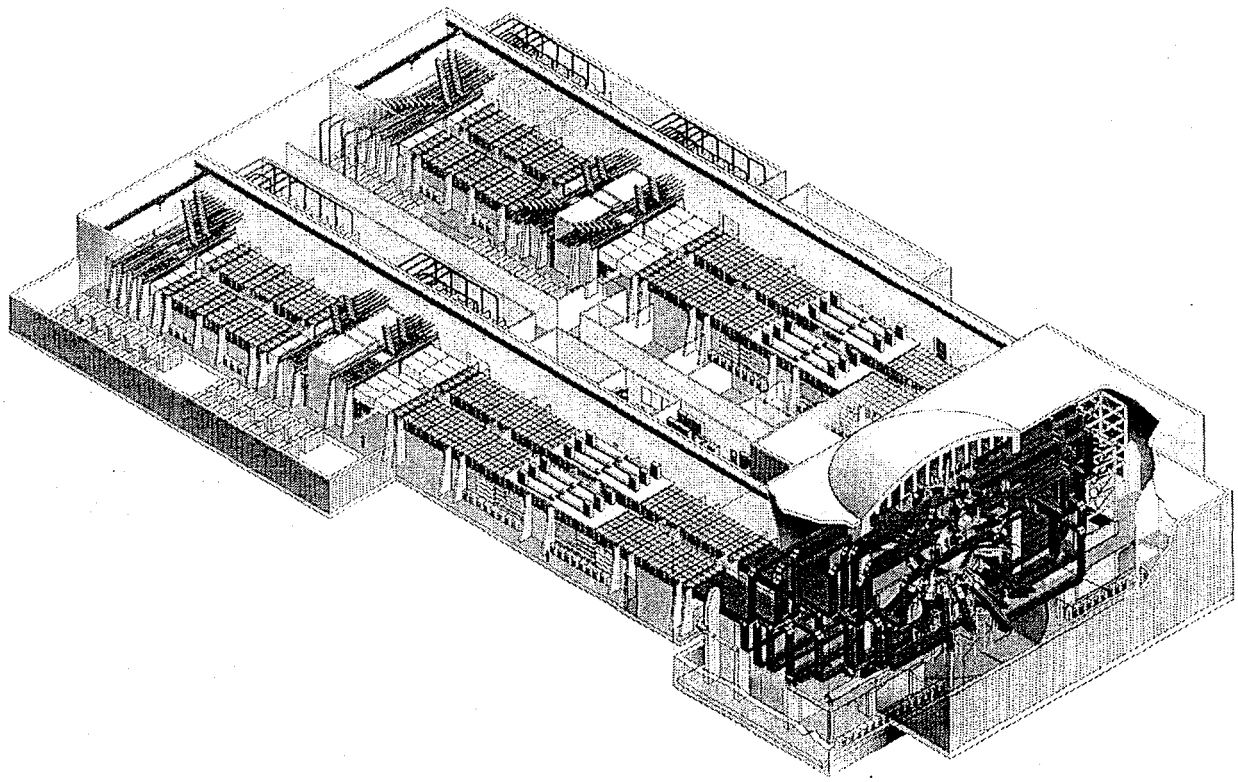

Lawrence Livermore
National Laboratory

DISCLAIMER

Work performed under the auspices of the U.S. Department of Energy by Lawrence Livermore National Laboratory under Contract W-7405-Eng-48.

UCRL-ID-120758

Configuring the National Ignition Facility for Direct-Drive Experiments

David Eimerl, Editor

July 1995

Laboratory for Laser Energetics
University of Rochester
250 East River Road
Rochester, NY 14623-1299

Inertial Confinement Fusion Program
Lawrence Livermore National Laboratory
Livermore, CA 94550

LAWRENCE LIVERMORE NATIONAL LABORATORY
University of California • Livermore, California • 94550

Contents

1.0 Overview: Direct-Drive Experiments on the NIF

The National Ignition Facility (NIF) is a project whose primary mission is to provide an above-ground experimental capability for maintaining nuclear competence and weapons effects simulation, and to pursue the achievement of fusion ignition utilizing solid state lasers as the energy driver. In this facility a large number of laser beams are focused onto a small target located at the center of a spherical target chamber. The laser energy is delivered in a few billionths of a second, raising the temperature and density of the nuclear materials in the target to levels where significant thermonuclear energy is released. The thermonuclear reaction proceeds very rapidly, so that the target materials remain confined by their own inertia during the thermonuclear reaction. This type of approach is called inertial confinement fusion (ICF). The proposed project is described in a conceptual design report (CDR) that was released in May 1994.

There have been two main approaches for achieving significant thermonuclear yield in ICF: The first is to enclose a small spherical shell (capsule) containing the fuel inside a cylindrical cavity (indirect drive). The laser beams heat the cavity and the associated x-ray flux on the capsule causes it to implode and ignite. In the second approach (direct drive), the laser beams illuminate the capsule directly, heating the corona itself to a high temperature. Based on a long history of experience from existing glass lasers, primarily Nova, and from the Halite/Centurion series of underground tests devoted to ICF physics, the primary ignition campaign on the NIF will use the indirect-drive approach. However, the direct-drive approach represents a less well studied but realistic alternative. The Omega laser at the University of Rochester's Laboratory for Laser Energetics (LLE) is nearing completion, and it will add significantly to the scientific database for direct drive. Present information indicates that direct drive can reach ignition at the energy and power of the NIF. If experiments at LLE and elsewhere confirm this, there would be a strong interest in carrying out NIF ignition experiments using direct drive also.

Early in FY95, a collaboration between the University of Rochester and the Lawrence Livermore National Laboratory (LLNL) was established to study reconfiguring the NIF to accommodate direct-drive experiments. The present paper is a report to the scientific community, primarily the scientists and engineers working on the design of the NIF. It represents results from work in progress, specifically work completed by the end of the second quarter FY95.

This report has two main sections. The first describes the target requirements on the laser drive, and the second part describes how the NIF laser can be configured to accommodate both indirect and direct drive. We include a description of the scientific basis for our conclusions. At this relatively early stage in the study, we do not yet have the complete picture. Nonetheless, our present understanding is sufficient to conclude that the primary target requirements and laser functional requirements for indirect and direct drive are quite compatible. It is evidently straightforward to reconfigure the NIF

to accommodate direct and indirect drive.

Reconfiguring the NIF for direct drive[1] involves adding 24 beam ports to the target chamber to make a total of 72 ports (Figure 1-1). Different subsets of these ports would be used for direct- and indirect-drive illumination. We would maximize the laser bandwidth by adding FM bandwidth to each of the four wavelengths present in a cluster. The bandwidth during the foot would be increased to improve the early time smoothing. The laser cavity and transport optics would remain the same. The added beam divergence associated with the beam smoothing does not appear to cause a significant reduction in the peak power on target. The Front End would be modified to incorporate the beam smoothing hardware.

An additional advantage of adding ports to the target chamber is that other hohlraum designs can be contemplated, in particular tetrahedral and octahedral hohlraums.

In Section 2, we describe the target requirements, including both target design and the essential features of an experimental campaign that would reach ignition with direct drive. In Section 3, we describe the strategy for accommodating direct and indirect drive; we also present the scientific basis for the laser performance expected in the direct-drive configuration. Finally we list the primary requirements and the laser functional requirements for the NIF when configured as an indirect-drive/direct-drive facility.

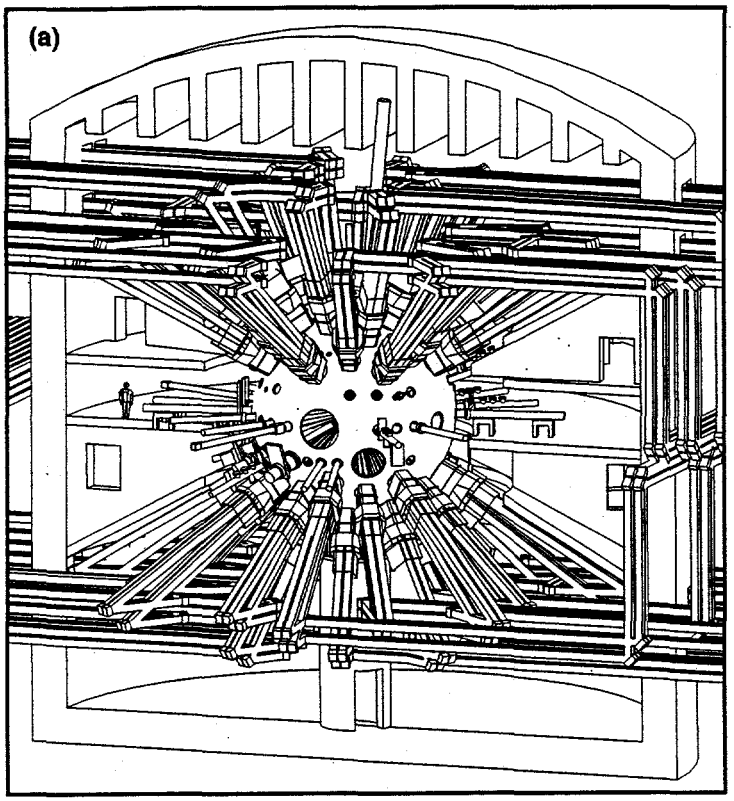

NIF indirect-drive laser target

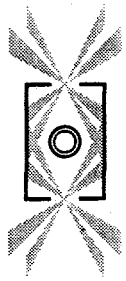

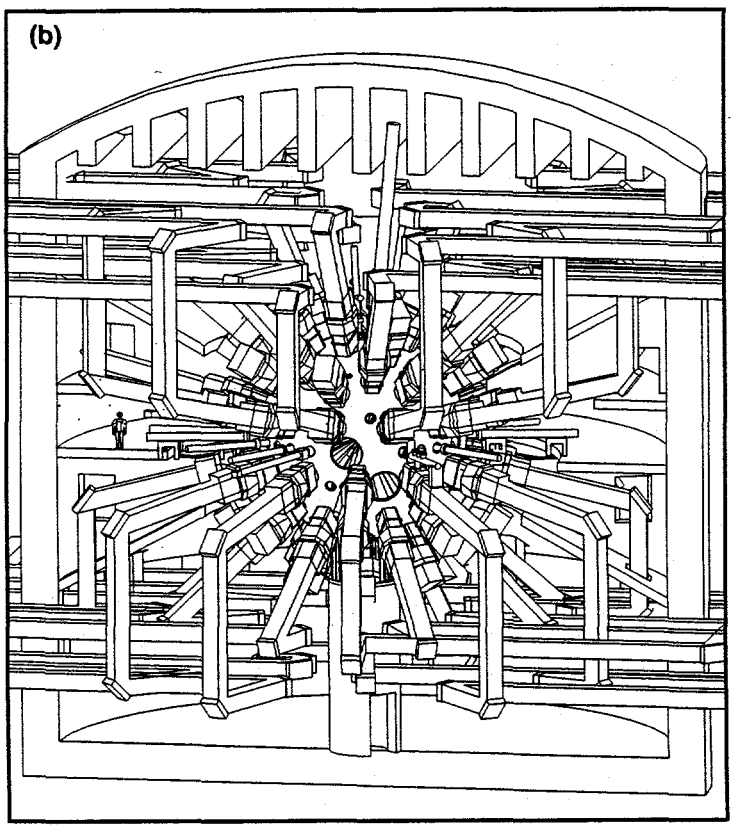

NIF direct-drive laser target

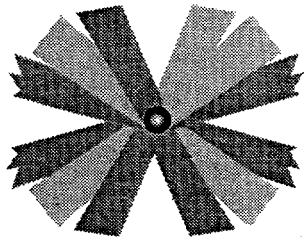

40-00-0894-3299pb03

Figure 1-1. NIF target illumination designs meet both the direct-drive and the indirect-drive requirements

2.0 Target Physics

2.1 Historical Review

In direct drive the fusion capsule is illuminated directly by the laser. The laser light is absorbed by inverse bremsstrahlung in plasma with an electron number density below the critical density, $n_c = 1.1 \times 10^{21} \lambda_{\mu m}^{-2}$ cm^{-3}. Laser light cannot penetrate into plasma of higher density. The plasma is heated by the laser to a high temperature, and thermal energy is transported by electron conduction to an ablation front at near solid density. The remaining portion of the shell is accelerated inwards in reaction to the ablation of mass. In indirect drive, the laser heats the inner wall of a hohlraum and generates soft x rays, which shine onto the capsule. X-ray transport rather than electron conduction deposits energy at the ablation front.

Direct-drive ignition capsule designs are based on direct-drive experiments conducted on the 1.5-kJ, 351-nm wavelength, 24-beam Omega laser (at LLE), and the two-beam Nova laser (at LLNL). Other direct-drive experiments have been carried out at the Naval Research Laboratory, Osaka University, the Rutherford Laboratory, and other laser facilities around the world. The results from the numerical simulation of the ignition design presented in this section incorporate the information obtained from these experiments. To date, however, predictions of capsule performance rely predominantly on the details of the physics included in the numerical simulations.

Experiments aimed at validating direct-drive physics issues relevant to NIF scale ignition capsules will be conducted on the 60-beam, 30-kJ Omega laser system at LLE, in the next few years (95–99). The LLE plan calls for examining many key physics issues relevant to NIF-scale experiments on direct-drive ICF in the years 95–98. Integrated direct-drive implosion experiments on cryogenic capsules that are hydrodynamically equivalent to direct-drive NIF capsule designs will be conducted on the 60-beam Omega system in the 98–99 time frame. Similar experiments are being performed at lower energy on the Gekko XII laser at Osaka; other direct-drive physics issues are being examined at several laser facilities worldwide.

Considerably more effort has been expended on examining indirect-drive NIF capsule designs, including work at LLNL, LANL, AWE, and Limeil. Furthermore, physics issues have been addressed experimentally in the Nova technical contract. Halite-Centurion underground experiments have also contributed to the confidence in indirect-drive capsule physics. Consequently, the indirect-drive approach is technically more mature at this time and is judged to be of lower risk. However, we note that in terms of energy on the capsule, only Halite/Centurion has exceeded that obtained by laser-direct-drive experiments. Positive experimental results in the next several years together with continuing simulation effort would considerably increase confidence in success by the beginning of NIF experiments. However, target designs and understanding of laser system requirements are also likely to evolve as a result of such work.

2.2 Direct-Drive Ignition Capsules

2.2.1 Capsule Dynamics

The energy balance in the ablation front may be evaluated by recognizing that the plasma flows through the critical density at approximately the sound speed. This simple assumption gives $I \sim \rho_c c_s^3$, where I is the laser intensity, ρ_c is the mass density corresponding to critical electron density, and c_s is the sound speed. This formula can be used to estimate the corona temperature (from c_s) given the laser intensity or the desired ablation pressure ($P_a \sim \rho_c c_s^2$). At the laser intensities relevant to ICF (about 10^{15} W/cm^2), this means that the coronal temperature is a few keV. For comparison, in indirect drive, the ablated material comes off at the radiation temperature, which is generally below 300 eV. This means that to achieve a desired implosion velocity with direct drive, less mass is ablated, which comes off at a higher exhaust velocity. As a result of this, the rocket efficiency, $\eta_r = (v_{exh}/v_{impl})^2/[\exp(v_{exh}/v_{impl}) - 1]$ is lower for direct drive. That is, less of the energy absorbed by the capsule ends up in kinetic energy of the imploding shell.

The leading edge of the conduction heat front is quite steep, because the electron conductivity varies as the 5/2 power of the temperature. Its steepness is limited when the scale length becomes comparable to the mean free path of the electrons that carry the heat flow, or equivalently, when the heat flux becomes comparable to the electron energy density multiplied by the thermal velocity. This phenomenon is called flux limiting. Processes which heat the plasma ahead of the electron conduction front contribute to raising the scale length at the front. The main contributors to this "preheat" are shocks driven by the ablation pressure, x rays emitted by the hotter regions in the plasma, and suprathermal electrons generated by the damping of electron plasma waves.

In addition to inverse bremsstrahlung, there are several ways in which laser light might be absorbed or scattered by coupling to plasma waves. These processes include resonance absorption, two-plasmon decay, stimulated Raman scattering, and stimulated Brillouin scattering. All of these processes are undesirable to various extents because they redirect the laser energy. This can result in undesired preheat, reduced absorption, and degraded symmetry. Parametric decay processes are minimized by employing shorter wavelength laser light and by keeping the laser intensity below instability thresholds. Here we assume that the wavelength is 351 nm, as in the baseline NIF design.

To achieve thermonuclear ignition and burn, a direct-drive capsule must be driven with controlled levels of preheating, and with a low in-flight aspect ratio (overdense shell thickness divided into the average radial location of that material) to minimize the effects of the Rayleigh-Taylor (RT) instability on the final core configuration. Current direct-drive NIF capsule designs require thick cryogenic fuel layers (typically a few hundred microns) surrounded by an ablator material of low atomic number (such as CH). These designs use laser pulses that are carefully shaped to control the isentrope of

the main fuel layer and ablator during the implosion. By an appropriate choice of isentrope some reduction in the RT growth rate during the acceleration phase can be achieved. These pulse shapes are also designed to minimize the occurrence of an RT unstable interface within the fuel near the fuel-ablator interface, associated with opacity and equation-of-state differences between fuel and ablator materials.

For directly driven capsules, numerical and analytic studies have shown that the RT time-dependent growth rate can be approximated by

$$\gamma(k,t) = \sqrt{\frac{A(t)kg(t)}{1+\varepsilon kL(t)}} - \beta k v_a \qquad (1)$$

where A(t) is the Atwood number, k is the unstable wave number, g(t) is the acceleration, L(t) is the density scale length, and $v_a(t)$ is the ablation velocity. The definition of v_a used in the above expression is

$$v_a(t) = \frac{\dot{m}}{\rho_p(t)} \qquad (2)$$

where $\dot{m}$ is the mass ablation rate and ρ_p is the peak density in the imploding capsule. (The parameters ε and β are approximately in the range of 0.25–1.0 and 3.0–4.0, respectively.) Simple scaling arguments and detailed numerical simulations have found that for directly driven implosions the ablation velocity scales as $v_a \sim \alpha^{3/5}$ and the in-flight aspect ratio as $R/\Delta R \sim \alpha^{-3/5}$, where the adiabat α is the ratio of the cold fuel pressure to the Fermi-degenerate pressure; it thus measures the departure from Fermi degeneracy.

The capsule energy needed to achieve ignition is lowest when the main fuel is Fermi degenerate, so that the main fuel density is highest for a given pressure. Simulations indicate that the minimum capsule energy is approximately $E_{capsule}(MJ) \approx 0.5(0.05/\eta_h)\alpha^{3/2}(v_{impl}/3)^{-5}$, where η_h is the capsule hydrodynamic efficiency, and v_{impl} is the implosion velocity in units of 10^7 cm/s. Simulations indicate that direct-drive designs with $\alpha = 1$ are likely to be too unstable to ignite for achievable levels of capsule surface finish and laser beam smoothness. Capsules may be designed to give higher adiabats; this can increase both L and v_a, improving stability. However, it raises the energy necessary to achieve ignition. The capsule point design uses shock preheat of the fuel to obtain a mass-averaged fuel α of three.

The use of higher fuel adiabat to improve hydrodynamic stability and the lower rocket efficiency for direct drive raise the capsule energy which is needed to achieve ignition. Also, only a fraction of the laser energy is absorbed by the capsule, about half for the point design, because as the capsule implodes, it underfills the laser spots. These factors tend to compensate for the x-ray conversion efficiency and hohlraum coupling efficiency losses in indirect drive, so that the energy needed for ignition is similar in the two cases.

LLE has conducted a number of one-dimensional, direct-drive, point-design calculations covering the incident energy range proposed for the NIF. Figure 2-1 displays the results of these simulations for four values of α. (The value of α assigned is determined as the mass-weighted value of the cold main fuel layer at a time close to ignition.) In Fig. 2-1, the foci of the individual laser beams are assumed to be fixed, initially tangential to the capsule (i.e., the envelope of each beam covers an entire hemisphere of the capsule).

For a direct-drive capsule in the incident energy range of the NIF, the tolerable level of initial perturbations can be estimated using the RT dispersion relation given above along with a stability model based on Haan's work.[2,3] In this model a constant acceleration from the initial radius R to a radius of $R/4$ is assumed, and the spectrum of the initial perturbation is taken from capsule data,

$$\zeta(L) = \zeta_0 L^{-1} \qquad (3)$$

where $\zeta(L)$ is the perturbation amplitude for the Legendre mode L. The model calcu-

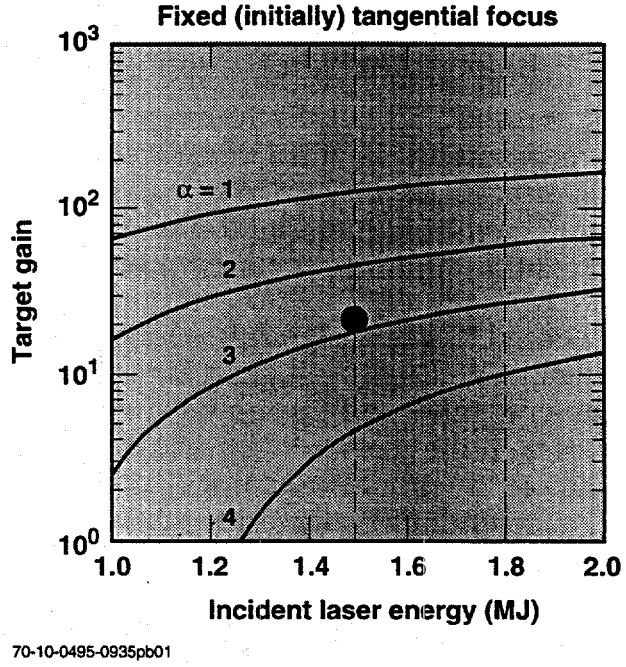

Figure 2-1. Target gain vs 351-nm laser energy depends on the adiabat α, which is the ratio of fuel pressure to Fermi degenerate pressure at the same density. Target instabilities are better controlled with higher α. The NIF target design uses 1.5 MJ and α = 3, and has a gain of about 20. The peak laser power (not shown) is increased if the beams can be more tightly focused at later times. This allows operation at a higher adiabat for increased stability.

lates the width of the RT mix region (Δr_{mix}) as a function of time. It is required that Δr_{mix} be less than the thickness of the accelerated shell Δr_{shell}.

Results of the model are shown in Fig. 2-2. Two relevant thicknesses are represented as in-flight aspect ratios relative to a shell radius of R/4. One set of curves corresponds to various initial perturbation amplitudes ζ_0, from 0.01 μm to 0.5 μm rms; the other corresponds to two implosion velocities close to 3×10^7 cm/s. The first set of curves is shown dashed for velocities below 3×10^7 cm/s.

For a capsule design with 1.5-MJ incident energy and an implosion velocity between 2.5 and 3×10^7 cm/s and an $\alpha = 1$, the maximum perturbation amplitude must be less than 0.01 μm rms for the mix thickness not to exceed the overdense shell thickness during the implosion. This amplitude represents the combination of the development of perturbations associated with capsule surface finish and initial laser imprinting added in quadrature. As α is increased, the amount of perturbation that the capsule can

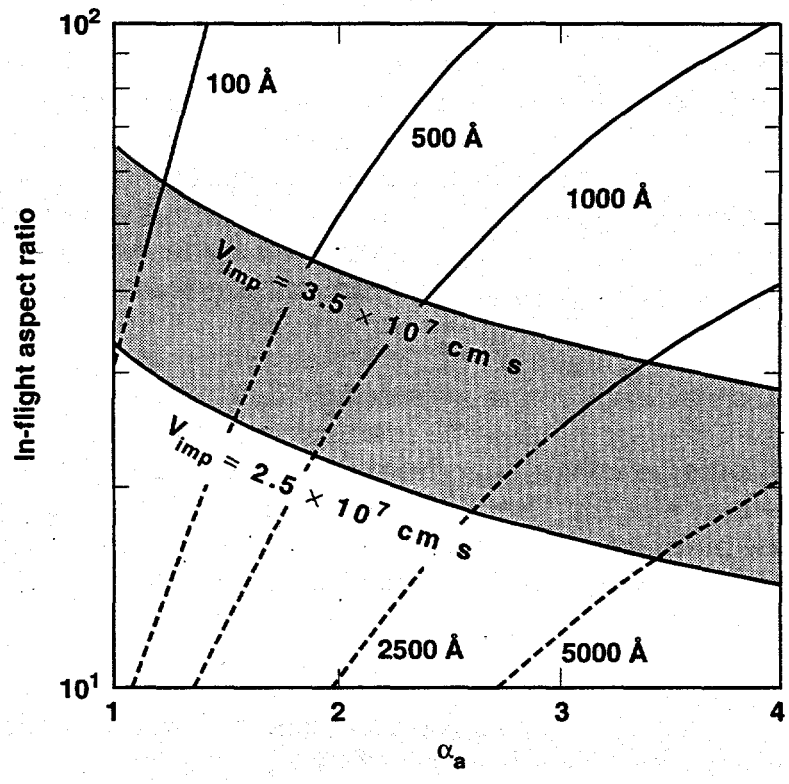

Figure 2-2. The IFAR (in-flight aspect ratio) decreases with increasing adiabat at a given implosion velocity. Lower IFAR allows the capsule to tolerate larger surface perturbations (rms in Å marked). Capsules with implosion velocities less than 3×10^7 cm/s are unlikely to ignite. Hence the surface finish contours are shown as dashed below that velocity.

withstand increases. From Fig. 2-1, an α no greater than 3–4 is required to achieve ignition and a moderate gain. From Fig. 2-2, the maximum perturbation amplitude must then be less than 0.5 μm rms.

Detailed 1-D and 2-D stability modeling has shown that the results from this simple model are reasonably accurate for the acceleration phase of the implosion. However, it should be noted that the values in Fig. 2-2 correspond to the time at which the laser power is near maximum and the acceleration is largest. When the earlier portions of the capsule implosion are included, the actual initial perturbations that the capsule can withstand are reduced by a factor of about two to three from those in Fig. 2-2. This is caused by a small amount of growth at early times due to both the RT and the Richtmyer-Meshkov instabilities. When the RT growth of initial inside-surface perturbations during the deceleration phase is also included in the analysis, the acceptable initial perturbation must be reduced by another factor of approximately two resulting in a combined initial (time before uniform acceleration of the ablation surface) outside perturbation limited to <0.1 μm rms.

Simple models such as the one above and detailed numerical simulations show that a conservative approach toward a direct-drive ignition design would be to initially start with a design for which α is between 3 and 4. This requires controlling the isentrope of the direct-drive capsule implosion. There are a number of methods that can be used to control the isentrope of the implosion of a direct-drive capsule. Two that have undergone extensive theoretical analysis at LLE are the use of pulse shaping and the addition of a material of high-to-moderate atomic number either to the ablator or to the fuel. (In the latter case, the fuel would be contained within a silicate foam, or the ablator doped with high-atomic-number material.)

The baseline direct-drive ignition capsule design is shown in Fig. 2-3. This capsule is predicted to produce a yield of 30 MJ when irradiated by the "picket fence" pulse in Fig. 2-4. This pulse shape contains approximately 1.5 MJ of 351-nm laser light shaped to produce a peak power of 475 TW. There are a number of possible shapes to the main (drive) portion of the pulse that can be considered and still preserve capsule performance. The baseline ignition capsule is described below, followed by a discussion of one (of the many) alternative designs.

The direct-drive ignition capsule incorporates a cryogenic solid deuterium-tritium (DT) layer surrounded by a very thin CH polymer ablator. The cryogenic DT layer is maintained by an effect called "beta-layering." The beta-layering process creates a DT layer of uniform thickness by a process in which regions where the layer is thicker are preferentially heated from energy deposited by beta particles (electrons) from the radioactive decay of the tritium. The DT sublimes from the thicker regions and redeposits in regions where the DT layer was originally thinner. This process eventually results in a DT layer of uniform thickness. The central region of the capsule is filled with a gas whose density and isotopic concentration are determined from the temperature at which the fuel layer is maintained. At the triple point of 18 K, the density of the gas is approximately 0.7 mg/cm^3. At 18.2 K, considered for this discussion the nominal condition, the gas density is approximately 0.3 mg/cm^3.

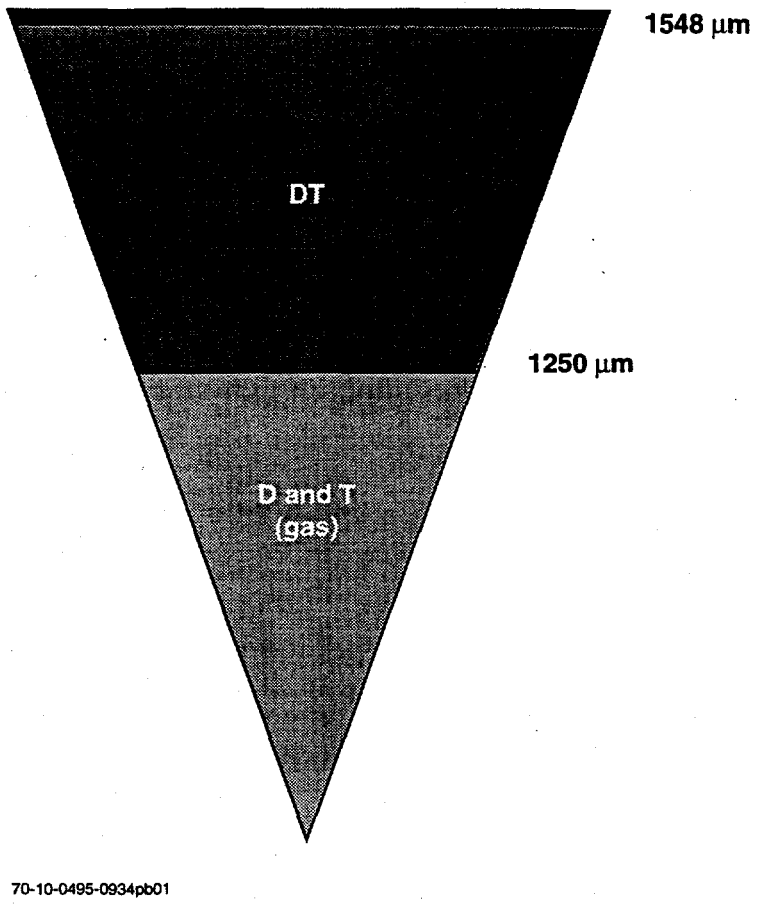

Figure 2-3. The LLE direct-drive target is 300-μm thick pure DT with outer radius 1548 μm, filled with low-density DT at about 0.5 mg/cm^3 (not drawn to scale).

At the nominal central gas density the location of the material composing the inner edge of the initially cryogenic main fuel layer converges by a factor of approximately 20 before ignition. For the purpose of this discussion this reduction in radius will be referred to as the hot-spot convergence ratio. The convergence ratio of a given capsule implosion is a key factor in determining the symmetry required to drive the implosion. Higher convergence ratio results in a tighter requirement on the uniformity. For the baseline design, the irradiation nonuniformity associated with long-wavelength Legendre modes (L = 1-20) must be below 1% rms throughout the duration of the laser pulse. Short time duration increases in the irradiation nonuniformity can be tolerated. The detailed levels and time duration depend on the spherical-harmonic mode number of the asymmetry produced by the swings. The baseline design assumes 192 beams arranged in 48 groups of 4 beams of slightly differently frequency. The 48 clusters are distributed nearly symmetrically about the capsule.

The sensitivity to long wavelength drive asymmetries can be reduced by decreasing the hot spot convergence ratio. One method of reducing this value is to initially increase the density (pressure) of the central gas region by increasing the temperature of the

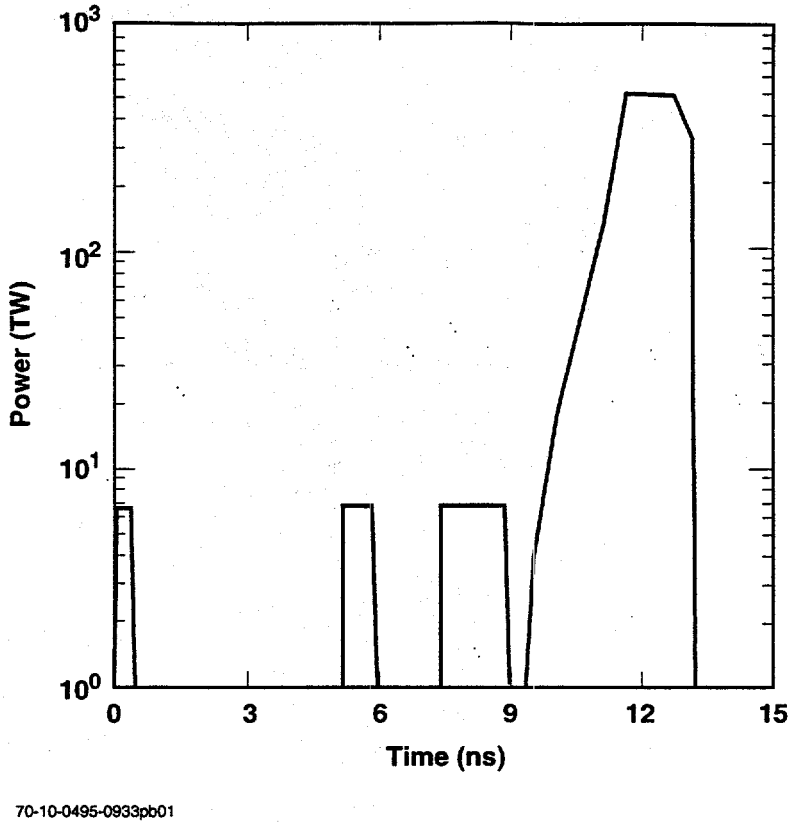

Figure 2-4. The picket fence laser pulse shape for the target in Fig. 2-3.

main cryogenic fuel layer. This process results in a reduction in the hot-spot convergence ratio; however, due to the fact that the final product of the compressed fuel density and radius is reduced, the yield will also decrease. Figure 2-5 displays the results of a number of 1-D simulations in which the initial central gas density was varied between 0.1 and 1.0 mg/cm^3.

The performance of the direct-drive ignition designs is limited by both laser-plasma and hydrodynamic instabilities. Theoretical studies and, at present, limited experimental data indicate that for most of the laser-plasma instabilities important to direct-drive implosions, it is the single-beam intensity that determines the laser-plasma instabilities and not the overlapped intensity. For all of the designs discussed in this section the single beam laser intensity was maintained below mid 10^{13} W/cm^2. Theoretical studies indicate that for the plasma-density scale lengths associated with the direct-drive ignition designs these intensities are sufficiently below the levels at which laser-plasma instabilities might adversely affect capsule performance.

The evolution of hydrodynamic instabilities and their effect on capsule performance have been examined using detailed 1-D and 2-D numerical simulations. For direct-drive capsule implosions, the development of perturbations arising from capsule fabrication and those seeded by laser irradiation nonuniformities must be considered. The detailed

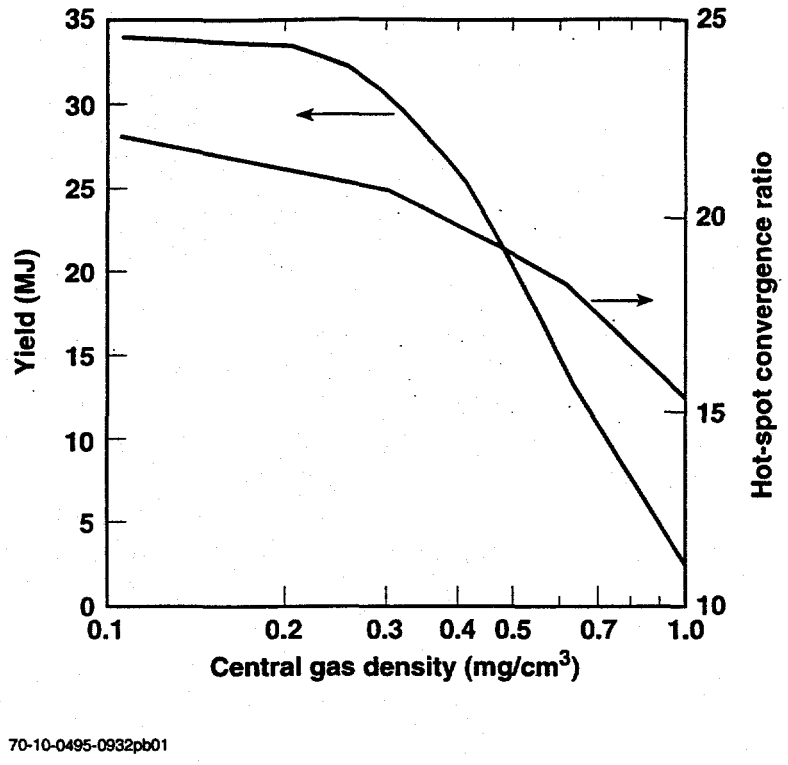

Figure 2-5. Yield and convergence ratio as a function of central gas density.

numerical simulations coupled with a saturation model have shown that for the baseline capsule design, the combined laser imprinting and capsule finish of the outside CH ablator surface must be below 0.1 μm rms. Since these two quantities add in quadrature, the requirements associated with the capsule finishing and irradiation uniformity must be balanced against one another. The analysis of the growth of perturbations due to feedthrough of the development of outside surface perturbations and initial inside cryogenic layer surface perturbations show that the inside surface finish associated with the cryogenic layer must be below 0.5 μm rms.

2.2.2 Direct-Drive Pulse Shapes

Pulse shapes for direct-drive capsules may be divided into two principal sections. The high power portion at later times accelerates the compressed shell inward. For the pulse shape shown in Fig. 2-4, the high power portion gives an ablation pressure of ~100 Mbar for ~2 ns. The length and height of the high power portion are set by the capsule radius and by intensity limits defined by RT and plasma stability (see Section 2.3). All of the earlier part of the pulse, the "foot," is designed to bring the DT shell up to the 100 Mbar acceleration pressure while controlling the adiabat. This is accomplished by sending several shocks through the fuel. It is necessary to use at least a few shocks of increasing strength or too much entropy will be produced in the fuel. However, some entropy must be added to set the fuel on the adiabat desired for hydrody-

namic stability, $\alpha = 3$ for this particular pulse. It is possible to generate most of the entropy with the first shock, and time the subsequent shocks to generate additional entropy. It is also possible to generate a large fraction of the entropy with the later shocks by adjusting their timing and strength. This pulse shape uses the second strategy.

The pulse shape also affects the imprint of laser intensity fluctuations. The intensity during the imprint phase affects the size of the pressure nonuniformities and the thickness of the plasma layer in which conduction smoothing occurs (see Section 2.2.3). Simulations indicate that the pulse in Fig. 2-4 gives less damaging imprint than a pulse with a first picket several times higher, for which the first shock would give most of the fuel entropy. The relation between pulse shaping and imprint is complex and has not yet been tested by experiments. Also, there are many degrees of freedom in the pulse shape. For example, the first picket in this pulse generates a pressure impulse. The strength of the impulse is related to the product of the length and the height of the picket. A longer and lower or shorter and higher picket would give the same impulse but would imprint differently.

There is a wide range of alternate direct-drive capsule designs that can be considered for the NIF. As shown, the baseline design incorporates a picket-fence pulses, which use different numbers of pickets, power, and temporal duration.

Some direct-drive designs have also been carried out that incorporate continuous pulse shapes. Continuous pulse shapes offer some reduction in the sensitivity of timing between individual beams that can result in long wavelength irradiation nonuniformities being generated during the pulse. For the purposes of this discussion, we will concentrate on one of these point designs. The capsule is very similar to the baseline design shown in Fig. 2-3. The continuous pulse shape is shown in Fig. 2-6.

The issues associated with the laser-plasma and hydrodynamic instabilities are very similar to those discussed with the baseline design. The pulse shape shown in Fig. 2-6 places the capsule on an $\alpha = 3$. The resulting irradiation uniformity and capsule surface finish requirements are comparable to the baseline case discussed previously, and again, the individual beam intensity is maintained below 10^{14} W/cm^2.

Pulse shaping tradeoffs will be examined in simulations and experiments during the next few years. It is desirable to retain as much flexibility in the pulse shaping capability as possible. However, this flexibility does not expand the limits of total energy and peak power which are discussed in Section 2.3. Also, the contrast ratio of the pulses illustrated is large enough to encompass designs with adiabats in the desired range.

2.2.3 Imprint

The short wavelength nonuniformity (s_s) arises from speckle structure on the individual beamlets and surface roughness. Smoothing by spectral dispersion (SSD) is a technique envisaged for reducing the laser imprinted component of this structure and can be combined with a birefringent wedge for polarization dispersion (see Section 3.4). Additional very short wavelength structure ($L > 500$) is produced by beam-to-beam

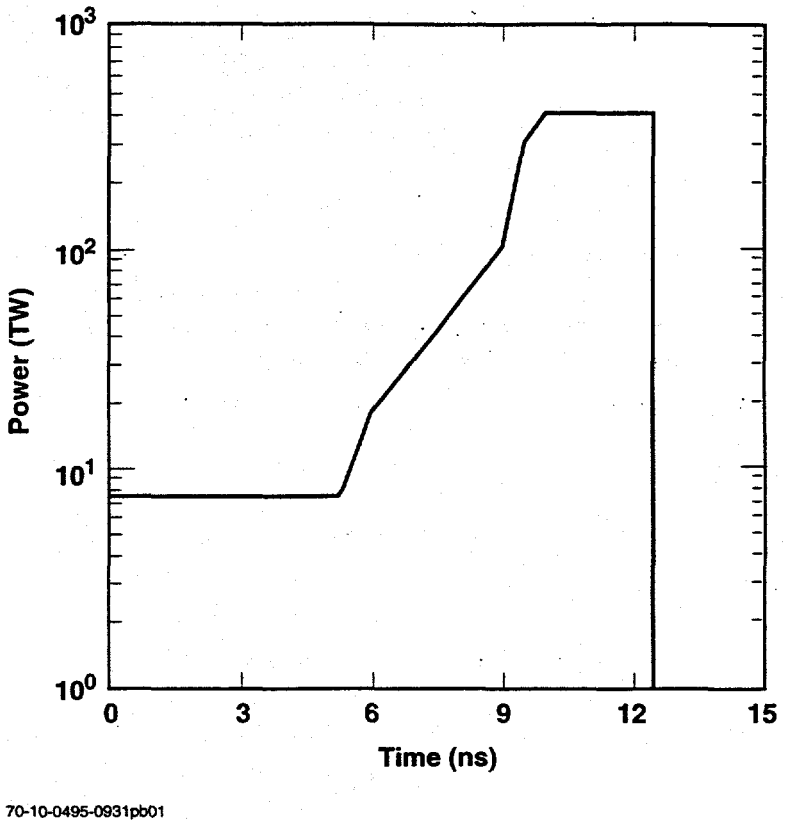

Figure 2-6. Continuous laser pulse shape for advanced target designs.

interference. Both SSD and the use of different frequencies for beamlets within a cluster will reduce this structure. Since these wavelengths involved are too small to affect capsule performance, this contribution to nonuniformity will not be further discussed here.

The spectrum of surface perturbations is the most important seed of RT instability in indirect drive, and it has been investigated in some detail. The typical spectrum of surface roughness exhibits a plateau at low L numbers with a fall off as L^{-1} for $L > 30$. The RMS amplitude of the surface perturbations obtained with the best fabrication method for polymer shells can be kept below 70 nm. For direct drive we must consider also the additional effective surface perturbation from laser speckle. This is a rather complex matter which has had relatively little experimental investigation; current understanding is based mainly on numerical modeling. The general character of SSD smoothing (see Section 3.4) is that there is a superposition of laser speckle patterns from many beams giving an instantaneously fairly flat spectrum of intensity perturbations in the L-mode range of interest with rather large (tens of percent) spectrally integrated RMS amplitude. Rapid temporal fluctuation of this pattern gives a time averaged smoothing which reaches time-integrated RMS intensity variations below 1% on a time scale of less than 1 ns. This temporal smoothing with SSD is ineffective for low L-modes which do not fluctuate in time, but because of the small spectral range the spectrally integrated RMS levels for low L-modes from this source are also less than 1%.

Modeling with 2-D hydro codes show that the hydrodynamic perturbations arising from laser intensity fluctuations develop quickly and after only 1 or 2 ns grow at a rate that is the same as those of perturbations from surface roughness. The imprinted effect can therefore be characterized by an equivalent surface roughness as illustrated in Fig. 2-7. The imprinting process therefore apparently terminates at the time when the growth rate of the imprint is indistinguishable from the growth rate from surface roughness. This apparent termination can be understood as the dominance of processes multiplying the current amplitude over the source of new amplitude from intensity fluctuations. The processes in question involve the oscillatory behavior of a rippled shock wave, Richtmyer-Meshkov instability and Rayleigh Taylor instability. The latter is dominant in the main acceleration phase, but the termination of imprint typically occurs earlier, before the first shock break out at the inner surface of the target shell, due to a combination of all three processes.

A further factor affecting the imprint process is diffusive electron heat conduction which smoothes the energy flow between the radial zone of absorption and the pressure maximum at the ablation front. The separation of absorption zone and ablation front develops rapidly in a few nanoseconds to a scale relative to the higher L-modes such that it provides an effective diffusive smoothing which advances the time at which imprint terminates, and thus reduces the equivalent surface perturbation due to imprint.

Higher spatial frequencies imprint only at early times in the laser pulse, while the lowest spatial frequencies continue to imprint longer. This feature may permit laser strategies which smooth better at early times when the capsule is more sensitive, and which smooth less effectively at later times. For example, the laser bandwidth could be

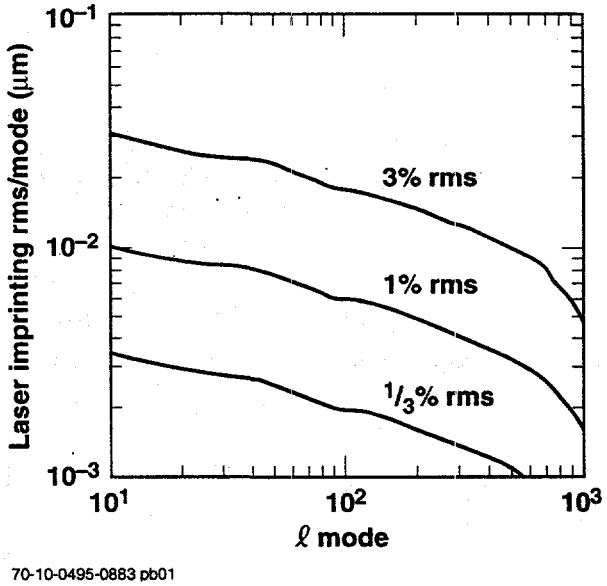

Figure 2-7. Equivalent surface finish expressed as RMS mode amplitude in μm, as a function of mode number, parametrically with the laser beam smoothness at 1 ns.

larger during the foot of the pulse, and smaller during peak power, when bandwidth would otherwise reduce the peak power by lowering frequency conversion. A conservative allowance for this effect is that the nonuniformity could be a factor of two larger, namely 2% rms in the modes L = 21–500, during the high power (P > 100 TW, say) portion of the pulse. Design calculations will be needed to assess the sensitivity of the capsule to smoothing of different spatial frequencies at different times during the pulse. Until such work is done, it is prudent to retain the requirement of 1% rms smoothness in modes L = 20–500, averaged over 1 ns.

Schemes have also been proposed, and to a lesser degree examined experimentally, to mitigate imprint by pre-forming a smoothing plasma around the capsule, or to utilize plasma fluctuations in the corona to smooth the laser intensity fluctuations. These schemes have not been verified experimentally, nor thoroughly examined in simulations, for NIF direct-drive capsule conditions. Therefore, such methods may not be relied upon at this time to lessen beam smoothing requirements. However, they provide an option to improve performance or to compensate for unfavorable developments in other areas of direct-drive capsule physics (for example, if RT growth rates were found to be higher than is indicated by current experiments and simulations).

Experimental measurements of imprint and comparisons with modeling are now beginning to be made and give some confidence in the models (to an accuracy of a factor of a few at present) but more work is needed to better understand the L-mode dependence of the process and to give a closer measure of amplitudes for NIF relevant irradiation conditions.

Where the growth of imprinted single modes has been modeled for NIF targets and folded in with the growth of surface perturbations it has been concluded that ignition can be achieved using 2-D SSD. These calculations have assumed that each cluster contains four beams of bandwidth about 0.5 THz, and separated by about 0.5 THz in frequency, polarization plates and multiple beam overlap, to give <1 % rms. fluctuations averaged over 1 ns (see Section 3.4). A surface roughness of <70 nm rms was assumed. The equivalent surface perturbation of the imprint is then also <70 nm rms.

2.3 Capsule Performance Margin

It is possible to estimate a target performance margin for direct-drive ignition capsules by similar methods as for indirect-drive capsules.[4] The analysis scales capsules from the design in Fig. 2-3 and with the pulse shape shown in Fig. 2-4, except with the peak power set at 412 TW. The focusing is assumed to be flat intensity over a spot size with diameter 0.9 times the initial target diameter. This point design has a laser energy of 1.3 MJ and peak power of 412 TW. Designs are scaled in laser power and energy by varying the capsule radius, aspect ratio, pulse length, and peak intensity. In-flight capsule aspect ratio and fuel adiabat are held constant based upon the assumption that these figures of merit have the values which are needed to achieve adequate hydrodynamic stability. The capsule quality factor on the low power side is the ratio of the shell kinetic energy to the minimum energy necessary to give ignition. The quality factor on

the high power side is a plasma physics limit, which is taken to be 10^{14} W/cm^2 divided by the single beamlet intensity. The quality factor is unity for a target which is just marginal either for ignition or plasma physics, and the margin, s = q – 1, is correspondingly zero for a marginal capsule. The plasma physics margin for the point design is 1.8, which allows for considerable uncertainty in the plasma physics requirements, or improvement in capsule performance if higher peak power can be obtained. The ignition marginis 0.9, which is close to the figure for the indirect-drive design at 1.8 MJ, 500 TW. A contour plot of margin vs. laser energy and peak power is show in Fig. 2-8. For comparison with the CDR data, we have shown the case for $\mu = 2/3$, where ablation pressure varies with laser intensity as $P_a \sim I^{\mu}$. Conclusions do not change substantially for other reasonable values of μ.

Designs at different points within the space of laser energy and peak power have a differing balance in the trade-off between ignition margin and laser plasma physics properties. The figure also illustrates that the laser design provides a reasonable margin in deliverable power and energy over the minimum for which ignition can be achieved. Of course, the risk is higher for capsule designs with lower margin. Also, capsule designs have many more parameters than laser energy and peak power. If hydrodynamic stability is better than this analysis supposes, then the capsule could be imploded on a lower adiabat, resulting in greater ignition margin and higher gain for a given energy and power. If stability is worse, the adiabat could be raised somewhat before the ignition margin would be lost. Different pulse shapes or other preheating strategies can be used to get to the same fuel adiabat. Such design variations will affect laser imprint

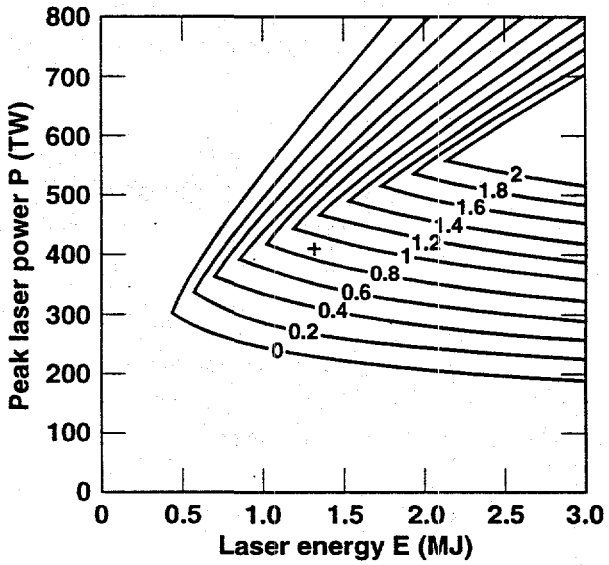

Figure 2-8. The performance margin of direct-drive targets scaled from the 1.5-MJ LLE target design. The lower bound on laser power derives from the implosion velocity requirement, and the upper bound derives from laser-plasma instabilities. All targets in this plot are stable.

and other capsule parameters. The flexibility to explore different design options is an essential feature of the NIF. Also, understanding of direct-drive capsule physics will be much more complete after the experiments on the Omega laser system during FY95-FY98 have been completed, as well as other experiments considerably at lower energy on other laser facilities, including the NIKE laser at Naval Research Laboratory, the Gekko XII laser at Osaka, and the Nova laser at LLNL.

2.4 Direct-Drive Uniformity Criteria

Direct drive requires that the laser intensity incident upon the capsule be nearly uniform at all times. This illumination requirement is simpler than that for indirect drive, since the pattern of illumination of a hohlraum may be complex and may change in time. Also, the relationship between the laser intensity pattern and the x-ray illumination uniformity upon the capsule can be complex. On the other hand, for direct drive, there is less smoothing between the laser illumination region and the ablation pressure than for indirect drive. Laser light deposits at a range of depths in the plasma surrounding a direct-drive capsule. The FWHM radial thickness of the deposition region varies between about 20 μm, in the middle of the first picket for the point design, to about 250 μm during the middle of the peak power portion of the pulse. Also, the laser refracts while going through the plasma. For the purposes of setting uniformity requirements on the laser, we can express the uniformity requirements in terms of the RMS uniformity on a hard sphere in two bands of L-modes.

The angular variation of the ablation pressure may be described in terms of spherical harmonic modes. The L-mode is related to the spatial wavelength by the radius of the target

$$L = \frac{2\pi R}{\lambda} \quad . \tag{4}$$

We define the long wavelength or low L-mode nonuniformity as the contribution to the total RMS from modes $1 \le L \le 20$. The high L-mode of short wavelength nonuniformity is the contribution from modes 21– 500. Modes that are shorter in wavelength are not expected to affect capsule performance, because they do not significantly "feed through" to the inner surface of the capsule, and because their Rayleigh-Taylor growth rate is severely reduced by ablation effects, thermal conduction and density gradients.

The relationship between pressure and laser intensity can be expressed most simply in terms of a "hard sphere" model of the target, where each ray bundle in the laser beam deposits all its energy at the point of impact on the sphere (see Section 3.2). The spherically symmetric component of the pressure is related to the average laser intensity by a power law, $P = Ia^{\nu}$, where ν is estimated to be 2/3 based on simulations and theoretical arguments. If this also applies in the hard sphere model, we find a one-to-one relationship between pressure L-modes and laser intensity L-modes. Then writing the intensity as

$$I(\Omega) = \Sigma I_{LM} Y_{LM}(\Omega) \tag{5}$$

we form the locally time-averaged intensity $I_{m'}$

$$I_m(t,\Omega) = \frac{1}{\tau} \int_{t-\tau/2}^{1+\tau/2} dt' \; I(t',\Omega) \tag{6}$$

and write

$$I_m(\Omega) = I_0 \left[1 + \sum_{L>1,M} \sigma_{LM} \; Y_{LM}(\Omega) \right] \tag{7}$$

Then the low L-mode nonuniformity is

$$\sigma_L = \left(\frac{1}{4\pi} \sum_{L \le 20} \sigma_{LM}^2 \right)^{1/2} \tag{8}$$

and the high L-mode nonuniformity is

$$\sigma_H = \left(\frac{1}{4\pi} \sum_{L=21}^{L=500} \sigma_{LM}^2 \right)^{1/2} . \tag{9}$$

The target requirements usually take these limits on the laser intensity to be 1% each for an integration time of 1 ns based on simulations.

The hard sphere model may not describe the relation between pressure and laser intensity when there is a well developed corona that refracts the beams and distributes the energy of a ray bundle over a sizable region of the corona. The pressure nonuniformity is driven by the energy deposition on the corona, which is transported to the solid density material by electron conduction. A diffusive process, electron conduction smoothes out the nonuniformities in the energy deposition. Then the pressure nonuniformity is

$$\frac{\delta P}{P} = \nu \frac{\delta I}{I} f(I,T,Z) \tag{10}$$

where f is a function of the plasma parameters, and is time-dependent. For some modes electron conduction can reduce the pressure by a very significant factor. For nearly uniform pressure, the pressure uniformity is simply

$$\sigma_P = f \nu \sigma_I \tag{11}$$

where σ_I is the intensity uniformity.

The target requirements as given, do not include all these effects. Nonetheless, for our study of nonuniformity, we elected to eliminate all reference to target parameters and optimize the intensity nonuniformity instead. Although fv < 1, we shall take the target requirement on nonuniformity to apply to the intensity nonuniformities. This is clearly quite a conservative approach.

The various contributions to these parameters are discussed individually in Sections 3.2, 3.3, and 3.4. Most of the lower mode spatial structure is constant in time, although there are sources of lower mode structure that could vary in time. The high mode structure generally fluctuates in time, and the temporal structure is likely to vary with mode number.

Simulations indicate that targets can tolerate intensity nonuniformity of 1% rms in modes L = 1–500. Sensitivity of the target to the mode spectrum within that range has not been addressed in detail. The patterns examined are typical of what a realistic laser system could generate; the power is strongly weighted to the lower modes as the higher modes are strongly smoothed by beam overlap and SSD. Full 3-D simulations are not available. However, LLE has simulated in 2-D implosions driven with intensity patterns taken from great circles lineouts through full 3-D Monte Carlo intensity patterns. With 8% rms power imbalance between individual beams, the specified 1% rms intensity nonuniformity is obtained. Several simulations were carried out corresponding to different great-circle lineouts. In each case ignition occurred. The implosions were of a capsule with higher convergence than the point design, and all simulations ignited. The amount of capsule margin at the 1% rms limit has not been characterized quantitatively, although it appears that this limit is neither close to the calculated failure point nor unreasonably conservative.

2.5 Experimental Campaign

The experimental campaign must deliver scientific data of sufficient quality to determine at least one set of illumination conditions for which the target ignites. However, the quality of the scientific data depends on the effort devoted to the campaign. With more NIF shots the quality of the data will improve, giving higher confidence in our understanding of the target science. The number of shots devoted to direct-drive experiments on the NIF will be a balance between the need for high-quality data on the one hand, and the lifetime shot capability of the NIF facility and the value of other campaigns on the other. While we are not in a position at the time of writing to discuss the larger question of the shot count for all the proposed NIF campaigns, we can compare the data required for the indirect- and direct-drive campaigns and determine the additional shots required for direct drive.

The NIF CDR suggests that 1600 shots be devoted to the indirect-drive campaign. This represents the judgment that 1600 shots will be sufficient to develop data of sufficient quality to reach ignition ("ignition data"). About 500 of the 1600 shots are devoted

to activating the laser system, and many of these may not need to be repeated for the direct-drive campaign. Table 2-1 gives a top-down estimate of the shot count for direct drive, using a similar method to that used for indirect-drive. The total number of shots for a stand-alone direct-drive campaign is the same as indirect drive, i.e., about 1600, of which about 500 represent laser activation.

We do not expect that there will be a complete overlap between the laser activation shots needed for direct and indirect drive. The most obvious difference is beam smoothing implementation, but there are also differences in the sensitivities to other laser parameters. Direct drive may ultimately require tighter tolerances on some laser parameters than indirect drive, such as beam pointing and beam power balance. These differences imply additional laser activation shots for direct drive, which we tentatively estimate at between 100 and 200.

Before the NIF is activated, the Omega facility at LLE will have spent several years conducting experiments that establish the target requirements for direct drive. If the Omega campaign achieves all its goals, we would need significantly fewer shots to reach ignition on the NIF. However, there are differences in energy scale and illumination geometry between Omega and the NIF; it is more likely that a significant campaign on NIF will be required to establish the appropriate scaling laws. There will certainly be a significant contribution from Omega. If we assume that Omega campaign will provide half of the needed scientific data at NIF scale, then only half the target campaign shots would be needed. In view of the large uncertainties in these assessments, we provisionally bound the additional shot at requirement between 600 and 1200, with 800 as its most probable value.

The transition time to change the illumination geometry between the indirect and direct drive configurations is essentially down-time for the entire system. (Low-energy shots with less than 48 beam clusters can be performed during such a transition, but this possibility does not change the conclusions.) With a long transition time, the transition would be undertaken less frequently than with a short transition time, to minimize the down-time. Also the scientific information learned per shot increases if the shots are allocated in groups separated by adequate time for evaluating the data and understanding its implications. Changing the configuration several times during the NIF campaigns is clearly advantageous for maximizing the value of each individual shot, and providing system flexibility. If transitions are scheduled at three per year, the transition time should be about two weeks from the last shot of the previous campaign to the first shot of the next campaign. Given the time required for alignment and other necessary activities, only a few days at most are available for the transition time for the beam ports. This rapid transition can be achieved only with large kinematic mirrors under remote control. An attractive feature of this approach is that it does not require large-scale re-engineering or construction, and it avoids the associated hazard to the optics, target chamber, and target diagnostics.

In summary, we estimate that the direct-drive campaign will require 1600 shots as a stand-alone campaign. Using data from NIF indirect drive experiments and Omega direct-drive experiments, we estimate the additional shots required for direct drive to be

between 600 and 1200. Changing from one illumination geometry to another must be accomplished rapidly, with the use of remotely controlled kinematic mounts.

Table 2-1. Shot count for direct drive.

I. Startup experiments: 500 shots
1. Disk shots, core diagnostics
2. Beam symmetry
3. Beam smoothing
4. Beam pointing
5. Pulse shaping
6. Power balance

II Hydrodynamics experiments: 400 shots
1. Gross energetics: laser deposition, ablation velocity, bang times
2. Planar RT
3. Convergent RT
4. Implosions mix experiments

III. Plasma physics: 300 shots
1. Planar SRS, SBS, filamentation
2. Parametric instabilities in spherical geometry, implosions

IV. Implosions: 400 shots
1. Pre-cryo: intermediate power
a. Square pulse, low smoothing
b. Square pulse, maximum smoothing
c. Shaped pulse - modest contrast, low smoothing
d. Shaped pulse -modest contrast, high smoothing
e. Shaped pulse - high contrast, low smoothing
f. Shaped pulse - high contrast, high smoothing

2. With cryogenic targets: intermediate power
a. Square pulse, low smoothing
b. Square pulse, maximum smoothing
c. Shaped pulse - modest contrast, low smoothing
d. Shaped pulse -modest contrast, high smoothing
e. Shaped pulse - high contrast, low smoothing
f. Shaped pulse - high contrast, high smoothing

3. Ignition implosions: full power
a. Demonstrate ignition
b. Parameter scans with ignition

Total number of shots: 1600

3. Laser Design

The target requirements for direct drive have been described in the previous section. Previously, we had developed a conceptual design for reconfiguring the NIF to include direct drive.[1] Here we present a technical analysis of these laser modifications. Our results strongly support our previous position that the NIF can meet the direct-drive requirements.

3.1 Strategy for Direct Drive

The strategy for modifying the NIF laser to accommodate direct and indirect drive should address several concerns. These include: (1) additional costs associated with adding the additional hardware should be kept to a minimum; (2) the modified system must be compatible with the indirect drive requirements; and (3) the plan must be flexible enough to respond to information obtained in the future, from Omega and elsewhere, regarding the laser parameters that will lead to ignition. A particularly important issue to resolve is whether direct drive should be included as an upgrade to the NIF, to be completed at a later date after indirect-drive experiments have begun; or whether it should be built into the facility during construction. The case for the latter course of action is compelling.

The main differences in the laser system requirements are the target illumination geometry and the need for smoothing to control both imprinting and the spherical distortion at ignition. The baseline illumination geometry is almost certainly incompatible with the port locations required for indirect drive. Given the past locations required for indirect drive, an illumination geometry suitable for direct drive may be obtained in one of three ways: (1) additional ports could be added to the indirect-drive chamber; (2) a second target chamber and experiment area could be built; and (3) the beams could be pointed from the indirect-drive locations so that some of them are not directed radially onto the capsule. Only the first possibility is reasonable; the second is expensive, and the third can be dismissed as ineffective (see Section 3.2). Moreover, adding the direct drive at a later date would require full reconstruction of the transport optics with considerable hazard to the optics, and a delay in experiments of between six and twelve months. The preferred approach is to build into the NIF at the outset the extra ports required for direct drive and at the same time add the mechanical capability to switch from one illumination geometry to another. It is therefore a high priority to determine the desired port locations before engineering design is started.

The beam smoothing strategy is less certain. Experiments have not yet been conducted to verify that propagation of suitably modulated beams through a NIF-like laser architecture is possible at the desired pulse energy and peak power. Also it is likely that data from Omega and elsewhere will indicate a preference by spherical targets for smoothing with particular characteristics. It is clearly desirable to remain flexible with respect to the beam smoothing implementation. The Front End would be designed to accommodate those schemes that are believed at the present time to be attractive. The scheme selected in the light of future scientific data would be implemented at a later

date closer to the direct-drive experimental campaign. Implementation costs would be borne by operating funds or taken out of construction funds held over for this purpose. It is likely that the cost of implementing a smoothing scheme will be compatible with either approach. Smoothing technology is currently under development. Experience on Nova and Omega will be incorporated into experiments on the Beamlet laser at LLNL to validate our approach to NIF.

Thus the laser strategy for direct drive is to design a target chamber at the outset that can accommodate both indirect- and direct-drive illumination geometries, and to design the Front End to accommodate changes that can be foreseen today in implementing the modulation required for beam smoothing.

We believe that this strategy will result in a flexible system for direct-drive experiments. In the laser modifications, we envision the temporal pulse shape will be continuously variable, and the bandwidth will be adjustable between the foot and the main pulse. The spatial profile of the beams at the target can be controlled by using different phase plates. The size of the beams can be adjusted in the same way. The average shape of the beams at the target (elliptical vs circular) can be controlled in a time-dependent manner by adjusting the parameters of the smoothing hardware. The illumination geometry can be fine-tuned by repointing beams so that they are slightly nonradial at the target. This represents a sufficiently large adjustment, despite the time dependence of the beams' apparent position, to fine-tune the time-dependent uniformity for optimum target performance. The power and energy of individual beams can be adjusted for further control of uniformity. The system we envision will have considerable flexibility within the basic constraints of frequency-converted glass lasers to optimize the drive uniformity and control target instabilities. This system easily supports the projected experimental campaign.

The NIF will also be capable of some alternative illumination strategies that will increase the implosion velocity at the expense of increasing imprinting. One such strategy is discussed below (see Section 4.0). There is also the possibility of using 527-nm light rather than 351 nm, if it is deemed worthwhile. While there is some debate about the value of enabling green operation of the NIF, it remains a possibility under consideration.

In this section we begin with the target requirements as described in the previous section, and present the scientific basis for our vision and design of a direct drive capable NIF.

3.1.1 Direct-Drive Laser Illumination Criteria

To perform direct-drive ignition experiments on the NIF, the nonuniformity from direct laser irradiation of the capsule should be less than 1–2% rms when averaged over an irradiation time of 1 ns. As discussed above, the exact tolerance of direct-drive targets to irradiation nonuniformity depends on the spatial wavelength of the nonuniformity. Typically, the RMS values for long and short wavelength structures should each be less than about 1%.

The low L-mode nonuniformity is controlled by the following: placement of beam ports in the target chamber, the power and energy balance between the beams, errors in beam positioning and capsule placement, and the beam spatial profile on the capsule. The geometric placement of the beam ports and the beam profile errors contribute to modes 1–20. Beam power imbalance and positioning errors contribute to modes L = 1–8. Capsule placement is primarily L = 1, and the tolerance for this error may be significantly larger than 1%. These individual contributions are discussed in detail in Section 3.2.

The high L-mode nonuniformity is produced by speckle structure on the individual beamlets. One technique for reducing the target sensitivity to this structure is smoothing by spectral dispersion (SSD) combined with a birefringent wedge for polarization dispersion. This technique relies partially on the overlap between independent beams on the capsule; it is advantageous to overlap as many independent beams as possible to minimize it. One example of SSD combined with polarization dispersion is discussed in Section 3.4. The remaining modes L > 500 represent very fine structure produced by fine speckle structure in the beams and by beam overlap. These modes are strongly attenuated by electron conduction, and they are not expected to be significant for capsule performance.

3.2. Low L-mode Uniformity

The deviation from sphericity of the pellet at ignition receives contributions from the laser nonuniformities at all spatial scales. For wavelengths that are long compared to the shell thickness a significant contribution is the nonuniformity of the laser drive itself. This nonuniformity receives contributions from a number of sources. In increasing order of importance, these are: the intrinsic uniformity associated with the port locations, the capsule positioning, the beam profile from the phase plate in the extended focus, the power balance between the beams, and the pointing errors of the beams. There is also a small contribution from the beam smoothing used for short wavelengths, which we believe to be negligible. In general these contributions are uncorrelated; they add in quadrature to give the overall low L-mode nonuniformity which is to be compared with the target requirements. We have

$$\sigma^2 = \sigma_{pointing}^{\ 2} + \sigma_{power}^{\ 2} + \sigma_{profile}^{\ 2} + \sigma_{ports}^{\ 2} + \sigma_{capsule}^{\ 2} \,. \qquad (12)$$

We find that the total nonuniformity varies from shot to shot due to the stochastic nature of the first two components, between a minimum of about 0.5% and a maximum of about 1.5%, with a mean value a little less than 1%. The port location contribution is typically less than 0.2%, the power and profile error contributions are about 0.4% each, and the pointing contribution is about 0.7%. The fact that the nonuniformity is not dominated by the port locations allows greater freedom to select the port locations without compromising the nonuniformity. Consequently the direct-drive constraints on the port locations are relatively benign.

3.2.1 Target Chamber Port Locations

A fundamental constraint on the port locations is that no ports can be diametrically opposed because of the possibility of optical damage from backward-traveling 1ω light in the laser. This constraint is a consequence of the fact that in the NIF, the residual 1ω and 2ω light enters the target chamber through the same ports as the 3ω light. If the unconverted light could be prevented to a high degree from entering, this constraint would not apply. Several options exist, such as locating the frequency conversion arrays far from the tank wall as in the Omega and Laser Megajoule designs. Separation is achievable with gratings, and possibly a spatial filter. The NIF cost is minimized with the frequency conversion arrays on the target chamber. Then we must arrange for space for the beam dumps between the ports. A cone or ring of ports at angle θ containing N ports of diameter D fills a fraction FF of the ring length, where

$$FF = \frac{D}{R}\frac{N}{\pi \sin\theta}. \tag{13}$$

Therefore the maximum number of ports on a ring (given by $FF = 1$) is

$$N < \frac{R}{D}\pi \sin\theta. \tag{14}$$

This is plotted in Fig. 3-1, for R/D = 3,4,5 and 6. The NIF target chamber has R/D of about 6. The two-cone indirect-drive illumination geometry has 8 and 16 beams in the

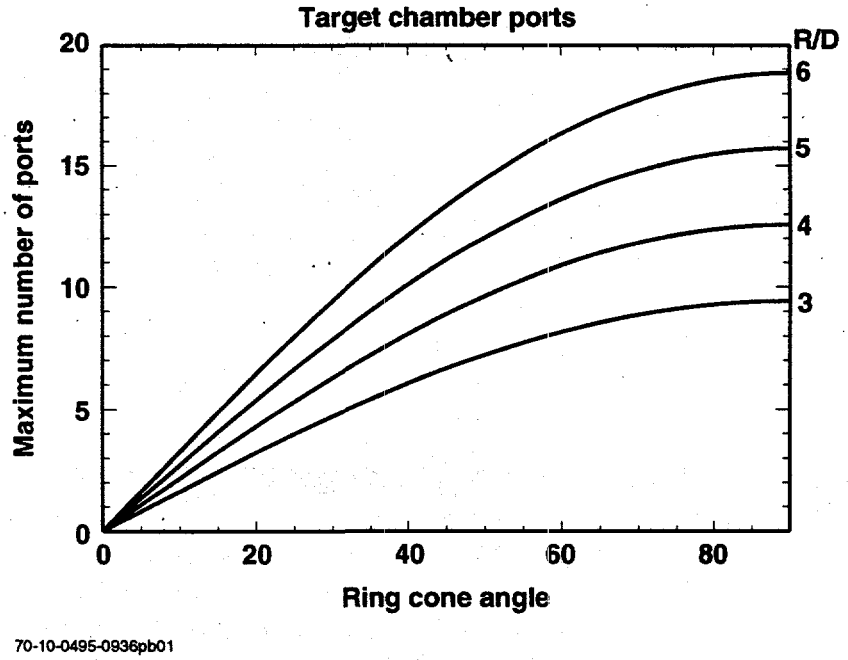

Figure 3-1. The maximum number of ports on a ring of the target chamber as a function of the ring cone angle and the size of the port. D = port diameter, R = target chamber radius.

rings, which must lie at large cone angles. With just two rings, the cone angles are generally incompatible with a range of hohlraum designs. Because of this, the NIF target chamber has four rings with 4,4,8 and 8 beams where each indirect-drive cone is split into two closely spaced rings. The CDR places these four rings at about 23°, 32°, 48°, and 57°. Within each ring the ports are spaced evenly: 90° for a 4- member ring, 45° for an 8-member ring. For a ring with a port on the line $\phi = 0$, the ports lie at azimuths $\phi_m = m\,(360/n)$, where m runs from 1 to n. In general, the NIF ports are rotated from these locations by $K(360/n)$, where K is the klick of the ring. A klick of unity brings the ring back to its original position, and corresponds to a rotation by its symmetry angle 360/n. Table 3-1 describes the baseline NIF port locations. The beam dumps of corresponding rings lie between the ports. Their distance to the nearest port is maximized if the klicks of corresponding rings in the upper and lower hemispheres differ by 0.5. Clearly, the baseline NIF port locations do not maximize this separation. The minimum angular separation between a beam dump and the nearest port is

$$\theta_{\min} = \frac{2\pi}{N}\left(|K - K'|\sin\theta - \frac{D}{\pi R}\right) \tag{15}$$

where ΔK is the difference in the klicks for corresponding rings. The condition for avoiding opposing beams is

$$\Delta K < \frac{1}{2}(FF)\,. \tag{16}$$

This is a design requirement on the target chamber. It is primarily a condition on the port size (R/D) rather than on the port locations.

The RMS intensity nonuniformity is

$$\sigma = \left[\frac{< I^2 >}{< I >^2} - 1\right]^{1/2}. \tag{17}$$

Table 3-1. NIF baseline port locations.

Ring	Ports	Polar angle	Klick
1	4	23.5	0
2	4	32.0	0.5
3	8	48.3	0.625
4	8	56.7	0.125
5	8	123.3	0.375
6	8	131.7	0.875
7	4	148.0	0.75
8	4	156.5	0.25

For a study of the port locations, the RMS nonuniformity is calculated using a hard sphere model. (For other laser parameters, such as the beam profile, this approximation will be inadequate. See Section 3.4). The NIF beams are assumed to be conditioned by phase plates. The speckle pattern of the beams near their focus exists over a distance substantially longer than the Rayleigh range of the focusing optics. The target is placed within this extended focus, near the minimum beam radius. The laser drive is the far field of the frequency-converted beam at the target focus lens, convoluted with the phase plate. Spatial nonuniformity in the laser such as what arises from non-optimal gain profiles gives rise to a long scale-length variation in the laser in the near field, which contributes to the near-forward far field of the beam. Because the beam divergence is much less than the angular aperture of the target, the phase plate determines the spatial profile of the beam on the target. Then to a good approximation, the near field nonuniformity of the laser is lost in the convolution with the phase plate. The same considerations apply to both indirect and direct drive. A selection of phase plates optimizes the beam size and profile at the target.

Without phase plates, the direct-drive target would be placed well in front of the focus, at a location where the beam diameter approximately matches the target diameter (tangential focus). Then the target lies in neither the near nor the far field, and it is possible that some long wavelength features of the near field profile (such as uneven energy between the left and right halves of a beamlet) will persist in the target profile. With phase plates, we can situate the target in the far field where this effect does not occur.

In this illumination scheme, the beams close to the target are essentially plane parallel (collimated) beams with strong spatial variation on the scale of the speckles. For studies of the port locations, we neglect the short wavelength speckle structure; we assume that each beam is a plane parallel beam directed towards the center of the pellet. The beam profile is then the envelope of the speckle pattern.

In the hard sphere model, the intensity on the pellet arising from a single beam is

$$I(\theta,\phi) = \cos\theta \; I_B \; (R_t \sin\theta, \phi). \tag{18}$$

$I_B(r,\phi)$ is the beam profile, R_t is the hard sphere radius, and (θ,ϕ) specifies a point on the sphere relative to the incoming beam direction (Fig. 3-2). The additional factor of $\cos\theta$ is a geometrical illuminance factor. We first write a spherical decomposition for the intensity in its own natural coordinate system, namely where the polar axis is along the central ray.

$$I(\theta,\phi) = \sum_{LM} B_{LM} Y_{LM}. \tag{19}$$

We then rotate the beam to its actual location on the sphere.

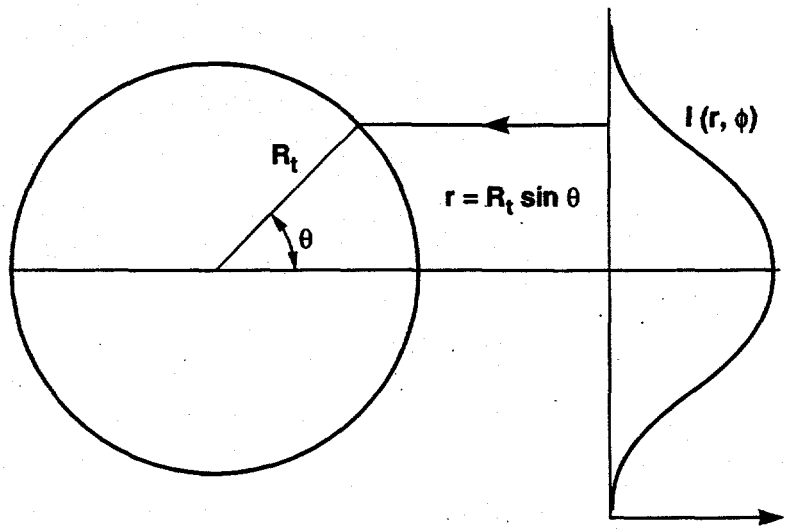

Figure 3-2. The hard sphere model of the pellet assumes that the rays of the laser beam propagate in straight lines to the sphere, where they deposit all their energy. A geometrical factor of cos θ relates the laser intensity to the intensity on the sphere.

$$I_j = \sum_{LM} B_{LM} d^{(L)}{}_{MM'}(R_j) Y_{LM'} \tag{20}$$

Here the d-coefficients are the rotation matrices for spherical harmonics and R_j is the rotation describing the location of the port relative to the apex of the target chamber at $(\theta, \phi) = (0,0)$. The total intensity is the sum of the intensities from each beam.

$$I = \sum_{LM} \left[\sum_{M'} B_{LM} D^{(L)}{}_{M'M} \right] Y_{LM} \tag{21}$$

where the D-matrix is a sum over the ports:

$$D^{(L)}{}_{MM'} = \sum_j d^{(L)}{}_{MM'}(R_j). \tag{22}$$

The average intensity is NB_{00}, and the nonuniformity of the beam is

$$\sigma = \frac{1}{NB_{00}} \left(\frac{1}{4\pi} \sum_{M,L=1}^{L=\infty} \left[\sum_{M'} B_{LM'} D^{(L)}{}_{M'M} \right]^2 \right)^{1/2}. \tag{23}$$

The nonuniformity clearly depends on the beam profile of the beams. If the beams are sharply peaked in the center, there is little overlap and the intensity varies from zero to the peak. If the beams have a hard edge, then the intensity changes rapidly at the boundaries, which is undesirable. However, while the magnitude of the nonuniformity

may depend on the beam profile, the configuration that minimizes the uniformity is independent of the beam profile, within some very general restrictions. Determining the optimum configuration can then be accomplished for any profile that meets these conditions.

To see the role of the beam profile, we note that the optimum configuration is evidently given by

$$\frac{\partial \sigma}{\partial R_j} = 0 \tag{24}$$

or

$$0 = \sum_{M,M',M'',L=1}^{L=\infty} B_{LM'} B_{LM''} D^{(L)}{}_{M'M} \frac{\partial D^{(L)}{}_{M''M}}{\partial R_j}. \tag{25}$$

For cylindrically symmetric beam profiles, only the $M = 0$ elements of B_{LM} are nonzero. Then

$$\sigma^2 = \frac{1}{N^2} \sum_{L=1}^{L=\infty} B_{L0}^2 \left[\frac{1}{4\pi} \sum_{M} D^{(L)2}{}_{M0} \right]. \tag{26}$$

The optimum configuration minimizes each $D^{(L)}{}_{M0}$ for each mode contained in the beam. If the beam has L modes, there are L functions to minimize with N beam parameters as variables. If the beam has only a few modes (much less than the number of beams), the result of the minimization will be stable, and by inspection, independent of the mode amplitudes. Therefore, for beam profiles that are relatively smooth with only a few modes, the optimum port configuration will be independent of the actual beam profiles.

For the optimization procedure, we choose a beam that has a $\cos\theta$ profile. Using this profile and the indirect-drive port locations, the nonuniformity is large ($\sigma = 0.235$) because they do not provide equatorial illumination. We note that for a uniformly bright sky (such as the inside surface of the target chamber) or spherically symmetric illumination, the power profile of the sky is proportional to $\sin\theta$. Then for uniform illumination, we would expect the number of beams in a ring to increase monotonically with angle. This suggests that we must move at least eight beams closer to the equator. Table 3-2 shows the improvements in uniformity achieved by moving eight beams, four at a time, to a fifth ring. Moving four beams from rings 3 and 4 leaves four remaining. The remaining four must be equally spaced; we can move the even numbered beams leaving the odd numbered beams [case (o)] or vice versa [case(e)]. The resulting uniformity is quite good and meets the target requirement in all cases. Another degree of freedom is the klick of the fifth ring. For an eight member ring the uniformity is relatively insensitive to its klick, and is not important. Access to the diagnostics around the equator is easier if the fifth ring angle is smaller. On that basis, the most attractive eight-move

Table 3-2. Nonuniformity moving eight beams to a fifth ring.

N1	N2	N3	N4	θ_{5opt}	σ(%)
4	0	4(o)	8	76.2	0.16
4	0	4(e)	8	76.2	0.35
4	0	8	4(o)	>88	<0.6
4	0	8	4(e)	>88	<0.6
0	4	4(o)	8	70.0	0.21
0	4	4(e)	8	70.0	0.45
0	4	8	4(o)	77.5	0.20
0	4	8	4(e)	77.4	0.38

N1 = number of ports in the first ring, etc.

Table 3-3. Nonuniformity moving 12 beams to a fifth ring.

N1	N2	N3	N4	θ_{5opt}	σ(%)
0	4	0	8	61.6	0.18
0	4	8	0	68.8	0.17
4	0	0	8	64.4	0.16
4	0	8	0	72.4	0.12

option is to move all the beams from the top ring at 23.5°, and to move the even numbered beams from the third ring at 48.3° to a fifth ring at about 70° for a uniformity of 0.21%. Note that the top ring is then not used in direct drive, and can be fixed by the indirect-drive requirements alone.

Another option is to move twelve beams to a fifth ring. These results are summarized in Table 3-3. The uniformity is generally better than with moving eight beams. On the basis of requiring the fifth ring to fit between the fourth ring at 56.7, and the equatorial plane diagnostics, all these options are probably satisfactory. Moving 12 beams allows a better separation between direct and indirect drive requirements. It is possible to choose the scheme so that direct drive does not interfere with the two most critical indirect drive rings.

Figures 3-3 to 3-5 show the nonuniformity as a function of the angles of the 4-ring and 8-ring, assuming that the 12-ring angle has been optimized. We used a $\cos\theta^{1.125}$ beam profile and klicks (0, .5) for the 4-rings, (.5, 0) for the 8-rings and (.625, .125) for the 12-rings. Figure 3-3 shows the 12-ring angle that minimizes the nonuniformity. Figure 3-4 shows the lowest achievable nonuniformity, and Fig. 3-5 shows the linear deviation of the intensity over the pellet, defined as

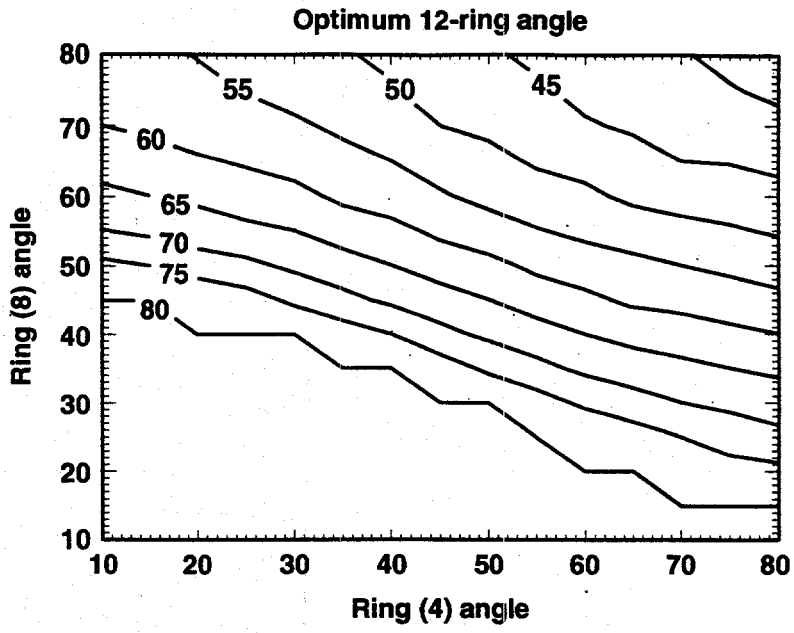

70-10-0495-0900pb01

Figure 3-3. The optimum 12-ring cone angle for a 4/8/12 illumination geometry. Angles greater than 80° are excluded, because such rings tend to interfere with equatorial access to the target chamber.

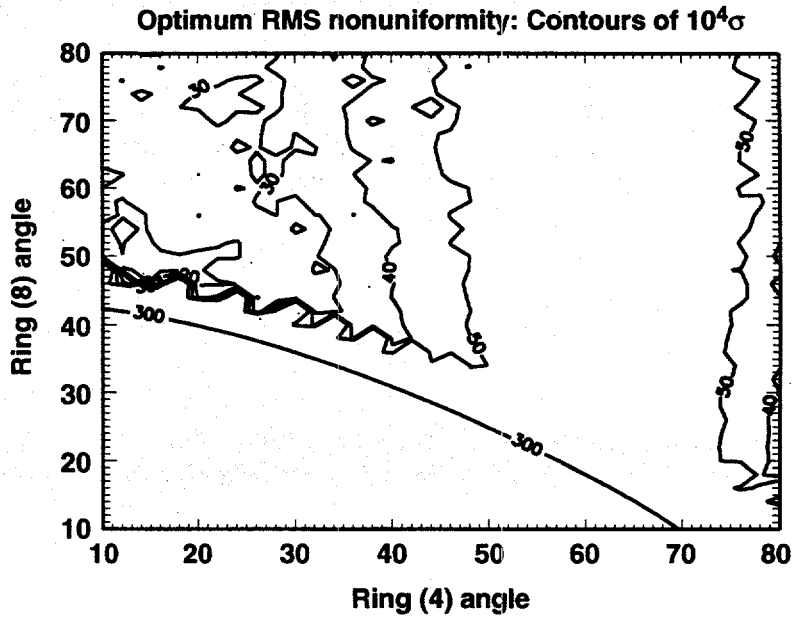

70-10-0495-0901pb01

Figure 3-4. The optimum RMS uniformity for beams with a cosθ profile, at the klick angles given in the text. The optimum region where σ < 0.2% is confined to a small region around the point (20,45).

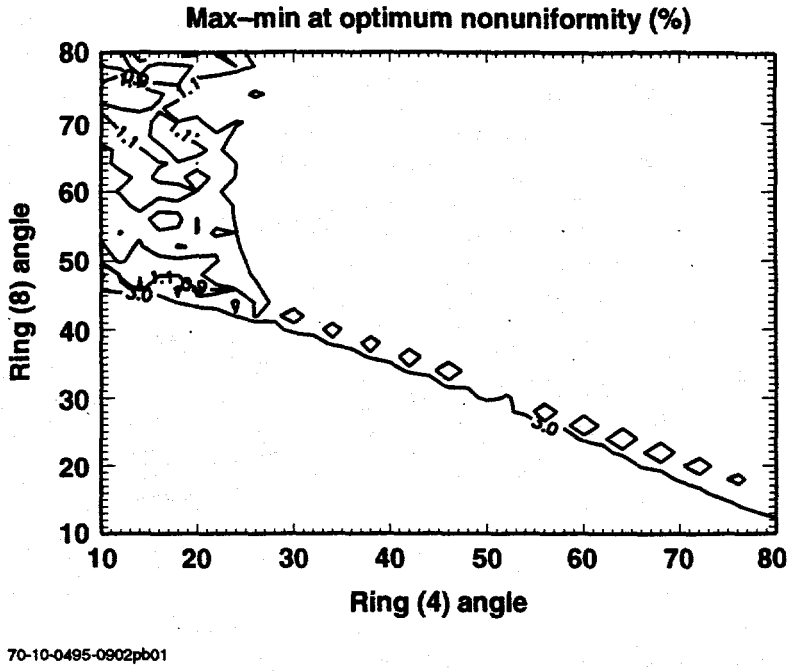

Figure 3-5. The linear deviation of the intensity distribution. In the optimum region of the plot, the intensity on the sphere is flat to better than ±0.5%.

$$D = \frac{I_{max} - I_{min}}{I_{min}} \tag{27}$$

Clearly there is only one interesting region in (θ_4, θ_8) space. This region is explored in Figs. 3-6 to 3-8. The figures show the region (16–24,40–60). The nonuniformity is a very uneven function, but the linear deviation is relatively flat. There is a line of minima close to the line $\theta_8 = 42.5–0.03\ (\theta_4–20)$, where the nonuniformity is very low (about 0.08%), but the associated 12-ring angles are large (about 85°), and the minima are extremely narrow. There are better points for direct-drive experiments that lie at higher values of θ_8, between 45° and 50°. The linear deviation over much of this region is about ±0.5°. The deepest minimum is sensitive to the klicks of the rings. Figures 3-9 to 3-11 present results for klicks (0, .5), (.5, 0) and (.25, .75) in the optimum region. The very uneven nature of the nonuniformity is evident. The deepest minimum for these klicks is about 0.12%, and one such minimum, occurs at (21.5°, 46°, 76°). However, values less than 0.2% occur over a wide range of ring angles. The linear deviation is ±0.35 % over most of this region. The minima are about a degree wide, as illustrated by the sensitivity ellipsoid, shown in Fig. 3-12. This ellipsoid is the surface σ = 1%. Its major axes are given in Table 3-4.

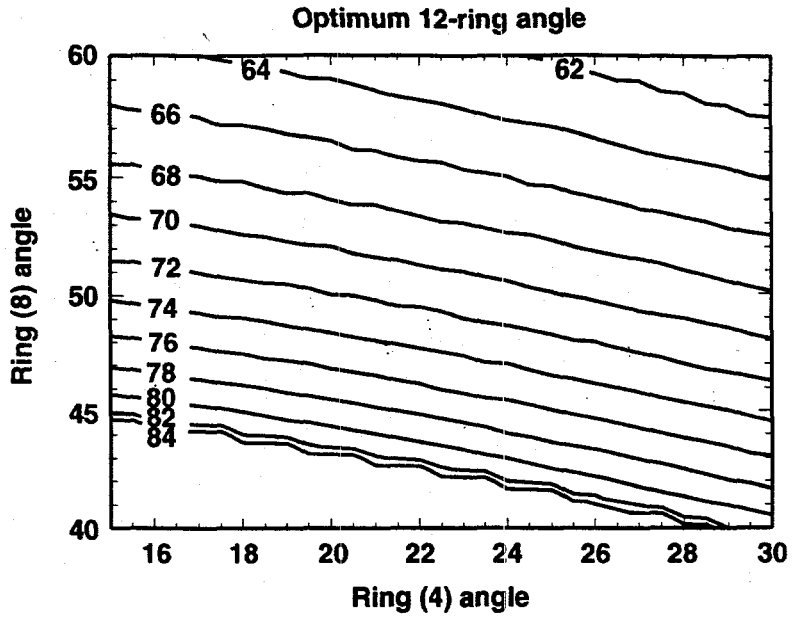

Figure 3-6. Detail of Fig. 3-3.

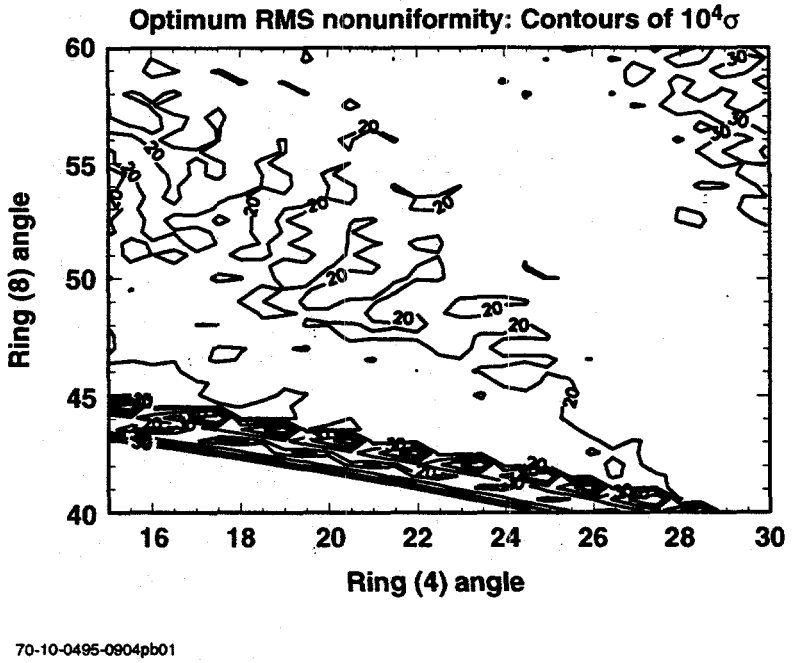

Figure 3-7. Detail of Fig. 3-4.

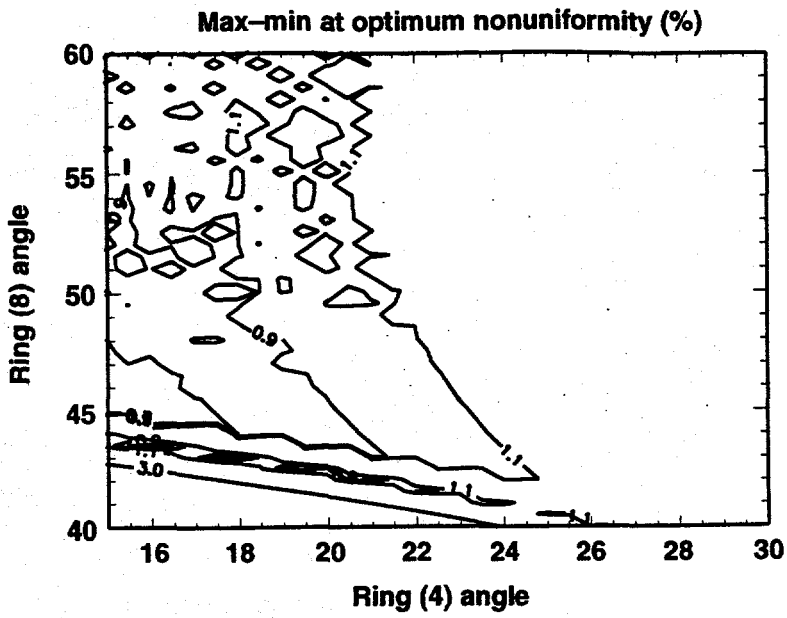

70-10-0495-0905pb01

Figure 3-8. Detail of Fig. 3-5.

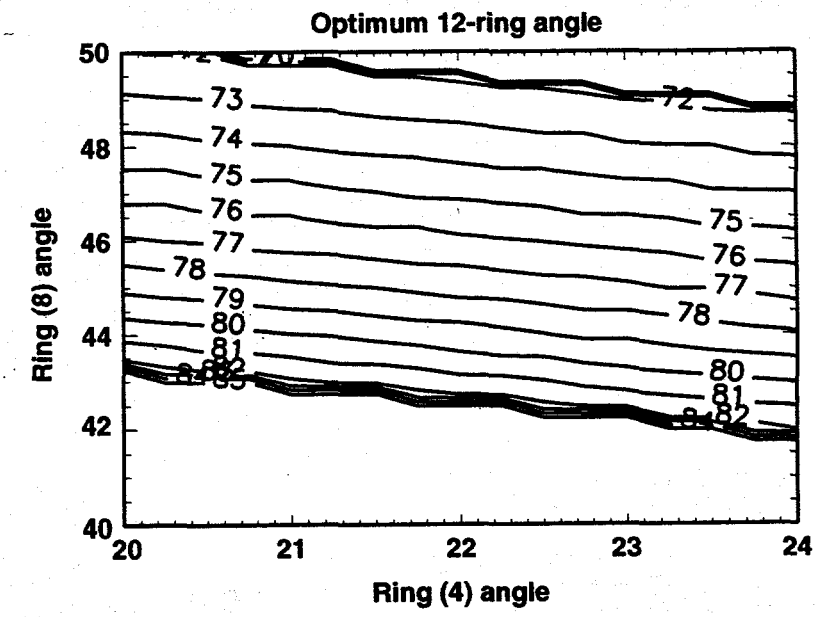

70-10-0495-0906pb01

Figure 3-9. Detail of Fig. 3-3.

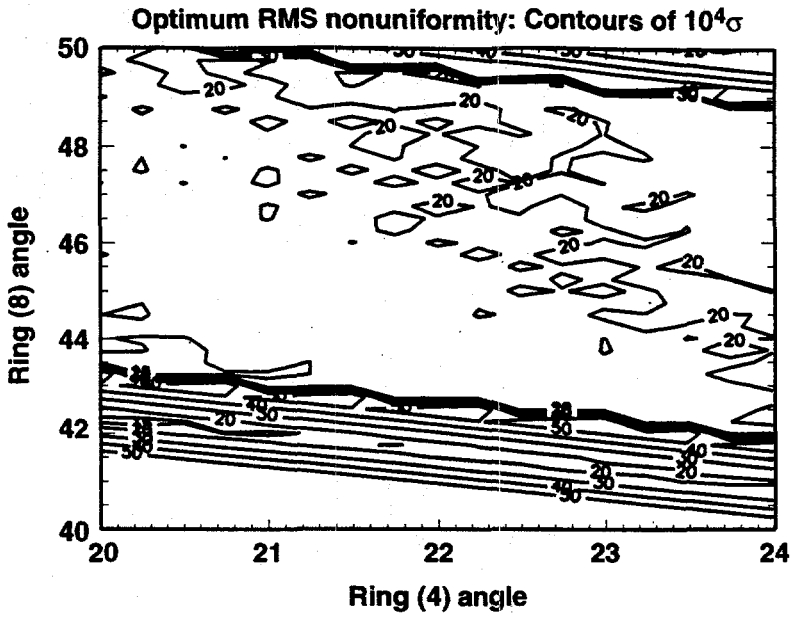

70-10-0495-0897pb01

Figure 3-10. Detail of Fig. 3-4, showing the region of greatest interest to indirect-drive experiments. The region of maximum uniformity is quite uneven, and is about 0.2% over most of this plot. The nonuniformity is less than 0.2% in the broad spaces between the 0.2% islands. This allows considerable freedom in the choice of indirect drive port angles.

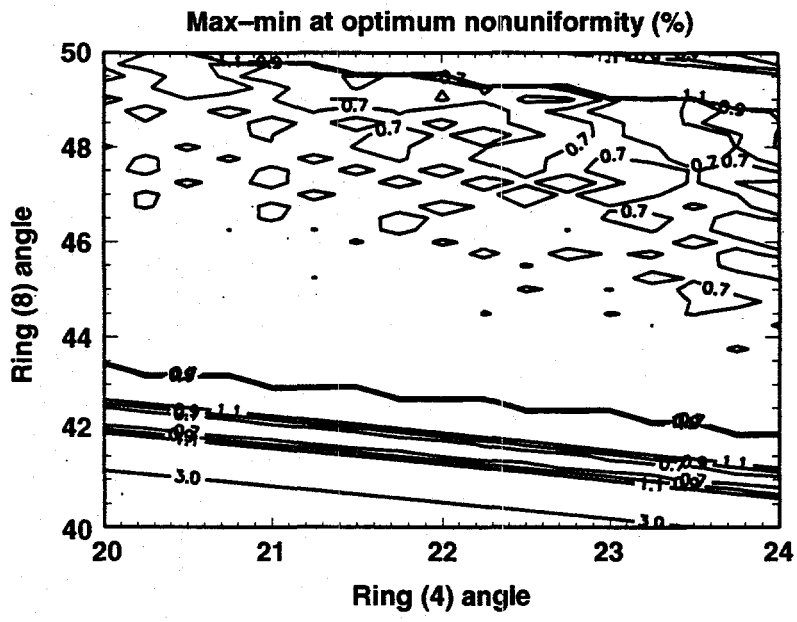

70-10-0495-0898pb01

Figure 3-11. Detail of Fig. 3-5.

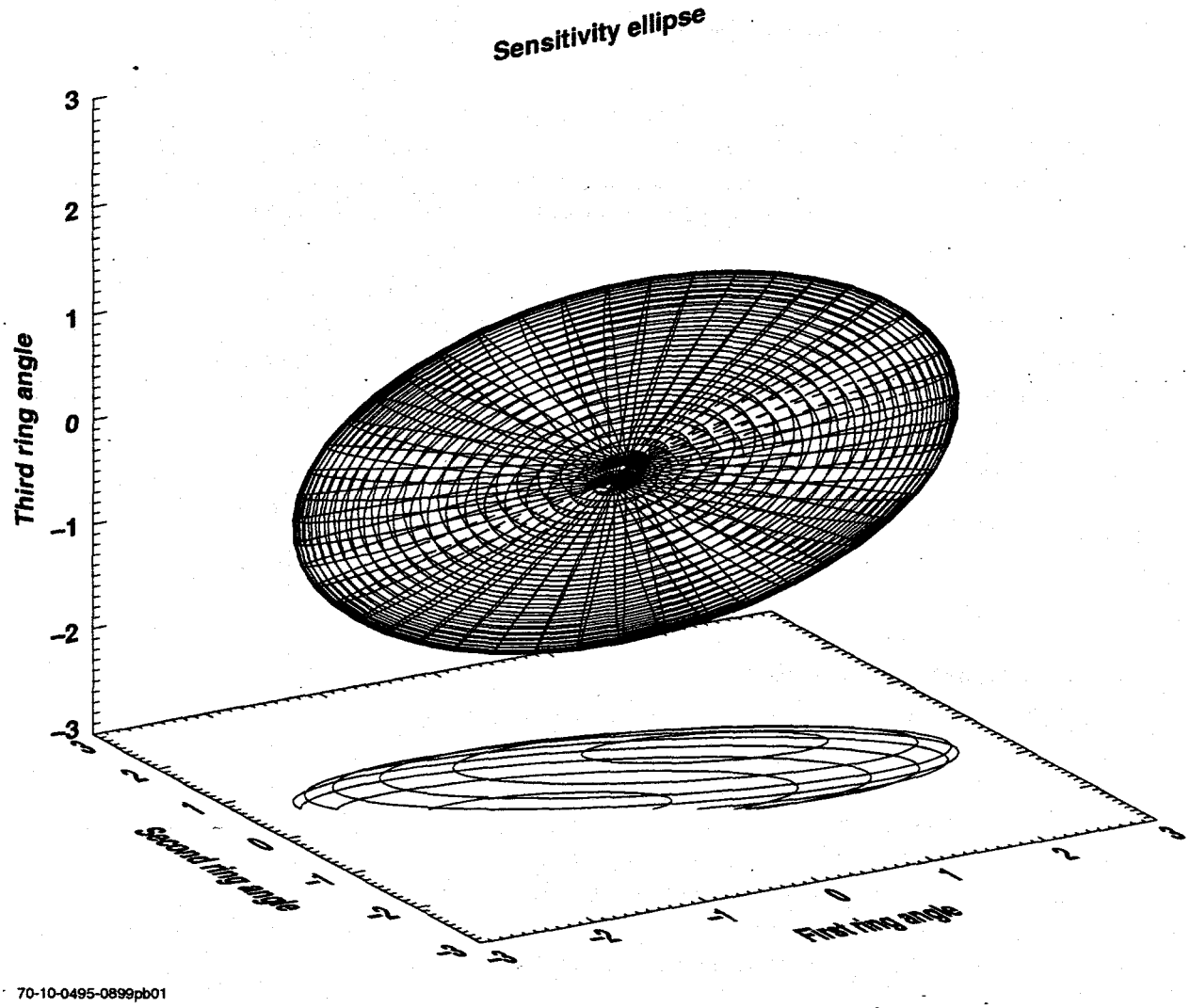

Figure 3-12. Sensitivity ellipse for the point (21.5, 46, 75.75). This is used in the text to estimate the nonuniformity arising from pointing errors.

Table 3-4. Major axes of the uniformity sensitivity ellipsoid.

Axis	u	v	w	d(°)
1	0.949945	-0.078937	-0.302279	2.7023
2	-0.197469	0.598057	-0.776745	1.5562
3	0.242094	0.797556	0.552534	0.7797

3.2.2 Nonradially Directed Beams

In principle, it is possible to use the indirect-drive ports for direct drive, if each beam is directed nonradially so that its apparent position on the target is close to the desired highly uniform configuration. This can obviously be achieved at any one fixed target radius, if the beam profile of each non-radial beam is precompensated to give the appropriate profile on the target. However as the target implodes, the critical surface where much of the laser energy is absorbed moves in by about a factor of two. Nonradial beams directed at an angle θ to a radius will change their apparent position by $\phi = \arcsin(R \sin\theta/r) - \theta$ as the absorption radius decreases from R to r. Our previous analysis of the sensitivity to apparent position indicates that the apparent position must remain constant to within a degree or so during the implosion so that the nonradial angle θ is also limited to about a degree. This is not enough to avoid adding more ports to the target chamber. It is preferable to use radially directed beams from ports close to the optimum locations. The possibility of using nonradial beams is a degree of freedom that might permit the fine-tuning of the illumination geometry at an advanced stage of the experimental campaign, but we should not rely on nonradial beams as the main strategy for achieving uniform illumination.

3.2.3 Beam Pointing and Power Balance

While it is possible in principle to plan to reach the optimal uniformity illumination geometry in NIF direct-drive experiments, the nonuniformity achieved will be sensitive to the actual beam profile, and also to pointing and power balance errors. From Fig. 3-10, the nonuniformity throughout the region of interest is around 0.2%, and this is a reasonable figure to take as the average value that the NIF will achieve in the absence of beam pointing and power balance errors. Note that if we take 0.2% as the expected baseline the acceptable error in the apparent angular position of the beams is greater than the value obtained from the sensitivity ellipsoid.

Each beam has a positioning error of S, which is taken to be the CDR value 0.05 μm rms. Moving a beam by S on the capsule corresponds to a change of S/R in its apparent position, where R is the target radius. The baseline direct-drive target absorbs the laser light at about r = 1.5 mm initially and at about r = 0.8 mm at ignition. Therefore as a result of mispositioning, a beam may change its apparent position by up to 0.033 rad for a 1.5-mm radius target or 0.065 rad for a 0.8-m target. The RMS nonuniformity from the beam pointing error can be estimated as

$$\sigma_\theta = \frac{S}{R d_{av}} \sqrt{\frac{3}{N_{eff}}} \qquad (28)$$

where d_{av} is the sensitivity scale, which we take to be similar to the size of the sensitivity ellipsoid, and N_{eff} is the effective number of overlapping beams at any one point on the pellet. N_{eff} has been calculated to be about 13 for 48 independent beams and 52 for 192 independent beams. For $d_{av} = 1°$ and 48 independent beams the nonuniformity is 1.2% at R = 1.5 mm and about 2.1% at R = 0.8 mm. The pointing error is a factor of two smaller for 192 independent beams. The total nonuniformity is the RMS of the pointing

error and the port location contribution, and is dominated by the pointing error contribution. This estimate of the pointing nonuniformity is conservative because the sensitivity ellipsoid overestimates the actual sensitivity of the nonuniformity to beam mispointing.

For the beam profile and power balance, we write the total intensity on the pellet as

$$I = I_0 + \Delta I \tag{29}$$

where the error is ΔI. For the power balance, the asymmetry in the drive on the pellet is almost completely in the low L-modes. However, the beam profile nonuniformity for all spatial wavelength is essentially unity because the beam profile is a speckle pattern. The relevant part of the profile is just the long wavelength part. Evidently the long wavelength part of the beam profile contributes in the same way to the nonuniformity as the power imbalance. In one approximation to the beam profile error, each beamlet can be divided into four quadrants and the power in each quadrant treated as independent. Then the effect of a profile error of 8% is the same as that of a power imbalance error of 4%. For shorter wavelength terms in the profile error, the number of effective beams increases rapidly. Therefore we might assume that an upper bound on the profile error contribution is about 1/2 of the energy balance result, for the same RMS error for one beam.

Simple kinematic considerations suggest that the nonuniformity arising from power imbalance is simply related to the RMS power variation over the beamlets. If N_{eff} beams overlap at any given point on the capsule, the RMS intensity nonuniformity is essentially $\sigma_E\,(1/N_{eff})^{1/2} = 2\sigma_E/7$ for 48 beams. Then a 2% nonuniformity would be expected from a 7% rms power variation per cluster, or a 14% rms power variation per beamlet. According to the provisional model of the beam profile, the RMS power variation must be reduced by 1.41 to give the same nonuniformity when beam profile errors are included.

Note that the pointing errors of the four beams in a cluster may be correlated; there may be less than 192 degrees of freedom for the pointing. For the power, the 192 beams are probably uncorrelated. The correlations are clearly significant and can affect the nonuniformity by up to a factor of two. Further work on the correlations is advisable. Nonetheless, these simple estimates suggest that the nonuniformity from beam pointing and power balance individually can each be about 0.7% and larger than the illumination nonuniformity, which is about 0.2%. The quadrature sum of these three contributions is about 1% and evidently meets the target requirements.

We have tested these approximations by calculating the nonuniformity including shot-to-shot errors in both the apparent angular position, and the power of the 48 clusters. A number of shots (256) were simulated varying the beam locations and beam energy on a shot-by-shot basis using a Gaussian probability distribution. The results are

summarized in Table 3-5 for the standard ring minimum (21, 46.5, and 75.75), for which $\sigma = 0.15\%$ for a $\cos\theta$ intensity distribution. If only 48 degrees of freedom are used, then the baseline specifications on the pointing and power balance lead to a mean nonuniformity of (2.65 ± 0.6) %. The peak nonuniformity is 4.6% and the minimum is 1.2%. If we argue that there are 192 degrees of freedom (no correlations) in both the pointing and the beam power errors, then the mean nonuniformity drops to $(1.3 \pm 0.3\%)$, and extremes are 2.3% and 0.6%. Partial correlations between the beamlets give intermediate results. Some partial correlation between the beams is expected but remains to be estimated. Even with the assumption that the error correlations will be weak, it can be concluded that the NIF CDR specifications will just fail to meet the target uniformity requirement of $\sigma < 1\%$, given this conservative approach.

The individual effect on nonuniformity produced by power imbalance is shown in Fig. 3-13. Conditions with the same RMS variation in energy can produce a relatively large spread in nonuniformity, as indicated by the bars, but it is all long wavelength

Table 3-5. Shot statistics and uniformity.

	192 beams	48 beams
Beam power RMS variation (%)	8	8
Beam position RMS variation (μm)	50	50
Beam location RMS (degrees) (R = 0.8 mm)	7.2	7.2
Mean nonuniformity (%)	1.3	2.65
Maximum nonuniformity (%)	2.3	4.6
Minimum nonuniformity (%)	0.6	1.2
RMS variation in the nonuniformity (%) (256 shots)	0.30	0.60

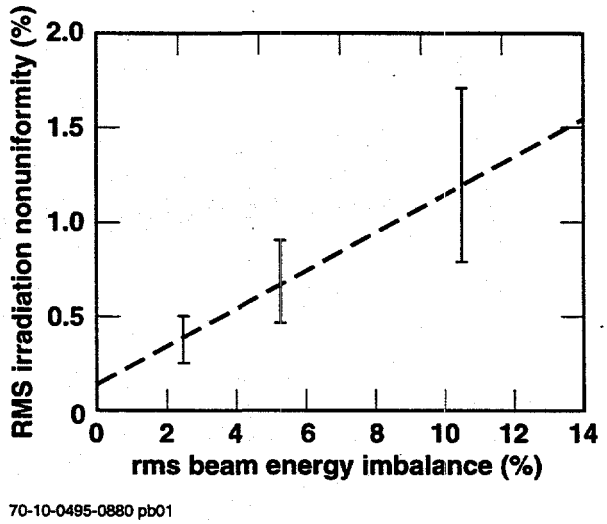

Figure 3-13. RMS nonuniformity increases linearly with RMS energy imbalance.

structure corresponding to low L-modes. The calculations for Fig. 3-13 assumed that there was no correlation between the powers of beamlets within a cluster and no correlation between clusters. Power variations among the 192 beamlets were treated as statistically independent. Typically, the RMS nonuniformity was found to be less then 0.5% when the power imbalance was below 5% RMS.

The individual effect of beam mispointing is shown in Fig. 3-14. All beamlets within a cluster were assumed to be completely correlated. The cluster mispointing was chosen as a random number between zero and a maximum value (shown on the horizontal axis). The spread in nonuniformity for different random configurations is shown by the bars, and the nonuniformity is all in long wavelength modes. The RMS nonuniformity is 0.5% for a circle of error of about $S = 5\%$ of the radius, or 40 μm at $R = 0.8$ mm and 75 μm at $R = 1.5$ mm.

Capsule positioning errors in Fig. 3-15 create nonuniformity primarily in the L = 1 mode. The radiation nonuniformity is less than 0.5% if the target is positioned to within 1% of its radius.

From these calculations we can describe the mean nonuniformity as

$$\sigma_{mean}{}^2 = \sigma_0^2 + \left(\frac{0.8}{R_t} a_t\right)^2 \left(\frac{\Delta c}{\Delta c_0}\right)^2 + \frac{48}{N}\left[\left(\frac{0.8}{R_t} a_s\right)^2 \left(\frac{\Delta s}{\Delta s_0}\right)^2 + a_E{}^2 \left(\frac{\sigma_E}{\sigma_{E0}}\right) + a_P{}^2 \left(\frac{\sigma_P}{\sigma_{P0}}\right)^2\right] \quad (31)$$

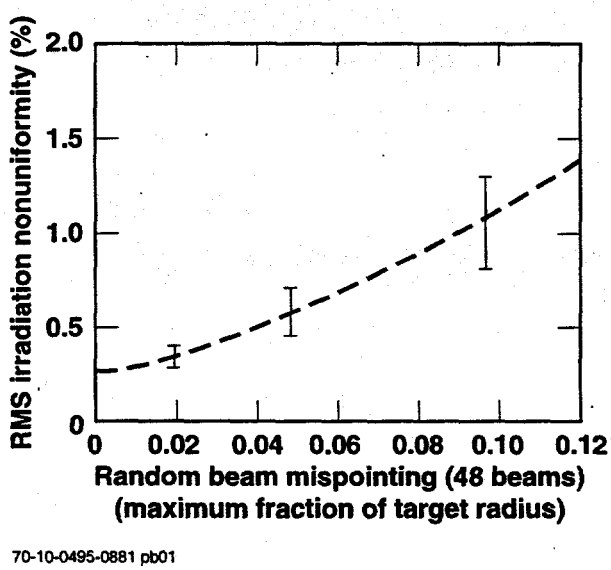

Figure 3-14. RMS nonuniformity increases almost linearly with RMS beam mispointing.

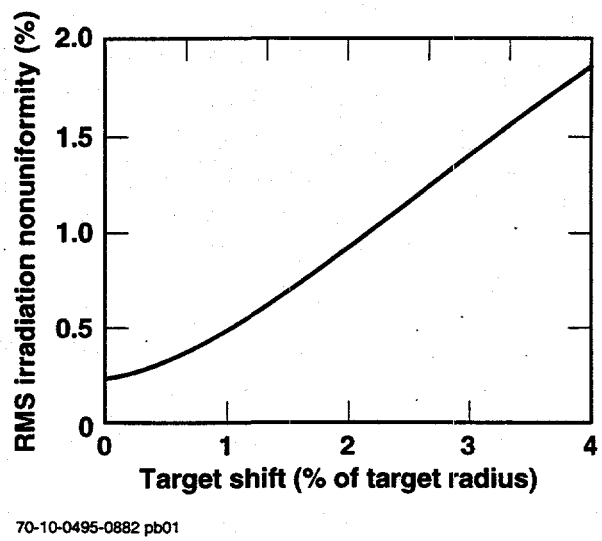

Figure 3-15. RMS nonuniformity increases with capsule misplacement.

where σ_0 is the intrinsic uniformity associated with the port locations, and Δs, σ_E, and σ_p are the RMS variation in the position, and the normalized RMS variation in the energy and beam profile of an individual beamlet. The target positioning error is Δc. It is a separate contribution to the beam positioning error and must be included separately. The pointing contribution depends on the assumed target radius R_t. The other parameters are $\sigma_0 = 0.2\%$, $a_t = 1.0\%$, $a_E = 0.88\%$, $a_s = 1.0\%$, and $\Delta c_0 = 18$ μm, $s_0 = 25$ μm, $\Delta E_0 = 4\%$. At present, we do not have quantitative results for the effect of beam profile errors, but according to a simple model given above, we expect that $a_p < (1/2)\, a_E = 0.88\%$, for $\Delta p = 4\%$ in the appropriate part of its spatial spectrum. Clearly, the intrinsic nonuniformity is much smaller than the error contributions, implying that positioning the ports correctly is not very significant for direct-drive uniformity, but that the beam parameters and target positioning are critical.

For the baseline NIF parameters for 192 uncorrelated beamlets, the RMS uniformity is about 1.5%. During the foot, when the target radius is 1.5 mm, the pointing error is smaller, and the uniformity is reduced to 1.3%. Table 3-6 presents representative specifications under various assumptions about the relevant target radius and beamlet correlations.

This table illustrates that the baseline specifications on pointing and energy balance will essentially meet the uniformity requirements for the foot, if all the beam errors are uncorrelated. The CDR error specifications give $\sigma_L = 2\%$ for the final target radius. If the beam errors are completely correlated, the specifications become significantly tighter. If the power balance is specified at 2% final target radius, and the pointing specification remains at 50 μm, then the resulting RMS nonuniformity is only 1.15%.

Table 3-6. Low L-mode irradiation uniformity: laser specifications for σ_L = 1%.

	Target Position (μm)	Position error (μm RMS)	Power balance (%)	Profile error (%)
Indirect drive/NIF baseline	25	50	8	n/a
Final radius/48 uncorrelated beams	7	20	2	2
Final radius/192 uncorrelated beams	7	40	4	4
Foot/48 uncorrelated beams	7	40	2	2
Foot/192 uncorrelated beams	7	60	6	6

Figures 3-16 and 3-17 show contours of σ_{mean} = 1%, for various assumptions about the relevant target radius and number of independent beams. For Fig. 3-16 the target positioning error is 7 μm, and for Fig. 3-17 the target positioning error is 15 μm. These illustrate that for 192 independent beams, the baseline specifications almost meet the target requirements. But for 48 independent beams, the laser tolerances must be about a factor of two tighter.

At this point, it must be noted that the hard sphere model for the uniformity is expected to be accurate only when the target corona is a thin atmosphere, at early times. At early times in the foot, we find that the baseline specifications will meet the uniformity requirements. It is not clear that the hard sphere model does not overestimate the nonuniformity in the pressure when the corona is well-developed. This effect of the corona on uniformity is a subject of ongoing investigation; it is discussed in the context of a particular model of refraction and electron transport in a later Section 3.3. During the main pulse, the critical surface becomes widely separated from the ablation front, affording the opportunity for significant conduction smoothing. This effect is not yet quantitatively understood, but there is good reason to believe that the uniformity requirements in the main pulse may well be less stringent than during the imprinting phase. In that case, the baseline NIF specifications might be expected to meet the uniformity requirements at all times in the pulse.

We note that the condition on the uniformity is a condition on the time-integral of the intensity. For the low L-modes, the relevant time integral is between 300 ps and 1 ns. If each beam pulse shape is set independently, and if the time step in the programming of each pulse shape is shorter than the relevant integration time, the number of independent (stochastic) variables in the power imbalance contribution to the nonuniformity is increased in the ratio F_{pr} = (integration time) / (pulse shaping time interval). Then the contribution of the energy imbalance to nonuniformity is reduced by $(1/Fpr)^{1/2}$. This effect increases the permissible instantaneous energy imbalance, by a factor that could be as much as 1.5–2. Note that the same effect is produced if two (or more) independently adjusted pulse shapers are used for each beamlet, and if their output is averaged.

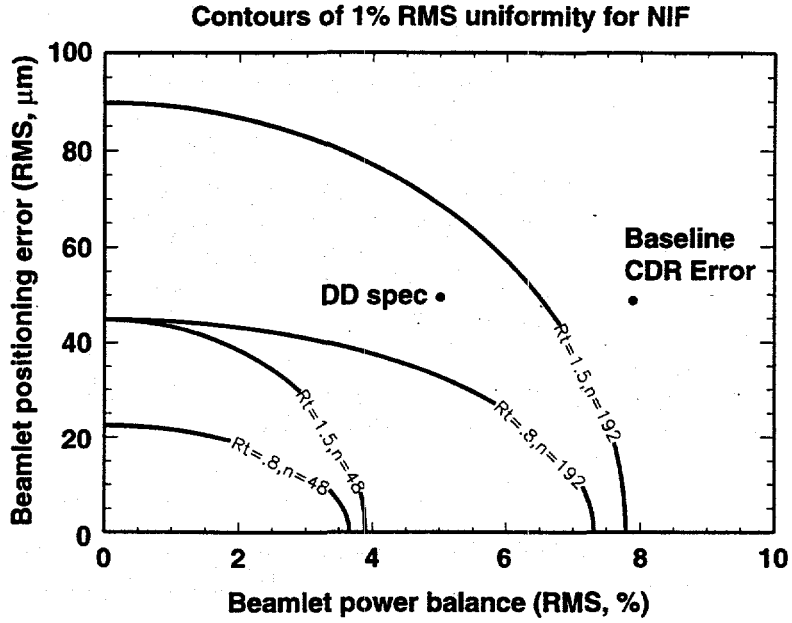

70-10-0495-0964pb01

Figure 3-16. Contours of 1% nonuniformity as a function of the beam positioning and power balance of a beamlet. The target positioning error is 7 μm. For the case of 192 beamlets, the baseline specifications just fail to meet the 1% requirement.

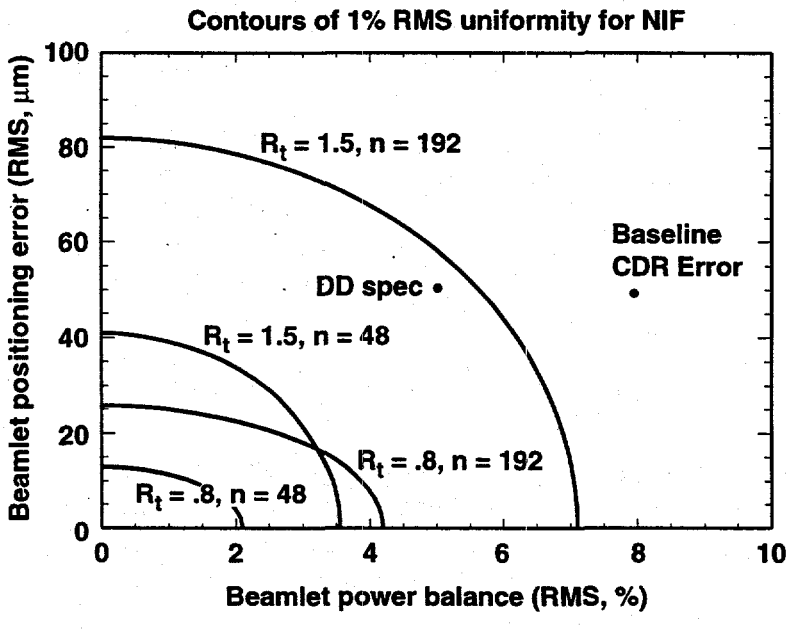

70-10-0495-0965pb01

Figure 3-17. As for Fig. 3-16, but where the target positioning error is increased to 15 μm. For this case, the baseline specifications are inadequate to meet the target requirements.

We also note that we have taken the uniformity requirements for the end of the main pulse to apply throughout the main pulse. However, as the pellet implodes, the effect of the positioning error increases in time. Its effect is greatest at the end of the pulse, where its influence on the capsule dynamics is weakest. If an appropriately weighted time-averaged uniformity is used instead of the end-point condition, then the effect of beam mispositioning is reduced.

There are evidently several effects that could improve the uniformity during the main pulse, including conduction smoothing, coronal refraction, and integration time effects. Taken together, they might relax the beam specifications enough so that the CDR error tolerances provide adequate uniformity throughout the pulse. We judge that the least stressing option for tightening the NIF laser specifications is to set the power imbalance between individual beams at 5%, rather than 8%. The profile error is also set at 5%, but the beam pointing specification remains at 50 μm. This choice leaves some margin without causing operational complexity.

3.2.4 Compatibility with Hohlraums

The most complete separation between the direct- and indirect-drive requirements for the port locations is for direct drive to use as few of the indirect drive ports as possible. Greatest separation is accomplished with the 4/8/12 design for direct drive, which has only two rings in common with indirect drive. Recognizing that the nonuniformity is not dominated by the port locations, we can then set a more relaxed tolerance on the nonuniformity arising from the port locations alone, σ_0. If this is set at around 0.2%, then the two common rings need only lie in the range (20°–24°) for the common 4-port ring, and 45°–50° for the common 8-port ring. The fifth ring lies between 75° and 85°. The klicks of the rings must be set to minimize σ_0. The klick for the 8-member ring is more important than for the 12-member ring, but neither is severely constrained. There are no other constraints on the port locations from direct-drive uniformity requirements.

Within the 4/8/12 strategy, we can also envision using other subsets of the 72 ports to drive other hohlraums. In particular, the possibility of driving hohlraums with four laser entrance holes, or tetrahedral hohlraums,[5] has been analyzed. Tetrahedral hohlraums use ports from all five rings, and the klicks of all the rings are significant. Table 3-7 lists the klicks for both an improved baseline design and a tetrahedral configuration. For the tetrahedral configuration the intrinsic nonuniformity for direct drive is between 0.12% and 0.15%, depending on the beam profile, well within the relaxed constraint of 0.2%. The tetrahedral hohlraum driven by these ports is distorted from the most symmetric arrangement, yet achieves an attractive uniformity within the hohlraum.

3.3 Beam Profile on the Capsule

The beam profile of an individual beam on the target must be shaped to optimize the uniformity of the drive. The pressure profile is related to the three-dimensional energy deposition profile resulting from inverse bremsstrahlung absorption of the laser.

Table 3-7. Port locations suitable for 2-LEH and 4-LEH indirect drive and direct drive.

Ring	Polar angle	Klick DD/ID$_2$	Klick DD/ID$_2$/ID$_4$
1	21	0	0
2	33	0.125	0.5
3	46.5	0.5	0.25
4	58	0.25	0.75
5	76	0.25	0
6	104	0.75	0.5
7	122	0.75	0.25
8	133.5	0	0.75
9	147	0.625	0
10	159	0.5	0.5

The deposition profile is the sum of the energy deposited by each beam, and each beam gives rise to an energy deposition rate that is strongly influenced by plasma refraction. The beam profile at the target must be such that sufficiently uniform pressure is maintained at all times in the implosion. Because we expect to have only a limited ability to dynamically shape the beams, the dynamics of the uniformity arises mostly from the evolving plasma refraction. Uniformity will then be achieved in a time-integrated sense rather than an instantaneous sense.

Each individual beam is conditioned by a phase plate and by SSD. The beam diameter at the focal plane of the target focus lens is approximately equal to the target diameter. Thus,

$$D_t / F = \theta_{SSD} + \left(\theta_{ph}^2 + \theta_0^2\right)^{1/2} \qquad (32)$$

where D_t is the target diameter, θ_0 is the beam divergence (FWHM) without a phase plate and in the absence of SSD and bandwidth, θ_{ph} is the divergence generated by the phase plate from a uniform beam, and θ_{SSD} is the added divergence associated with SSD.

Table 3-8 lists the phase plate parameters for targets of different diameter. The ignition target diameter is between 2 and 4 mm, and we assume that the required asymptotic smoothness is the same for all targets. Also we require that the phase plate divergence should be significantly larger than the beam divergence if the far field profile is to be controlled by the phase plate. The central portion of the target profile is essentially unaffected by the beam profile, but the slope of the profile in the wings is essentially limited by the slope of the beam profile. Calculations of the sensitivity of the RMS nonuniformity suggest that it is not very sensitive to the wings of the profile. Rather, it is controlled mostly by the shape of the central lobe. Then the beam profile is a weak

Table 3-8. Beam size requirements in μrad.

Target diameter mm	Target size μrad	SSD μrad	Phase plate μrad	Beam (3ω) μrad	Phase plate beam ratio
3	429	50	375	50	7.5
2.5	358	50	304	42	7.3
2	286	50	233	33	7.0
1.5	215	50	162	25	6.5

Table 3-9. Beam size requirements scaled to 1053-nm diffraction limit (θ_{DL} = 6.02 μrad).

Target diameter mm	Target size	SSD	Phase plate	Beam (3ω)	Phase plate beam ratio
3	71	8.3	63	8.3	7.5
2.5	59	8.3	51	6.9	7.3
2	47	8.3	39	5.5	7.0
1.5	36	8.3	27	4.2	6.5

factor in RMS nonuniformity, and we are free to set a relatively lax limit on the ratio of beam divergence to phase plate divergence. Based on nonuniformity calculations, we require this ratio to be greater than about 6. If we set it at just over 6, we obtain the beam size requirements for various target diameters given in Table 3-8.

In Table 3-9, we reexpress these divergences in terms of the 1ω diffraction-limited divergence for a square 35-cm beam, namely $\theta_{DL} = 2\lambda/D = 6.02$ μrad.

The beam divergence requirement is set by the uniformity requirements for the larger, ignition targets, at about 35 μrad.

The beam profile on the capsule must be shaped to meet the uniformity requirements. For the hard sphere illumination model, we have calculated the nonuniformity for the optimum port locations and parametrized the pressure profile from any one beam as a power of cos(θ).

$$A(\theta)I(R_t\sin\theta) = I_0\cos^{\nu}\theta \qquad (33)$$

In Figure 3-18, we plot the RMS nonuniformity for the optimum port locations as a function of ν. There is a broad minimum in the nonuniformity at ν = 2.25. The minimum is approximately symmetric; its width for doubling the nonuniformity is about $1.5 < \nu < 3$.

The apparent beam profile on the target will change as the target implodes. We can account for this within the hard sphere model by scaling the beam profile inversely with the target radius. Clearly, we wish to maintain an attractive pressure profile during the implosion. If the beam profile is flat, the nonuniformity is independent of the target radius, otherwise the nonuniformity will change as the target implodes. The effect of decreasing radius therefore depends separately on the beam profile and absorption profile. However, the hard sphere model gives no prescription for separating the absorption profile from the beam profile. Nonetheless, a feel for the sensitivity is obtained by using a two parameter parametrization as follows. The beam profile is

$$I(r) = (1 - r^2 / R_{beam}^2)^{\nu} \tag{34}$$

and vanishes outside the beam radius R_{beam}. Laser light outside the target radius is not absorbed by the target so the beam capture efficiency is

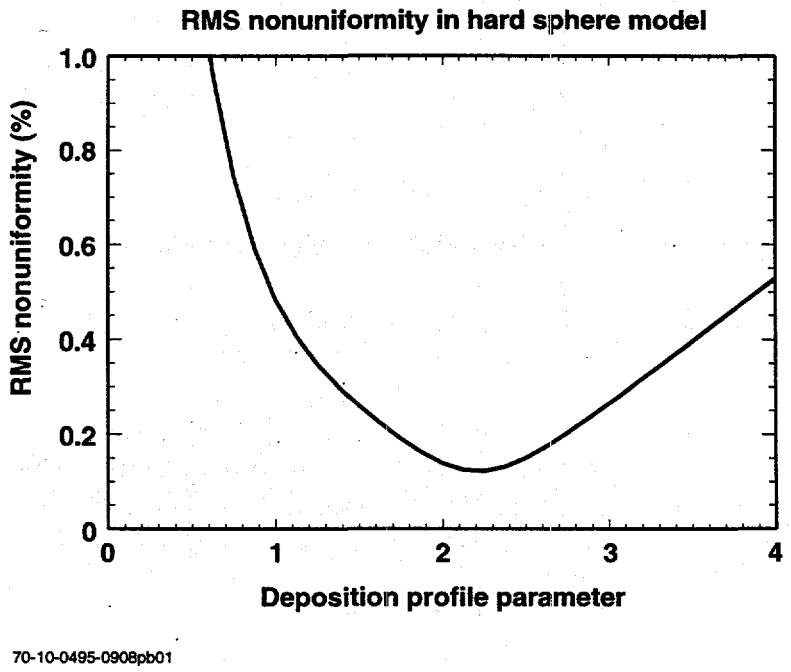

Figure 3-18. RMS nonuniformity as a function of the power law exponent of the intensity profile from one beam. The abscissa is ν where $I(r) = (1 - (r/R))^{\nu/2}$. There is a minimum at ν = 2.2. The nonuniformity is quite sensitive to deviations from this optimum profile.

$$\eta = \frac{\int_0^{R_t} I(r) 2\pi r dr}{\int_0^{R_{beam}} I(r) 2\pi r dr} \tag{35}$$

or

$$\eta = 1 - [1 - (R_t / R_{beam})^2]^{1+\nu} \tag{36}$$

Figure 3-19 plots the beam capture efficiency as a function of the ratio R_t / R_{beam}.

The absorption profile in this parametrization is set so that at tangential focus the deposition profile is optimal.

$$A(\theta) = \cos^{(2.125-\nu)}\theta \tag{37}$$

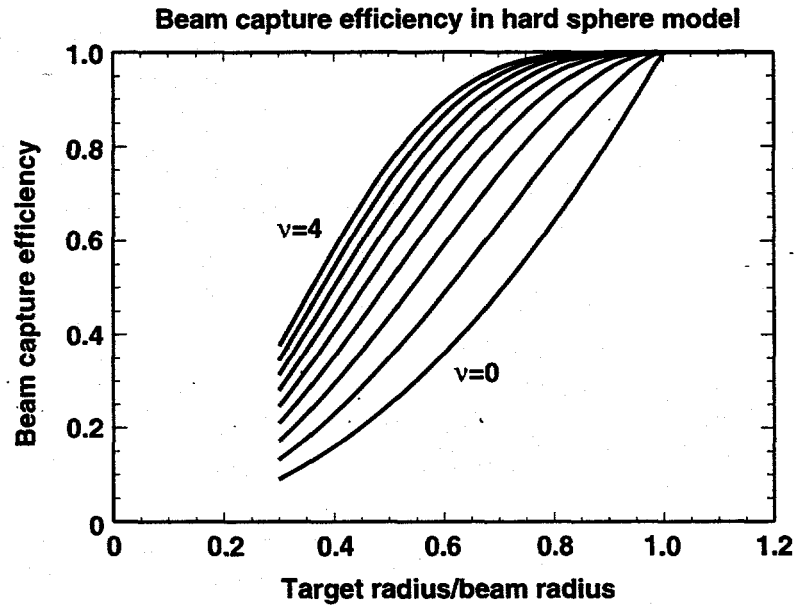

70-10-0495-0909pb01

Figure 3-19. The beam capture efficiency in the hard sphere model as the target radius decreases, parametrically in the beam profile parameter ν. The data are plots for ν = 0,0.5,...,4. They illustrate the advantage of higher ν for the absorption efficiency of the target as it implodes.

Figure 3-20 plots the nonuniformity as a function of the ratio of target radius to beam radius, for various beam profiles $\nu = 0.5, 1, 1.5, 2$, for this choice of absorption profile. As expected, the variation in nonuniformity with target radius is stronger for more sharply varying beam profiles. The variation of nonuniformity with target radius will be weaker if more of the angular variation in the deposition is taken up by the absorption profile. In Figs. 3-21 and 3-22, we plot the nonuniformity as a function of target radius for more strongly varying absorptions:

$$A(\theta) = \cos^{(2.625-\nu)}\theta, \ \cos^{(3.125-\nu)}\theta \tag{38}$$

These plots suggest that to maintain a low time-dependent nonuniformity, the beam profile must be quite flat, or at least that a quadratic profile may not keep the time-dependent nonuniformity within the target requirements.

To the extent that $A(\theta)$ represents the effect of the corona on pressure, the hard sphere model suggests that the time-dependent nonuniformity is quite sensitive to the evolving properties of the corona. We have tested this by calculating the actual three-dimensional deposition profile in the corona including refraction and inverse bremsstrahlung absorption. The pressure responds very rapidly to changes in the deposition. We therefore used a static model of transport to relate the pressure to the deposition. The general effect of the corona on absorption can be illustrated using analytic results from a representative simple model of the corona.

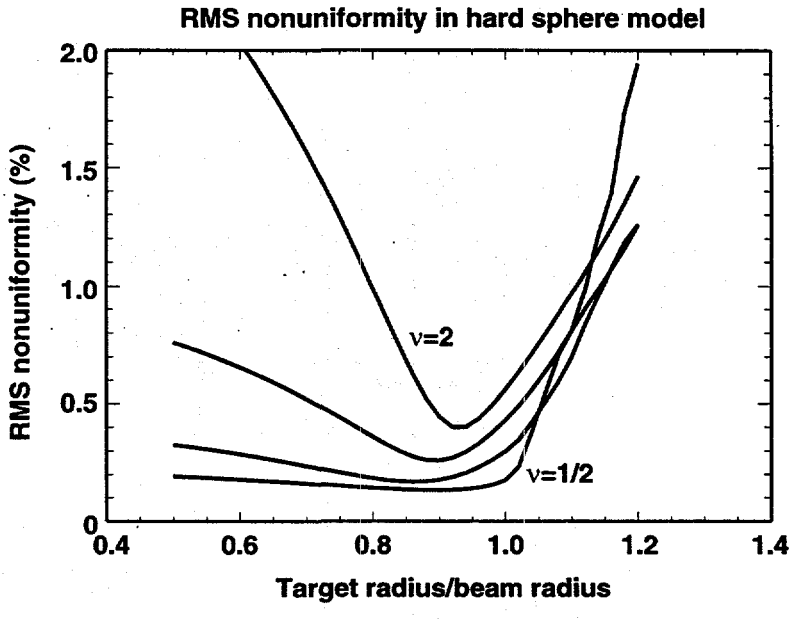

Figure 3-20. The RMS nonuniformity in the hard sphere model assuming a beam profile parameter $\nu = 0.5,1,1.5,2$, and an absorption profile $A = (\cos\theta)^{\mu}$ where $\mu + \nu = 2.125$.

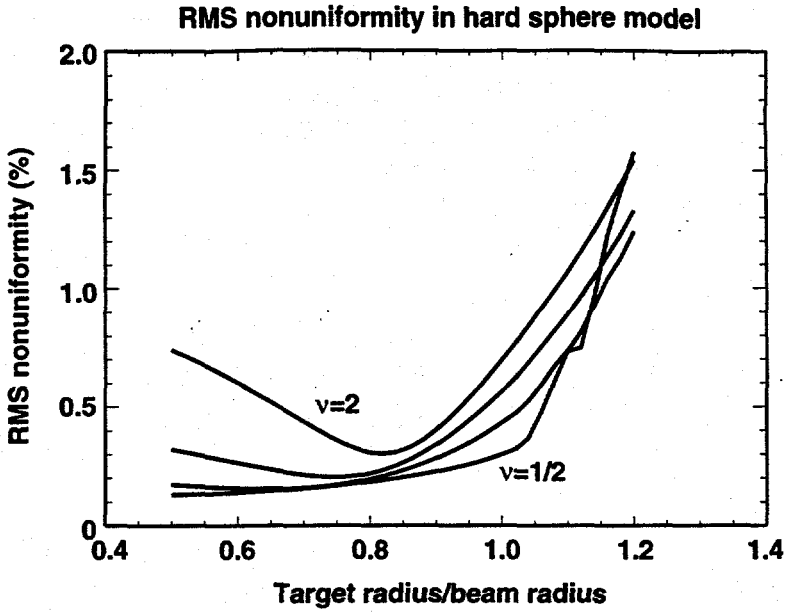

Figure 3-21. Repeat of Fig. 3-20, but where $\mu + \nu = 2.625$.

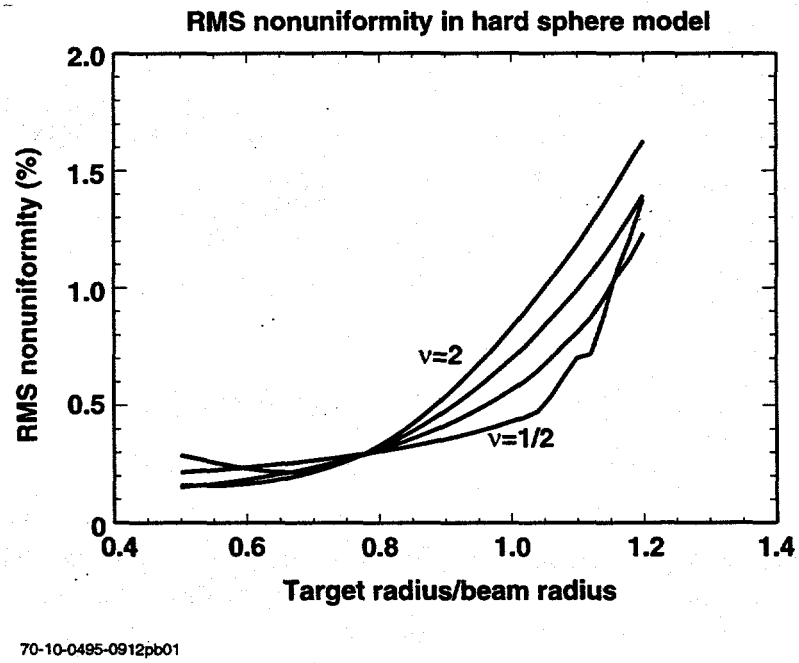

Figure 3-22. Repeat of Fig. 3-20, but where $\mu + \nu = 3.125$.

Consider a constant velocity spherically expanding corona. While this is not a bad approximation, in general, it is not a sufficiently good approximation for a quantitative evaluation of the coronal optics. Nonetheless, it is qualitatively useful because refraction and absorption in this corona can be solved analytically. The density profile is given by $dm/dt = 4\pi nvr^2 = \text{constant}$, so

$$n / n_c = (L / r)^2 \tag{39}$$

where r = L is the critical surface. The refractive index is $[1-(L/r)^2]^{1/2}$. Then with $u = 1/r$, the ray trajectories are given by

$$du / d\theta = \left[\frac{1 - L^2u^2}{b^2} - u^2\right]^{1/2} \tag{40}$$

where b is the impact parameter of the ray (Fig. 3-23). The trajectories are

$$u = \frac{1}{b\xi}\sin\xi\theta$$

where

$$\xi = [1 + (L / b)^2]^{1/2}. \tag{41}$$

For any impact parameter greater than zero, the ray fails to reach the critical surface. The distance of closest approach for a given ray is

$$r_{\min} = (L^2 + b^2)^{1/2} \tag{42}$$

and occurs at half the deflection angle.

$$\theta = \pi / 2\xi \tag{43}$$

The locus of the distance of closest approach of any ray at a given angle is the caustic of the "lens" formed by the corona. It is plotted on Fig. 3-23. The strongest deposition occurs along the caustic because the density is greatest there, and every ray osculates the caustic. The caustic therefore represents to a reasonable approximation the primary region of energy deposition in the corona from a single beam. For rays near the center of the beam, the caustic is approximately given by the locus of the turning points of the rays, $r = L / [1+(2\theta/\pi)^2]^{1/2}$.

A significant feature of the coronal deposition that is not present in the hard sphere model is the existence of pressure in the geometrical shadow of the target. The rays that

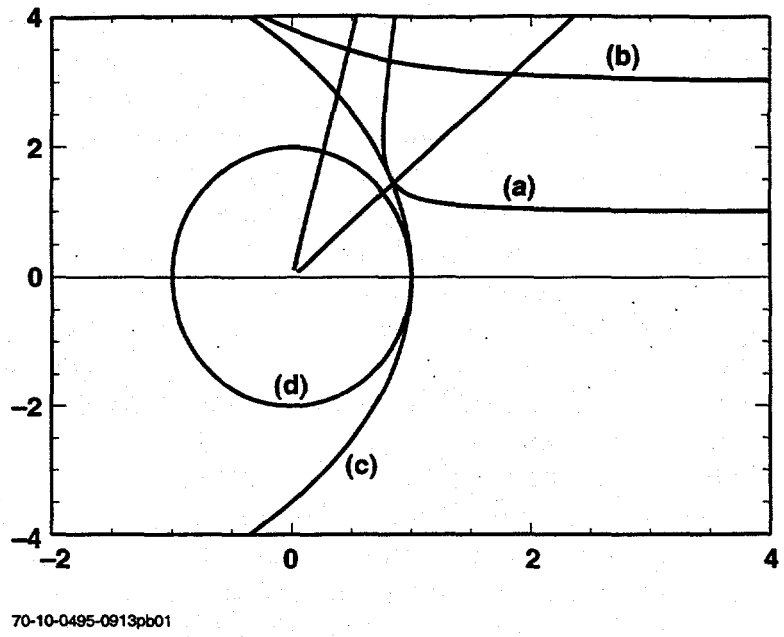

Figure 3-23. Ray trajectories in the corona: (a) near axial ray approaches critical surface and is reflected, (b) peripheral ray is weakly deflected, passes through low-density plasma, (c) the caustic, the locus of the distance of closest approach of any ray at the given angle, (d), the critical surface.

pass by the target and enter the region $\theta > \pi/2$ deposit energy that contributes to the pressure on the dark side of the target, in the geometrical shadow of the hard sphere model. The pressure of these grazing rays extends and smoothes the pressure profile generated by a single beam, and can help reduce the nonuniformity below the levels predicted by the hard sphere model.

The plasma density and temperature profiles were obtained from 1-D LASNEX calculations of the target. The deposition profile was calculated, and the resulting pressure profile was taken to be

$$p(r,\Omega) \approx \int_{r_{solid}}^{\infty} W(r,\Omega) r^2 dr F(r) \qquad (44)$$

where F(r) is a weighting function that simulates transport. We used three models for F(r) to determine the sensitivity of our results to the transport physics. The models were F(r) = constant, F(r) = exp(-r/a), where a is the distance between solid density and 0.1 critical density, and also F(r) = 1 for $r < r_{peak}$ and 0 otherwise, where r_{peak} is the radius at which the corona temperature peaks. The smoothest pressure profiles are obtained for F(r) = constant. The least smooth are obtained in the temperature cut-off model where there is a hard edge to the pressure profile that occurs when the caustic moves outside r_{peak}.

Plasma refraction causes the power in a given ray bundle to be deposited over a range of angles, so that the relation between deposition and beam profile is nonlocal. The pressure at a given angle receives contributions from rays from a fairly large fraction of the beam profile. This smoothing tends to make the pressure profile somewhat insensitive to the beam profile, so that at later times the nonuniformity for a flat beam profile is very similar to the nonuniformity from a quadratic ($\cos^2\theta$) or sinc^2 $(\sin x/x)^2$ profile. At all times in the pulse but the earliest, the nonuniformity was about 0.2% to 0.4% for beams that were flat or quadratic. On the other hand, at the earliest time when the corona is forming, the relation between deposition and beam profile is more local in character, and tends to show some sensitivity to the beam profile. Figure 3-24 shows the power deposition profile at t = 17 ns and Fig. 3-25 shows the pressure profile arising from this deposition in the three models considered. The near quadratic form for the pressure indicates that the nonuniformity from all 48 beams will be low. In Fig. 3-26, the nonuniformity is plotted as a function of time in the pulse for flat and sinc^2 beam profiles, for the most optimistic (F(r) = const) and the least optimistic (temperature cut-off) models of the pressure. Each beam is assumed initially at tangential focus. The general decline in nonuniformity with the size of the corona is evident. At early times, where the plasma density is steep the ray approximation may not be accurate, depending on the details of the plasma profile. It is therefore preferable to use a hard sphere model for the initial nonuniformity. Figure 3-27 illustrates that the absorption efficiency is lower for flat profiles.

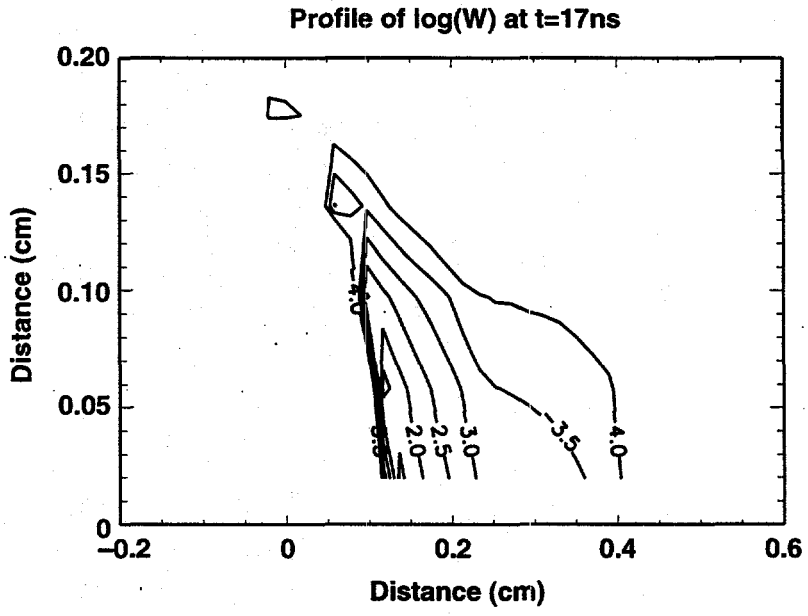

Figure 3-24. Power deposition profile at t = 17 ns for the LLE target with a picket fence pulse and a flat beam profile. Note the concentration of energy along the caustic.

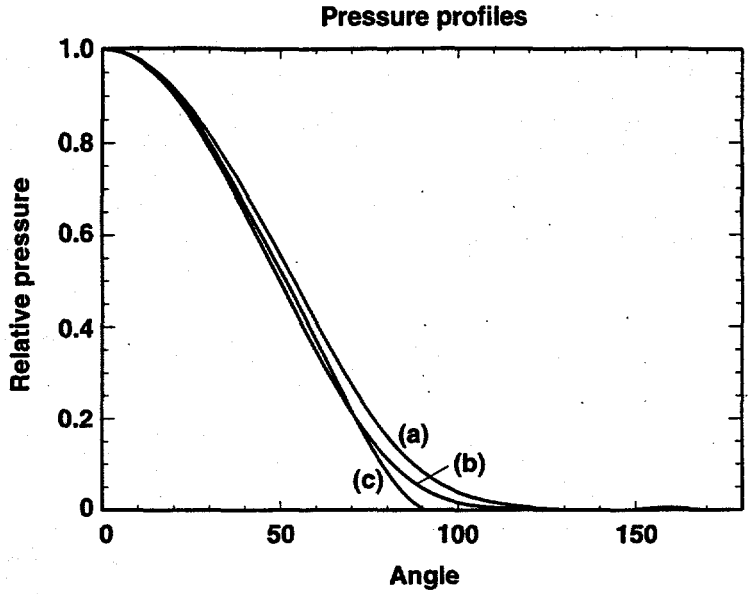

Figure 3-25. The pressure profile drive by the deposition profile in Fig. 3-24. The three models are described in the text. They are (a) F=const, (b) F=exp(-r/a), (c) F cut-off at temperature peak. All three models give a near-optimal pressure profile for minimizing the nonuniformity. Flat beam profile.

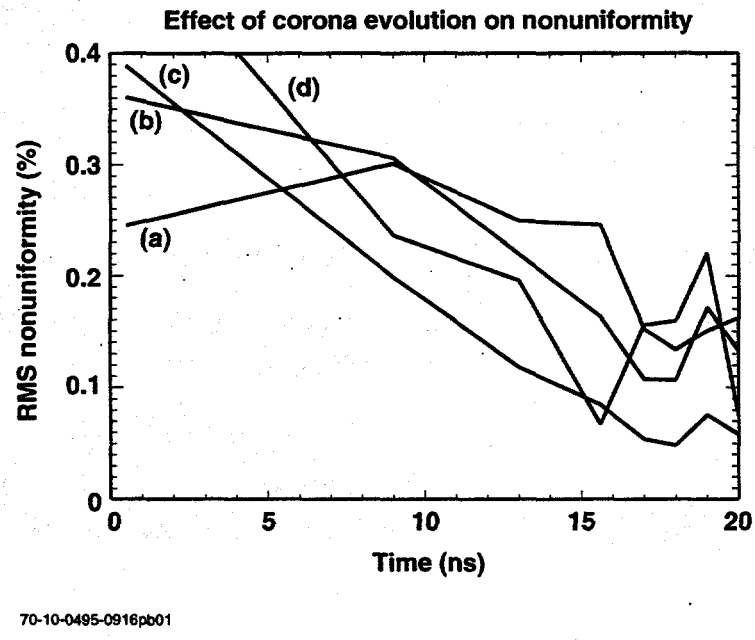

Figure 3-26. RMS nonuniformity for various beam profiles and pressure models. (a) optimum beam profile (ν = 2.125), pressure model F = const, (b) flat beam profile, F = const (c) optimum beam profile, F = temperature cut-off (d) flat beam profile, F = temperature cut-off. The early time results have large error bars arising from the initial steepness of the corona density profile.

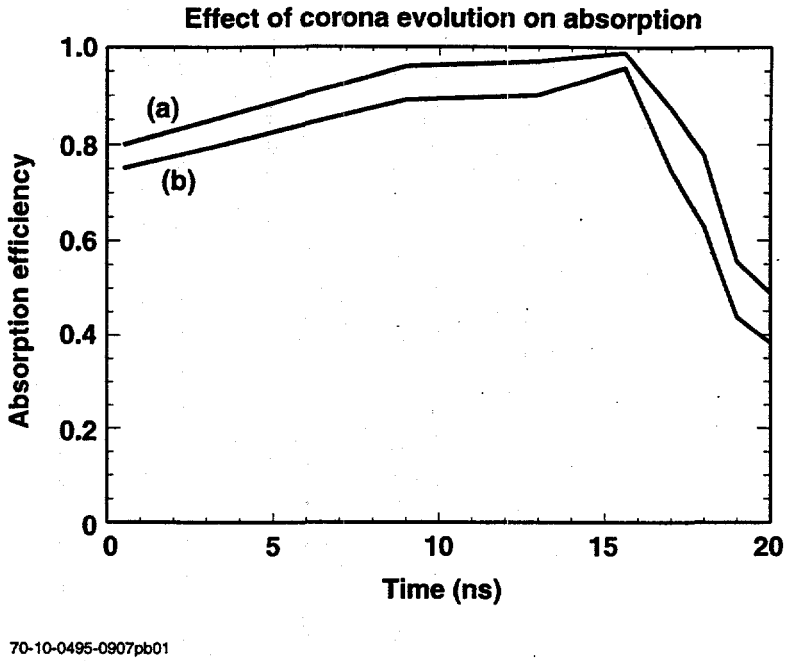

Figure 3-27. Coronal absorption for (a) optimum beam profile, (b) flat beam profile.

We conclude that the nonuniformity at later times in the pulse is controlled by coronal refraction, and is less sensitive to the beam profile. At early times, we prefer that the beam profile vary as $(\cos\theta)^{1.2}$ to give the optimal pressure profile $(\cos\theta)^{2.2}$. This suggests that the target smoothness requirements can be met if the beam profile is chosen to make the initial pressure profile uniform, relying on the coronal physics to smooth the pressure profile at later times.

3.4 High L-mode Uniformity

Direct-drive targets place a requirement on the high L-mode uniformity of the laser. The intensity is written as a sum over spherical harmonics.

$$I(\Omega) = \Sigma I_{LM} Y_{LM}(\Omega) \tag{45}$$

We define a local fluence as the time-integrated intensity over a finite time interval.

$$\begin{aligned} F(t,\Omega) &= \frac{1}{\tau}\int_{t-\tau/2}^{t+\tau/2} dt'\, I(t',\Omega) \\ &= F_0(t)[1+\sum_{L>0}\sigma_{LM}(t)Y_{LM}(\Omega)] \end{aligned} \tag{46}$$

The time interval for the integral is typically $\tau = 1$ ns. The target requirement on the high L-modes is

$$\left(\frac{1}{4\pi}\sum_{L=21}^{L=500}\sigma_{LM}{}^{2}(t)\right)^{1/2} < \sigma_{\max} \qquad (47)$$

where $\sigma_{max} = 0.01$. The various methods for achieving this goal[6–14] involve illuminating the target with a beam that is a rapidly fluctuating speckle pattern, such that the time-integrated intensity reduces to a smooth envelope. Since the normalized variance of a speckle pattern is 1.0, and the speckle field obeys Gaussian statistics, the normalized variance (including all L-modes) for the sum of N distinct patterns is $(1/N)^{1/2}$. To reach a normalized variance of 0.01 (all modes) 10^4 patterns must be applied to the capsule within the integration time of 1 ns. Fewer than 10^4 patterns will actually be required to satisfy the target requirements because the target requirement involves only modes 21–500. In this section we describe techniques that will accomplish this.

Regardless of the implementation, the target requirements place a fundamental limitation on the smoothing rate and the added beam divergence. For a single beam of full bandwidth $\Delta\nu$, the maximum number of distinct speckle patterns which can be generated in a time τ is $N_{max} = \Delta\nu\tau$, and thus $\sigma > 1 / (\Delta\nu\tau)^{1/2}$. It is therefore of paramount importance to maximize the bandwidth in order to achieve the optimal smoothing rate. This bandwidth limit is shown for a single beam in Fig. 3-28. To achieve this smoothness, there must be $\Delta\nu\tau$ distinct speckle patterns available in the laser beam. The presence of these patterns gives rise to an added beam divergence that is necessary for smoothing. (With no added divergence there is only one speckle pattern in the laser.) The angular shift required for a speckle pattern to decorrelate is λ/D where λ is the wavelength on target and D is the beam aperture at the target focus lens. For smoothing by spectral dispersion in two dimensions (and perhaps other methods as well) this

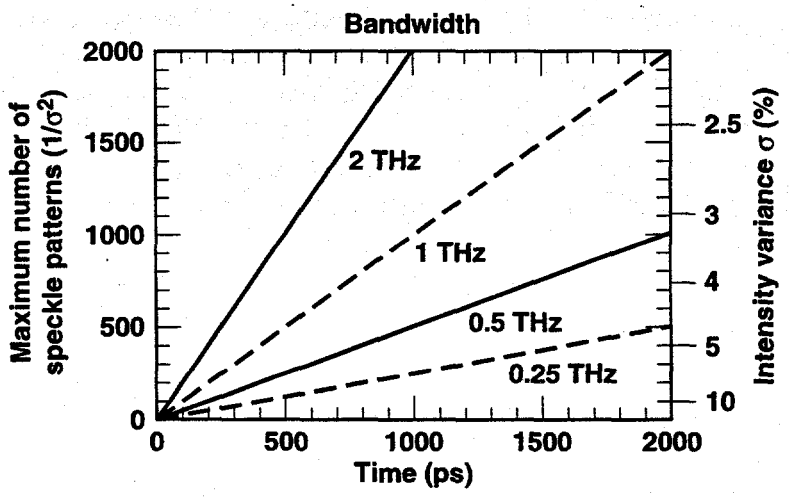

70-10-0495-0868 pb01

Figure 3-28. Maximum number of speckle patterns in a beam of given bandwidth.

implies that $N_{max} = \Delta\nu\tau = (\Delta\theta\, D/\lambda)^2$ where $\Delta\theta$ is the added divergence of the laser, and D is the square beam width. For the NIF, $\lambda/D = 1.0$ μrad, thus one finds that the proposed 50 μrad induced divergence is sufficient to generate $50^2 = 2500$ speckle patterns (or $\sigma = 2\%$). As can be seen from Fig. 3-28, the bandwidth limit is more severe than this divergence limit for integration times up to 2 ns and perhaps longer.

To achieve the desired total uniformity on target, one must also consider the effects of multiple beam and polarization overlap. In the NIF baseline, each of 48 clusters will comprise 4 beams of nonoverlapping frequency (each separated by 0.5–1 THz). In this case, these 4 beams smooth in a few picoseconds leading to a $\sqrt{4} = 2$ times improvement in σ. Of the 48 clusters, calculations show that the effective number illuminating a single point is about 13. The overlap of these beams smoothes the spatial frequencies present in a single beam, but also, owing to coherent interference, generates new nonuniformity at very high spatial frequencies (L-modes > 10^4). It is generally assumed that these very high spatial frequencies have no significant adverse effects on target performance and can therefore be neglected. Finally, by generating a distinct speckle pattern in each of the two polarizations one attains an effective total increase of ~2 (polarizations) × 13 (effective number of clusters) × 4 (beams / cluster) = 104 times in the number of speckle patterns generated by one beam. Therefore the total variance in intensity is reduced from the single beam variance by a factor of ~10. With this overlap smoothing taken into account, one can see from Fig. 3-28 that an estimated single beam bandwidth of 500 GHz will ideally (i.e., for a smoothing method which achieves the bandwidth limit) lead to a total variance of 1% in an integration time of 200 ps, and 0.45% at 1 ns. Thus one sees that the uniformity requirements of the direct-drive target can be exceeded by two times or more for parameters which are consistent with the NIF design.

3.4.1 Beam Smoothing Methods

The baseline method for beam smoothing on NIF is two-dimensional smoothing by spectral dispersion (2-D SSD). In the SSD method, the speckle pattern and average illumination profile are generated by a tailored random phase plate. The laser is then phase modulated and angularly dispersed to create a time varying (shifted in one perspective) speckle pattern which averages out to leave the smooth beam profile (Fig. 3-29). To accomplish 2-D SSD, the laser is phase modulated, dispersed by a grating in one transverse dimension, followed by a second modulation, and dispersion in the orthogonal transverse dimension. The effect of the gratings is to produce a temporal skew across the beam. In the Littrow configuration at an angle of incidence θ, one finds that the skew s (ps/cm) is given by

$$s = 2\tan\theta / c = \lambda / dc\cos\theta \tag{48}$$

where d is the groove spacing. The angular dispersion is thus proportional to the skew

$$d\theta / d\lambda = 1/d \;\cos\theta = sc/\lambda \;\; and \;\; d\theta / d\nu = -s\lambda \cdot \tag{49}$$

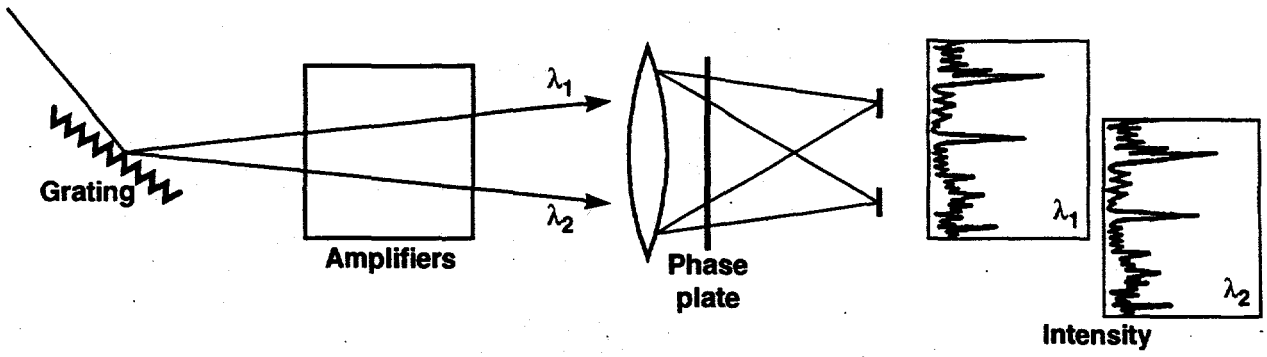

Figure 3-29. Beam smoothing by spectral dispersion (SSD). Spectral components are angularly dispersed by a grating which results in a shifted speckle pattern after transmission through a phase plate. Integrating these shifted patterns average out the high spatial frequencies present in the individual speckle patterns.

For optimal smoothing the dispersion of each grating must be adequate to separate adjacent sidebands (in the case of FM, the sidebands are separated by the modulation frequency Ω_{mod}) by the minimum angular shift for decorrelation, $\lambda/D, \leq d\theta/dv\ \Omega_{mod}$. In terms of temporal skew induced by the grating, the skew must be at least equal to the period of the modulator, $sD > 1/\ \Omega_{mod}$. For each grating an oppositely dispersive grating preceding the modulator can eliminate the generated temporal skew on the pulse (Fig. 3-30).[11] The great advantage of this method is that the near field quality of the beam intensity can be maintained by relaying the plane in which the gratings lie to the amplifiers.

The smoothing performance of this method has been calculated, and it shows that near bandwidth limited performance can be attained for integration times of 1–2 ns (Fig. 3-31). SSD has the disadvantage that spatial frequencies of wavelength longer than the beam motion on target (focal length times total divergence. $L \tilde{<} 20$) are not smoothed effectively. However, these spatial frequencies have relatively little total nonuniformity (less than 0.25%) and are outside of the band of peak RT growth (wavelengths of 50–200 μm), and therefore one expects 2-D SSD will yield good target performance results. However, given the target uncertainties it would be advisable to maintain the capability to implement other smoothing techniques that offer better performance at these low spatial frequencies.

3.4.2 Propagation of Partially Coherent Light (PCL) Pulses

In this method a partially coherent (i.e., spatially incoherent) beam is generated in the front end and propagated through the laser amplifiers. This approach has been investigated on the Phebus laser,[8] where the spatial incoherence is generated by propagation of a temporally incoherent pulse though a long multimode fiber. In this method it is expected that instead of a shifting speckle pattern, one generates completely uncorrelated patterns at the bandwidth limited rate. Although one expects that there is a divergence limit for the asymptotic smoothing level in this method as well; this ques-

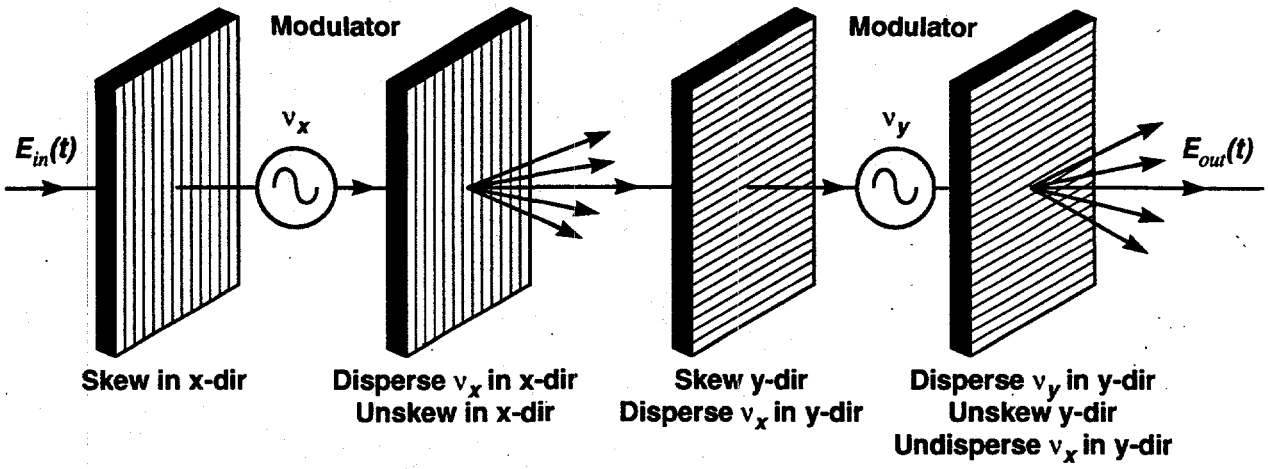

$$E_{out}(t) = E_{in}(t)\exp[i\beta_x \sin(2\pi\nu_x(t + s_x x)) + i\beta_y \sin(2\pi\nu_y(t + s_y y))]$$

70-10-0495-0870 pb01

Figure 3-30. Schematic of a 2-D SSD modulation scheme, suitable for direct-drive experiments on NIF.

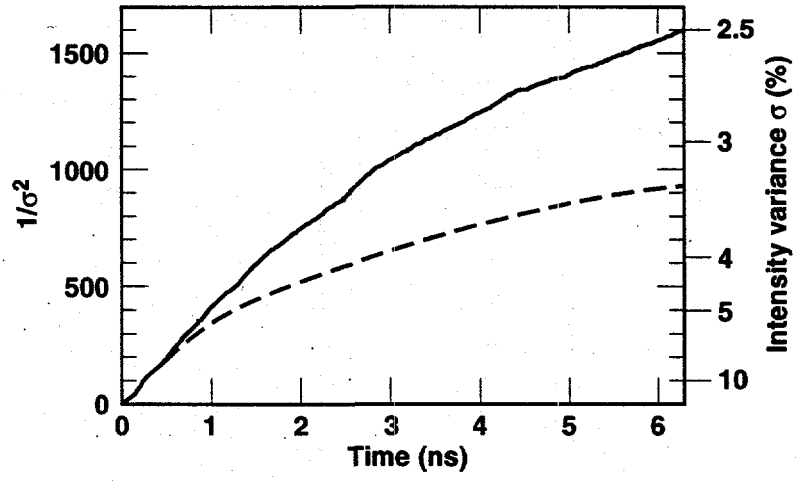

70-10-0495-0871 pb01

Figure 3-31. Variation of $1/\sigma^2$ with time in the case of standard 2-D SSD using 8.2 and 3.4 GHz modulation frequencies along transverse orthogonal directions, aggregate bandwidth of 500 GHz, and induced divergence 25 times the diffraction limit (dash). Solid curve: a second modulation frequency is applied in each direction (~0.3 GHz), and the beam divergence and bandwidth are unaltered.

tion has yet to be fully resolved. However, because the speckle patterns are uncorrelated one expects that all spatial frequencies are smoothed equally. As a result, one can analytically determine the nonuniformity as a function of spatial frequency in terms of the dependence found for a single speckle pattern. For a square aperture of width D, the total normalized variance for a single speckle pattern within the band of spatial frequencies (f_1,f_2) is given by

$$\sigma^2{}_{total}(f_1,f_2)=\int_{f_1}^{f_2}\sigma^2 df=(\pi f^2-8f^3/3+f^4/2)\Big|_{f_1}^{f_2} \qquad (50)$$

where the spatial frequencies have been normalized to the maximum frequency D/Fλ (for NIF this spatial frequency corresponds to a wavelength of 7 μm), and F is the final lens focal length. If one can attain ideal uniform bandwidth filling, then in an integration time t, this result is reduced by Δν t, independent of spatial frequency. This result can be compared to numerical calculations of 2-D SSD to show the improved performance at low spatial frequency (Fig. 3-32). The disadvantage of this method is that the near field beam has large fluctuations in intensity. As a result, one expects diminished peak laser performance. Experiments on Phebus have shown that the laser power output is limited by these fluctuations to about one half of what is obtained from a similar laser system operated with a clean near field.

The critical stage of imprinting the target with laser nonuniformity occurs during the driver pulse foot, where typically the fundamental intensity is less than 10% of the peak. It is thus desirable to obtain maximum smoothing rate during this stage of the pulse. To this end one can capitalize on the fact that conversion efficiency is not critical during the foot, and push the modulation bandwidth far beyond what would be acceptable at the pulse peak. Calculations by J. Auerbach[15] (see Fig. 3-42) indicate that a FM bandwidth of 300 GHz at 1ω (i.e., 0.9 THz at 3ω) would lead to a penalty in the energy available to the pulse peak of only 2%. Near the end of the foot one would then require the capability to quickly reduce the modulation bandwidth so as not to drastically reduce the conversion efficiency at the pulse peak.

In a similar fashion one could conceive of switching entirely between smoothing methods from the foot to the pulse peak. Given the above discussion of PCL and its potential advantages over SSD, one might want to use PCL during the pulse foot and SSD (1-D or 2-D if any method) during the pulse peak. Here again, because the foot intensity is low, the difficulties of propagating PCL though the amplifiers may be eliminated, and superior performance at low spatial frequencies is obtained. However, in order to achieve laser full output at the pulse peak, the PCL light must be replaced by a near field intensity profile of good quality before the pulse peak. Figure 3-39 is a schematic for a possible implementation of this technique.

As a final possibility, one might consider having the pulse foot in a physically separated beam (e.g., one of the four beams in a cluster). If this is the case one could imagine using 2ω as the beam color for the foot only, thereby allowing for much broader spectral

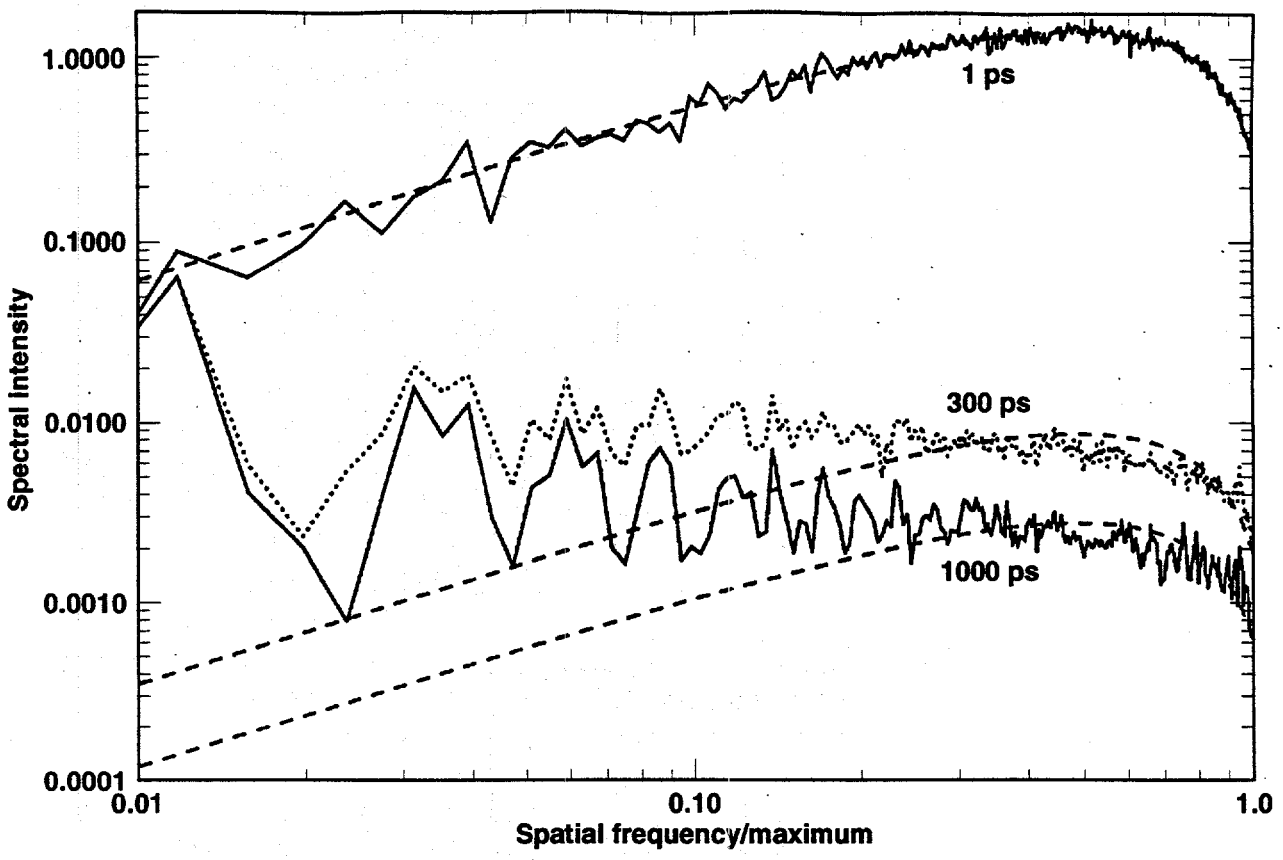

70-10-0494-0872 pb01

Figure 3-32. Calculated variance power spectrum of the integrated speckle intensity vs spatial frequency produced by 2-D SSD (solid and dotted curves) compared at the indicated integration times. 2-D SSD calculation assumes 8.2 and 3.4 GHz modulation frequencies and aggregate bandwidth of 500 GHz. PCL is assumed to also have a bandwidth of 500 GHz. Normalization of all curves is such that the area under any given curve $\int_{f_1}^{f_2}$ [spectral intensity]df yields the value of σ^2 for a given spatial frequency range. The spatial frequencies are normalized to $D/\lambda F$ which for a 1.5 mm radius target corresponds to L = 1350.

extent. Alternatively one could use Raman scattering in this "foot" beam to generate broad bandwidth for use in a smoothing scheme.

3.4.3 NIF Baseline: 2-D SSD

The current baseline beam smoothing proposal for NIF direct drive is to use 2-D SSD utilizing the integrated optic modulator as the first phase modulator, and a free standing resonant cavity modulator as the second (Fig. 3-33). Because the integrated

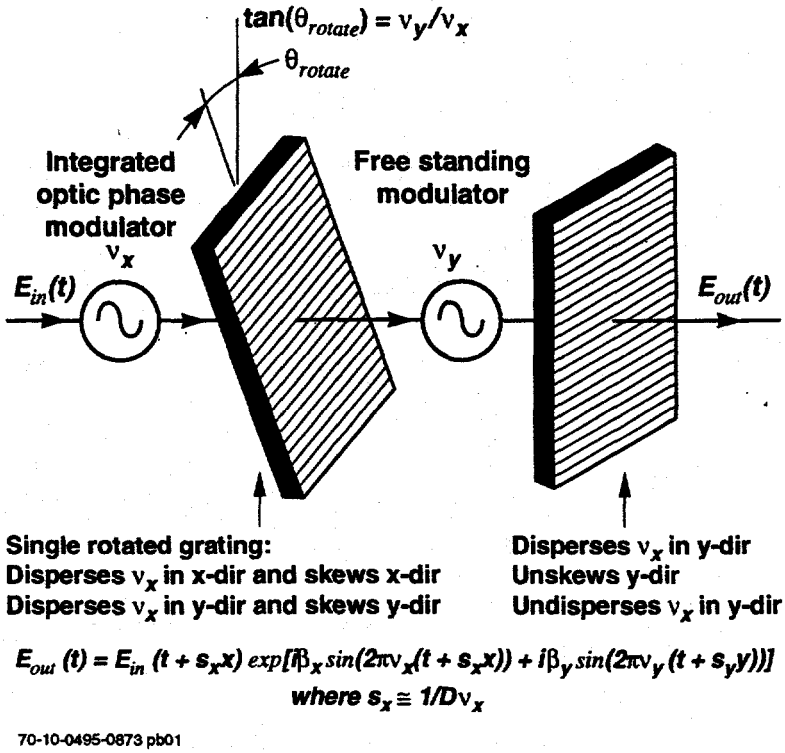

Figure 3-33. Modified 2-D SSD arrangement reduces the number of optical components.

modulator is a single transverse mode device, a grating placed before it cannot be used to compensate for the temporal skew generated by the grating following it. In the pre-amplifier section, between the four-pass rod amplifier and the beam shaping optics, one must insert the free standing LiNbO3 modulator and two gratings. The first grating is rotated about the optical axis so that it both disperses the bandwidth of the integrated modulator and pre-compensates for the dispersion of the second grating. The proposed total bandwidth at 1ω is 150 GHz and the induced full angular divergence is 50 μrad, although it may be possible to increase these significantly during the pulse foot.

The gratings must be placed in relay planes and it is desirable for the modulator to be located at a relay plane as well. Out of the relay planes FM is converted by free propagation into AM. For the usual case where the grating skew equals the modulation period this conversion is given by

$$A = Kz\beta/D^2 \tag{51}$$

where A is the peak-to-peak modulation in percent, K is 1/7.5 cm, z is the propagation distance, β is the modulation depth, and D is the beam width. For β = 7, at full NIF aperture this AM is only 1% for every 13 m of propagation away from the relay plane.

In the rod amplifier, however, D = 2.5 cm and the AM is 1% for every 6.7 cm of propagation. It is therefore important, if there is significant nonlinearity present in the rod amplifier, to minimize the separation of the rod from the relay plane.

The schematic of the current proposal for the arrangement of the gratings and modulator is shown in Fig. 3-34. A second LiNbO3 crystal oriented with its c-axis rotated by 90° provides compensation for astigmatism created by propagation through the modulator. If desired this crystal could, in fact, be used as a second free standing modulator. It should be noted that the telescope reducing the beam size to pass through the small aperture of the modulator may require large demagnification (10:1) and therefore will have significant space requirements.

The integrated phase modulator will be required to generate as much as 200 GHz of bandwidth, and will need to have frequency response extending to 10 GHz. The driving electronics should be capable of generating arbitrary wave forms in the 3–10-GHz range, including being capable of greatly reducing the modulated bandwidth on a ~100-ps time scale. One must insure that group velocity dispersion present in the transport fiber does not convert this FM to AM to the extent where laser performance is adversely affected; i.e., either the length of the fiber after the modulator must be made

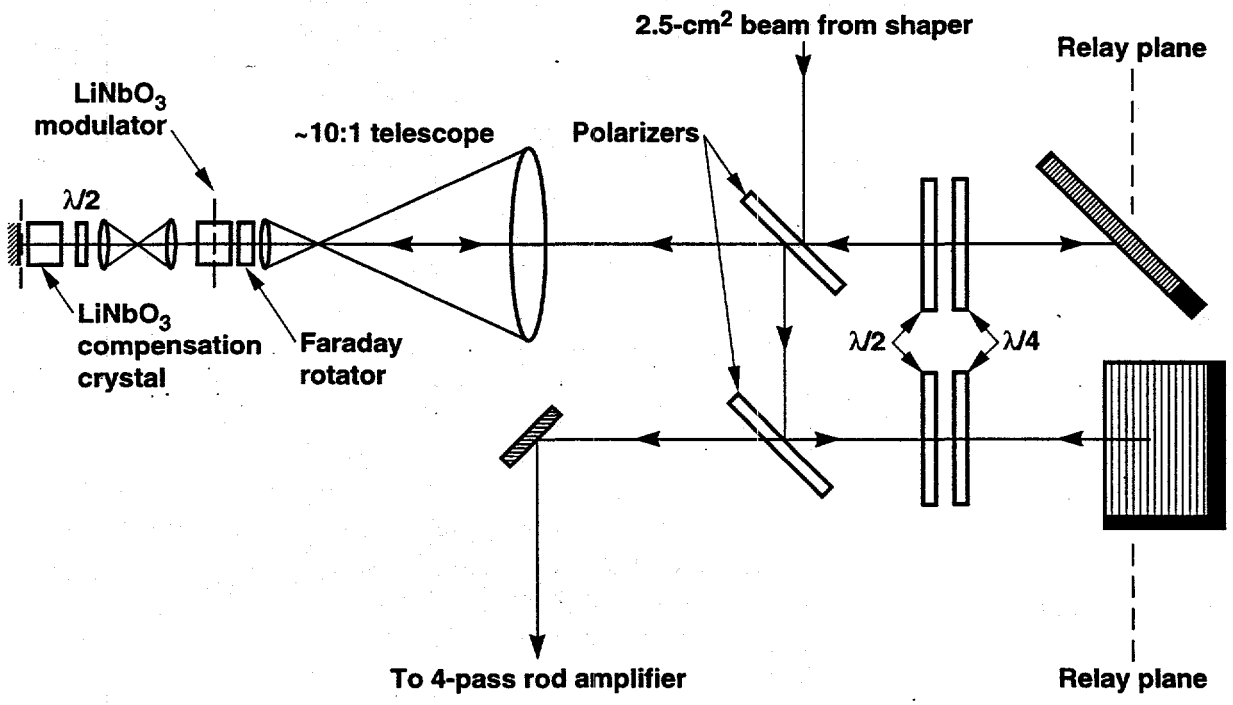

Figure 3-34. Schematic of 2-D-SSD generating hardware recently proposed for testing on the Beamlet. Adroit use of polarizers and rotators minimizes the number of expensive components.

sufficiently short and/or the dispersion of the fiber must be reduced. The peak-to-peak AM resulting from linear dispersion of FM light is given by

$$A = K'z\beta d^2/dw^2\Omega_{mod}^2 \quad (52)$$

where $K' = 8 \times 10^{-5}$, Ω_{mod} is the modulation frequency, and $d^2k/d\omega^2$ is the group velocity dispersion. For fused silica at the fundamental wavelength the dispersion is 1.5×10^{-4} ps^2/cm, and taking $\beta = 7$, $z = 100$ m, and $\Omega_{mod} = 10$ GHz yields a modulation of 8.4%.

If the AM is excessive, it would be possible to use a free standing modulator as the first modulator instead of the integrated modulator. This scenario would most likely be a more costly option, would not allow for arbitrary phase wave forms, and it would be more difficult to switch off the modulation before the pulse peak, however it would allow for the elimination of the temporal skew associated with dispersion of its bandwidth, if deemed necessary.

The free standing second modulator must provide modulation depth on the order of 10 and probably will operate in the 1 to 3 GHz range. It may be desirable to place a second free standing modulator in series with this one, operating at a different frequency. This would result in better spectral uniformity and smoothing. Also the interference (at the beat frequency) between the two modulators can be used in order to reduce the bandwidth and induced divergence during the pulse peak.[11] As another alternative to switching off the second modulator it may be possible to generate a plasma (optically or electrically) inside the modulator cavity which would rapidly damp the cavity field.

3.4.4 Polarization Overlap

If one can generate distinct speckle patterns on the target in orthogonal polarizations one obtains a smoothing improvement of about $\sqrt{2}$. A variety of arrangements for creating the two polarized patterns are possible. Perhaps the simplest is the use of a wedged birefringent plate (see Fig. 3-35). The optical field is polarized at 45° to the e and o axes of the plate which then generates two speckle patterns shifted from each other by an angle equal to $\Delta n \bullet \alpha$, where Δn is the birefringences and α is the wedge angle. In an arrangement discussed below, to create new speckle patterns one must shift by more than the maximum shift of SSD (~50 μrad). For KDP, this would require α = 0.1°, but if one uses a thicker wedge, e.g., $\alpha = 5°$, then the required birefringence would only be 5×10^{-4}. A number of other possibilities exist. One can double the grating dispersion (which has obvious disadvantages for the laser performance) and use the wedge to interlace orthogonally polarized modes separated by the minimum shift λ/D = 1.0 μrad. For this shift a 5° wedge would require a birefringence of only 10^{-5}, which may be induced by stress in an isotropic material. Another alternative method of creating an orthogonally polarized speckle pattern is to scramble the polarization over the near field aperture using diffractive optics or other patterned birefringent elements.

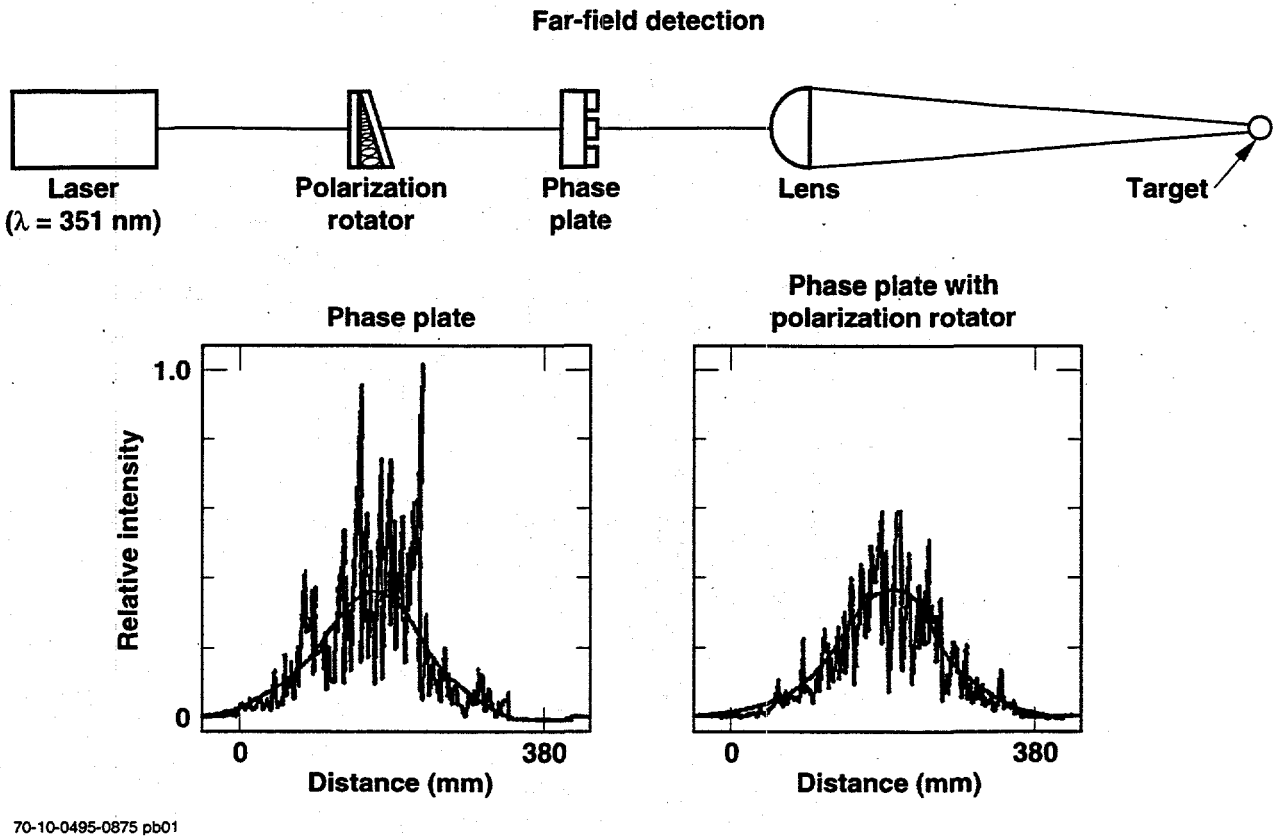

Figure 3-35. Polarization dispersion uses polarization to add modes to the far field, reducing the required added beam divergence for smoothing.

One strategy[16] for combining two-dimensional spectral dispersion of the bandwidth with polarization dispersion from a birefringent wedge is shown in Fig. 3-36. This shows the modal positions in the target plane. The minimum separation between modes should not be closer than ~1/2 the diffraction limit of the beam (i.e., 1/2 a speckle size) for good smoothing. The symbols "x" and "o" represent orthogonal components of polarization. This configuration allows for the smallest amount of angular dispersion through the laser, but requires the maximum polarization dispersion. To keep the beam nearly circular, either twice as many modes must be used in the direction perpendicular to polarization dispersion (i.e., twice the angular spread), or else the beam envelope must be adjusted using the phase plate to compensate for unequal angular dispersion.

To examine the effect of increasing the angular dispersion in one direction, we considered the following example: The parameters associated with the 3-GHz modulator (Fig. 3-35) were kept constant, and parameters of the other modulator were varied. The 1-Å IR bandwidth from the 3-GHz modulator produces about 31 spectral lines upon frequency tripling. These were spectrally dispersed to a separation of 1/2 a speckle distance in the target plane i.e., a total angular spread of 15 times the beam's diffraction limit (denoted by 15 x DL). This was chosen to be the direction of polarization dispersion, which was also 15 x DL, corresponding to the horizontal direction in Fig. 3-36. The total angular deflection in this direction is now 30 x DL.

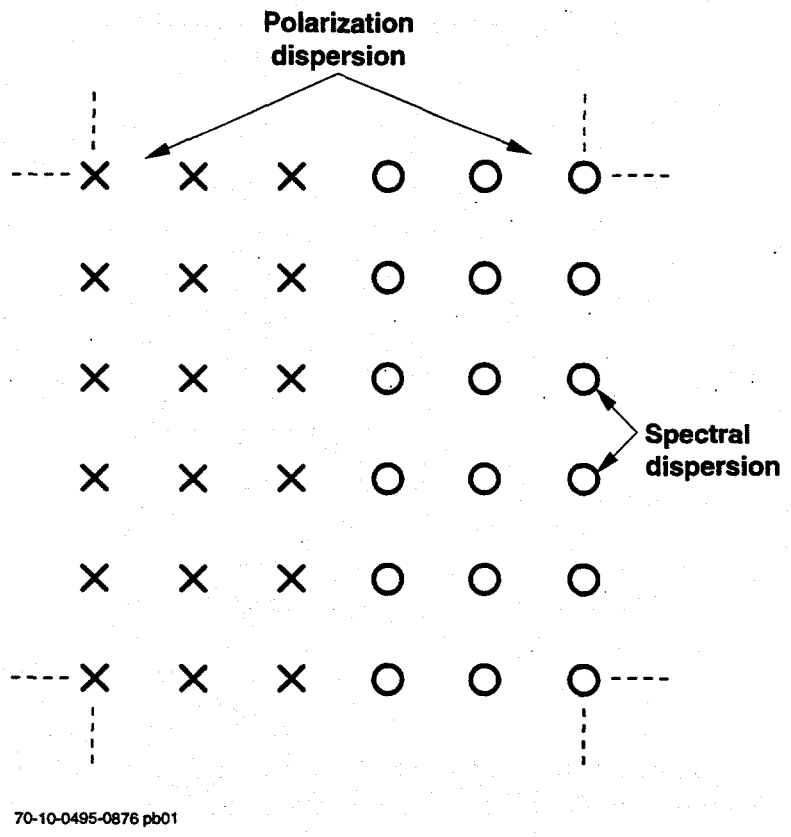

Figure 3-36. Far field of a polarization dispersed 2-D SSD beam. The polarization dispersion in this case is large compared to the added beam divergence.

For spectral lines from the second modulator, the modes were also dispersed to a separation of (1/2) DL in the target plane, but the number of modes (i.e., the total angular spread) was allowed to vary keeping the bandwidth constant. The bandwidth was maintained at a value near 4 Å (IR) by varying the modulation frequency Ω_2 inversely with the number of spectral lines. A secondary constraint that the frequencies from the two modulators should be incommensurate, could have been imposed. However, to simplify the calculation, it was only required that the second frequency should be an odd multiple of 0.5 GHz. This assured that when its modes were combined with those from the 3-GHz modulator, the resultant modes would have equally spaced frequencies separated by $\Delta\Omega$ = 0.5 GHz. (The resultant modes have frequencies composed of a harmonic from one modulator plus a harmonic from the second.) Beam smoothing will then occur for averaging times up to 2 ns , which is the time required to smooth nearest neighbor modes. If longer smoothing times are applicable, then Ω_2 can be chosen so that the resultant modes are more closely spaced in frequency.

Figure 3-37 shows the effect of increasing the angular dispersion in one direction. Plotted is the rms nonuniformity for a single beam versus averaging time. Here, the rms nonuniformity is defined as the intensity fluctuation around the diffraction-limited envelope that would be produced if interference between all phase-plate elements were

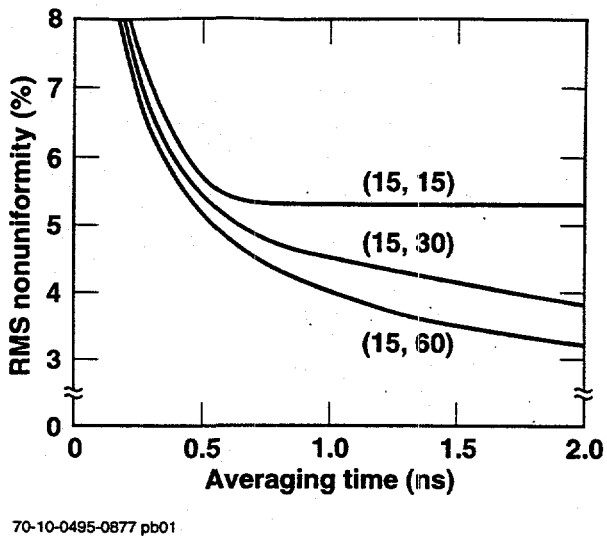

Figure 3-37. RMS nonuniformity improves as the dispersion in one direction is increased.

absent. The RMS value was evaluated at the center of the beam, over a square region given by ±0.1 times the capsule radius in each direction. This gives a good sampling of the short wavelength structure. (Long wavelength nonuniformity is more appropriately discussed in conjunction with the effects of multiple-beam overlap). The three curves in Fig. 3-37 are labeled by the angular deflection (in terms of the beam's diffraction limit) in each direction.

The single-beam results in Fig. 3-37 show that if we are only interested in averaging times less than ~500 ps, then there is not much advantage to increasing the angular dispersion. However, if averaging times of 1 ns or larger are relevant, then substantial improvements in uniformity can be achieved from increased dispersion. The majority of the effect is achieved at 30 x DL: For a 2-ns averaging time, the RMS nonuniformity is reduced by 40%, compared with the 15 x DL result. (For 60 x DL, the reduction is increased to 65%). The improved uniformity is probably the result of smoothing some of the longer wavelength nonuniformities that become accessible with increased angular dispersion. (All three cases in Fig. 3-37 use the same bandwidth.) Table 3-10 summarizes some of the SSD parameters and results.

The uniformity results for spherical illumination, using multiple beam overlap, are shown in Fig. 3-38. The beams were mapped directly onto the capsule surface, and the nonuniformity was expressed in terms of spherical harmonics for modes up to 512. No refractive smoothing or thermal smoothing in a plasma atmosphere was used, except indirectly by neglecting the very short wavelength structure with spherical harmonic modes greater than 512. Interference between the beams was not included in the calculation. This is justified for the interference between beams within a cluster and between beams from different clusters with different frequencies, as this structure will smooth within about 5 ps. Interference between beams (of the same frequency) from different

Table 3-10. Large bandwidth modulator and single-beam uniformity.

Modulation frequency (GHz)	15 X DL	30 X DL	60 X DL
Modulation frequency (GHz)	13.5	6.5	3.5
Bandwidth (Å, IR)	4.05	3.9	4.2
Single beam uniformity for Dt = 0.5 ns	5.9%	5.7%	5.4%
Single beam uniformity for Dt = 2 ns	5.3%	3.9%	3.3%

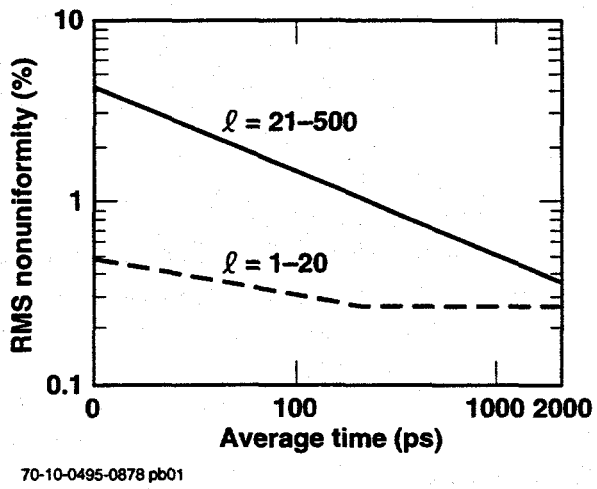

Figure 3-38. RMS nonuniformity in the high and low L-mode regions.

clusters was not considered, because this nonuniformity has spatial wavelengths that are much shorter than the minimum considered here. Such very short wavelength nonuniformity would be smoothed by thermal conduction within the capsule blow off, over distances of only a few microns.

The nonuniformity for spherical irradiation, in Fig. 3-38, has been separated into a long wavelength component, with spherical harmonic modes $L \leq 20$ (σ_L), and a shorter wavelength component with $21 < L < 512$ (σ_S). The long wavelength modes are relatively static and are dominated by the shape of the cluster intensity envelope and the number of clusters. It is possible that this component of nonuniformity could be further reduced by modifying the envelope shape as part of the phase-plate design. The shorter wavelength modes (21–512) are seen to decrease with averaging time t roughly as $t^{-1/2}$. This is the same scaling as ISI[6] and is obtained from the superposition of different random speckle patterns.

The results in Fig. 3-38 show that the direct-drive uniformity constraints can be achieved, namely: $\sigma_L < 0.5\%$ and $\sigma_s < 1\%$ at 500 ps and <0.5% at 2 ns.

3.4.5 Unconverted Light

The direct-drive target requires a wedge of angles 5.5°–6° (or some other method) in order to divert the unconverted 1ω and 2ω light away from the target.[17] It should be noted that if this wedge is made birefringent, then the polarization modes discussed above can be generated by the same optic. These diverted beams will be absorbed in specifically designed material on the chamber wall opposite to entry. Because of the larger spot size associated with direct drive (2–4 mm compared to 0.5 mm for indirect drive), it has been shown that with current phase plate designs and technology, the peak-to-average (P/A) intensity present at these absorbers will be 6:1. The present baseline calls for absorbers that tolerate 3:1 P/A. Resolving this discrepancy will require either a new phase plate design which reduce the P/A, or improved absorbers, or a redetermination of the effect of a 6:1 P/A on the operational aspects of the NIF.

3.5 Propagation and Frequency Conversion

The spatial propagation of the beams the NIF amplifiers is affected by the smoothing modulation applied to the beam (Fig. 3-39). The modulated beam will have intensity modulation in both space an time, and as a result the peak power delivered by the NIF is potentially compromised by modulation.

The modulated beam has both bandwidth and an added beam divergence associated with the additional spatial modes imposed. Bandwidth causes intensity modulation through group velocity dispersion (GVD) and the added beam divergence causes spatial and temporal intensity variations associated with nonlinear ripple growth or beam clipping in the spatial filter pinholes or a near field aperture. At low intensity, large intensity modulation is permissible without compromising the performance. However, at high intensity an additional variation in the fluence across the beam aperture increases the risk of damage and requires the total power and energy to be reduced. The power and energy on target will be a maximum if the smoothing technique uses pure phase modulation at high power.

A beam with phase modulation develops intensity modulation with propagation distance. Beams with SSD develop intensity modulation as a result of beam divergence as well as GVD in the laser glass. The dispersion relation for SSD is $ck = \omega n \cos\theta$, from which the dispersion is $ck'' = 2n' + \omega n'' - \omega n\theta'^2$. If the intensity modulation has relative amplitude R, then

$$dR/dz = \frac{1}{\pi} k'' \Delta\omega\Omega$$

$$= \frac{k}{2\pi\Gamma}\left(\frac{2n'\omega + n''\omega^2}{n}\left(\frac{\Delta\omega}{\omega}\right)^2 - \Delta\theta^2\right) \qquad (53)$$

where Ω is the RF frequency in rads/s, Γ is the depth of modulation, $\Delta\omega = 2\Gamma\Omega$ is the total bandwidth of the modulation (full width), and Δθ is the added divergence (full

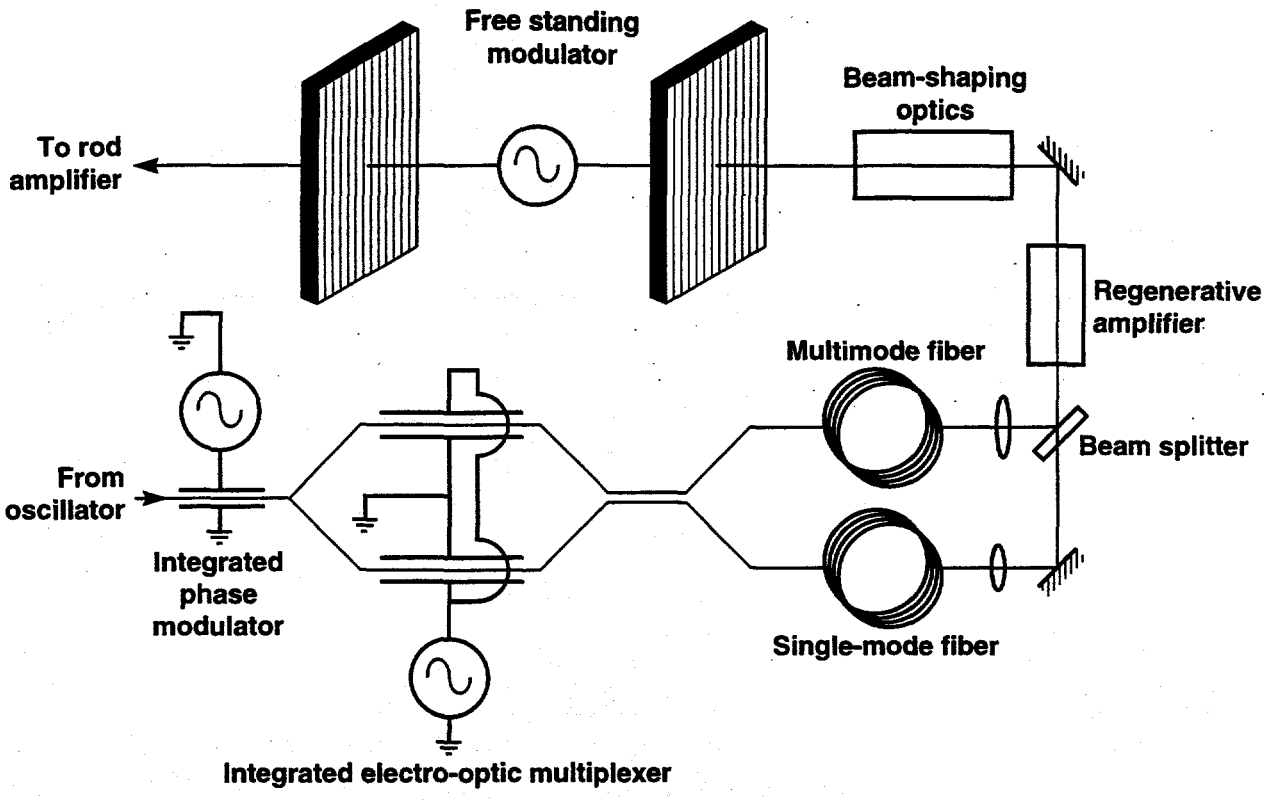

70-10-0495-0879 pb01

Figure 3-39. Integrated optical system to switch from PCL to a clean near field between the foot and main pulse. An integrated phase modulator provides bandwidth (FM or otherwise), and the electro-optic multiplexer can rapidly switch the pulse between a single mode (clean near field) and multimode (PCL) fiber channel. After recombination both channels undergo additional (1-D or 2-D) SSD to insure adequate smoothing during the main pulse.

width). For direct drive the fractional bandwidth might be 0.0005, and the added beam divergence is about 10× the diffraction limit, or about 50 μrads. Note that the first term (GVD) only applies inside an optical material, whereas the beam divergence term applies even in free space propagation. Because the optical path in the optical elements is a small fraction of the cavity length, the divergence term dominates. For a depth of modulation $\Gamma = 6$, the intensity modulation is $dR/dz = 0.0004/m$. The propagation distance in the relayed cavity is never more than the total cavity length, 45 m, for which R = 1.8%. During transport to the target chamber. The distance may be as large as 90 meters, for which R = 3.6%. Note that this modulation increases rapidly with the added beam divergence.

The intensity modulation represented by R is illustrated in Fig. 3-40. The peaks are skewed across the beam with the same time delay as the RF phase, and the modulation oscillates at the RF frequency and wavelength $2\pi c/\Omega$. Its time integral is small, therefore, it has very little direct effect on the fluence, and hence on the maximum power and

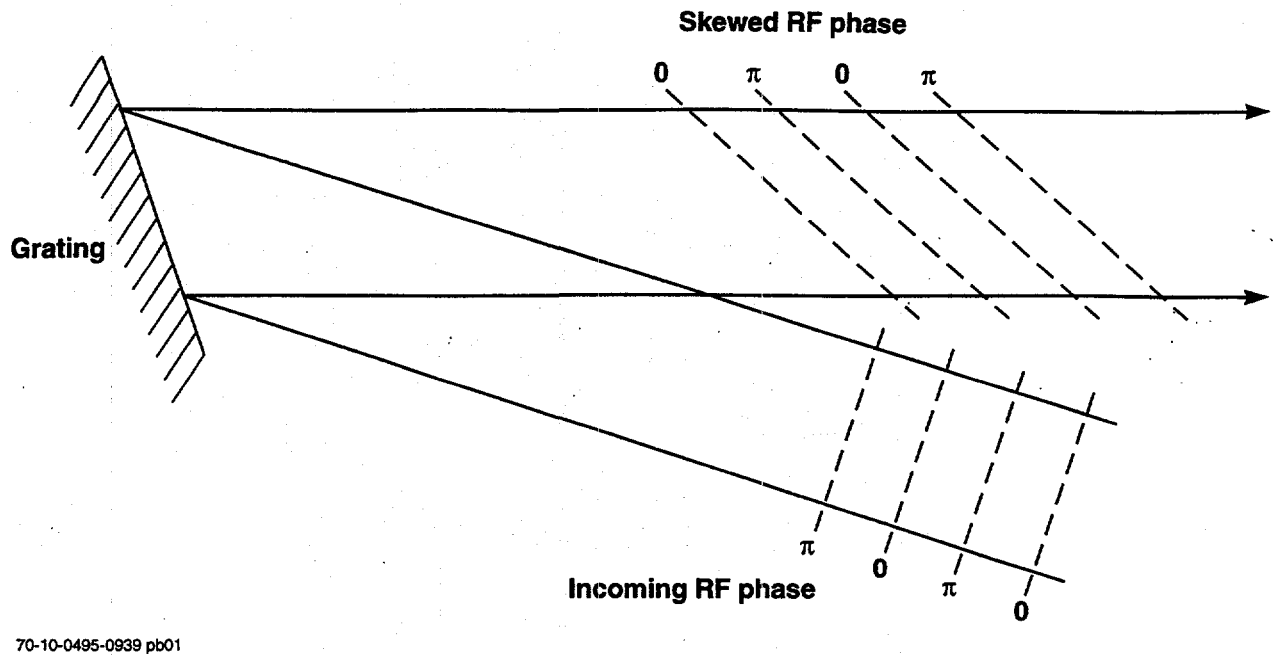

Figure 3-40. RF phase fronts in a beam diffracting off a grating are skewed. Any modulation arising from FM-to-AM conversion follows these phase fronts. The RF phase varies both transversely across the beam and longitudinally along the propagation direction.

energy. On the other hand the peaks in the local intensity are large relative to the spatial wavelength of those ripples that experience significant Bespalov-Talanov nonlinear growth. In these circumstances, the ripple growth depends on the local intensity; it varies locally over the beam aperture and in time within the pulse. Ripple growth is superlinear with intensity. The net effect of the intensity modulation is to increase the effective ripple growth. As a result, the modulation affects the local fluence indirectly through ripple growth, adversely impacting the peak power and energy. We can estimate the fluence enhancement as follows. The ripple intensity is

$$P(\vec{r},t) = SI(\vec{r},t)G[I(\vec{r},t)] \tag{54}$$

where S is the linear scatter that creates the ripple and G(I) is the nonlinear growth factor. The local intensity is

$$I(\vec{r},t) = (1+R)\left\{1+SG\left[(1+R)I_0\right]\right\}I_0 \tag{55}$$

where f = Rsin(Ωt-Qr) is the local intensity modulation, Qr is the temporal skew and I_0 is the zeroth order pulse shape, also skewed. The peak local fluence in a ripple is the time integral the local intensity. Expanding the ripple gain as a function of the intensity we find

$$F = F_0 + SG_0F_0 + \frac{1}{2}R^2S\int dt(G' I_0^2 + G'' I_0^3). \quad (56)$$

If the ripple gain is exponential, G = exp (2B I/I_0), then

$$F = F_0 + SG_0F_0 + R^2(B + B^2)SG_0F_0. \quad (57)$$

The increase in the peak fluence as a result of enhanced ripple growth is of order R^2 which is of order 0.0004 or less in the cavity. Even if the local nonlinear growth factor B is 2 or higher and the baseline ripple is 30%, the effect on the power and energy is insignificant.

A potentially more significant effect is the effect of modulation on the function of the spatial filter pinholes. The added beam divergence brings the beam closer to the edge of the pinhole and also permits partial passage of ripples at angles greater than 100 μrads that would ordinarily not pass in the absence of SSD. Both effects increase the spatial modulation at the frequency converter. Figure 3-41 is illustrative of the ripple growth in the NIF baseline. Adding 50 μrads to the beam and pinhole diameter does not increase the ripple growth; it may even reduce it. Calculations of the performance of the baseline NIF cavity with 200 μrad (full width) pinholes, using monochromatic beams offset in angle by up to 60 μrads, indicate that at about 10–12 times the diffraction limit the

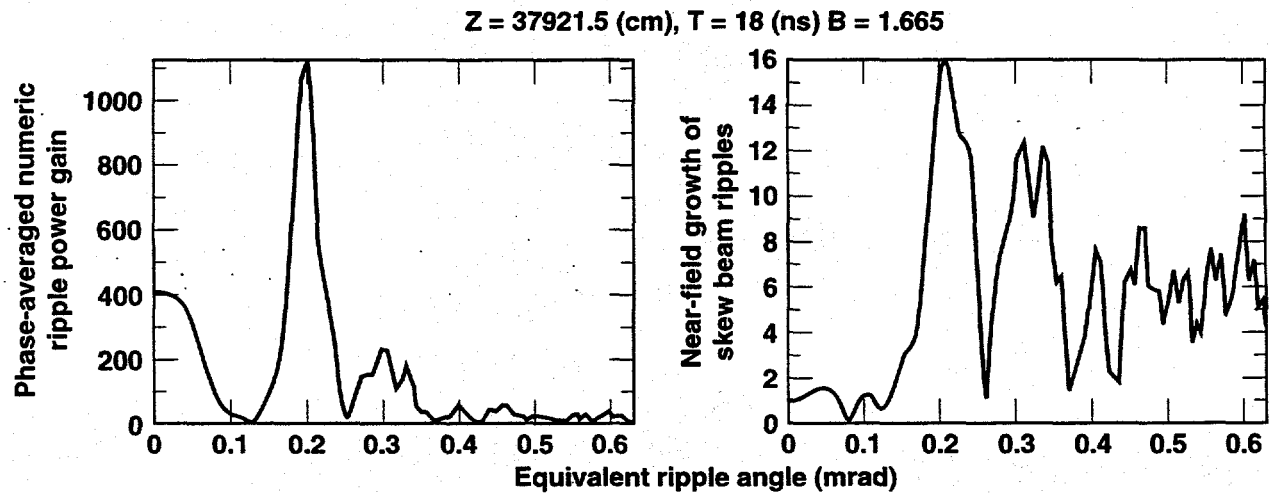

70-10-0495-0864 pb01

Figure 3-41. Calculations of the ripple growth factors in the NIF as a function of the angle of the ripple. The baseline calls for ± 100 μrad pinholes, which are well below the first peak at 200 μrad. In the 2-D SSD scheme, about 50 μrad of added beam divergence is added to the beam. If the pinholes were opened up to ±150 μrads, there would evidently be no increase in the ripple growth factors. Therefore 2-D SSD does not increase the nonlinear ripple growth.

spatial modulation on the beam begins to limit the power and energy. This calculation is conservative in that the beam energy is spread out by the added divergence rather than tilted off, and the NIF cavity may transmit beams of larger added divergence without loss. In view of the ripple growth spectrum illustrated in Fig. 3-41, this increase in spatial modulation is probably caused by linear optical effects such as pinhole clipping. It appears that the pinhole radius could be increased by up to 50 μm without exacerbating nonlinear growth. In that case, the clipping limit would move out to 100 μrad added divergence, well beyond the direct-drive smoothing requirement. These calculations suggest that the NIF cavity will indeed handle the modulated beam without loss in energy or power.

The frequency converter is sensitive to bandwidth. Figure 3-42 shows the conversion efficiency for the baseline tripler (11 mm / 9 mm) as a function of bandwidth, for a typical foot intensity (0.25 GW/cm^2) and a main pulse 1ω intensity of 3.25 GW/cm^2. At the nominal bandwidth of 160 GHz at 1ω, the conversion efficiency is substantially reduced. The energy conversion efficiency for a picket fence pulse with a temporally flat main drive, and where the peak 1ω intensity is set to 3.25 GW/cm^2, is 0.70, and falls to 0.47 at a bandwidth of 160 GHz. The peak power conversion drops from 0.88 to 0.57, over the same range. The peak power is a very significant parameter for direct-drive targets. This loss in conversion efficiency translates linearly into a reduction of about a third in peak power, which is very significant. Another feature of large bandwidth, apart from the loss in energy and power on target, is the strong power modulation that appears on the 3ω beam at the RF frequency. Such modulation is unlikely to affect the pellet hydrodynamics. It will appear on the target only if the RF spectrum across the

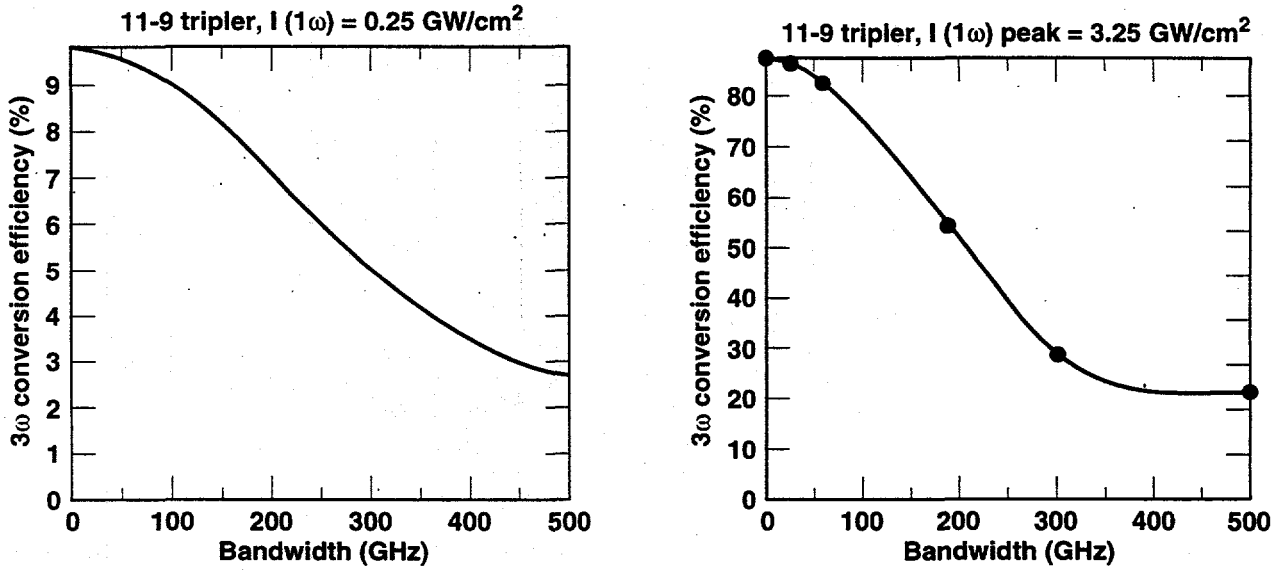

Figure 3-42. (a) Conversion efficiency of the NIF baseline tripler (10.5 mm / 8.5 mm) as a function of FM bandwidth in the foot at 0.25 GW/cm^2, (b) at 3.25 GW/cm^2.

beam aperture is not balanced. The imbalance will be small, and any residual effects will smooth out in half the modulation period; it will not affect pellet hydrodynamics for the long wavelengths that will be created.

There are several ways to recover from this loss in peak power. The first is to redesign the tripler to be thinner. With a thinner tripler, the foot converts less efficiently, but the main drive is essentially unaffected. Data[18] from experiments on a 10.5 mm/8.1 mm tripler are shown in Fig. 3-43 The peak conversion efficiency for the given pulse shape and divergence drops from over 70% to about 60%, a loss of less than 20%, a considerable improvement to the baseline. There are also other frequency conversion schemes that offer some improvements, such as high dynamic range designs that increase the conversion efficiency for the foot of the pulse without significantly compromising the conversion efficiency at its peak. One design[19] that accomplishes this is a three-crystal design with two Type I doublers arranged in an alternating-Z configuration, and a single Type II tripler. In the alternating-Z doubler configuration the z-axes of the two doublers are in equivalent directions, and their angular offsets in opposite senses. The scheme is described in Fig. 3-44. The thicknesses and angular offsets of the three crystals are listed in Table 3-11. The three lengths are L_2, L'_2, and L_3; the associated angular offsets are θ_2, θ'_2 and θ_3. Also listed are the baseline, and a thicker crystal baseline that improves low intensity conversion by sacrificing the high intensity performance. Two advanced designs are shown. The second advanced design uses deuterated crystals to offset the increase in optical absorption for thicker crystals.

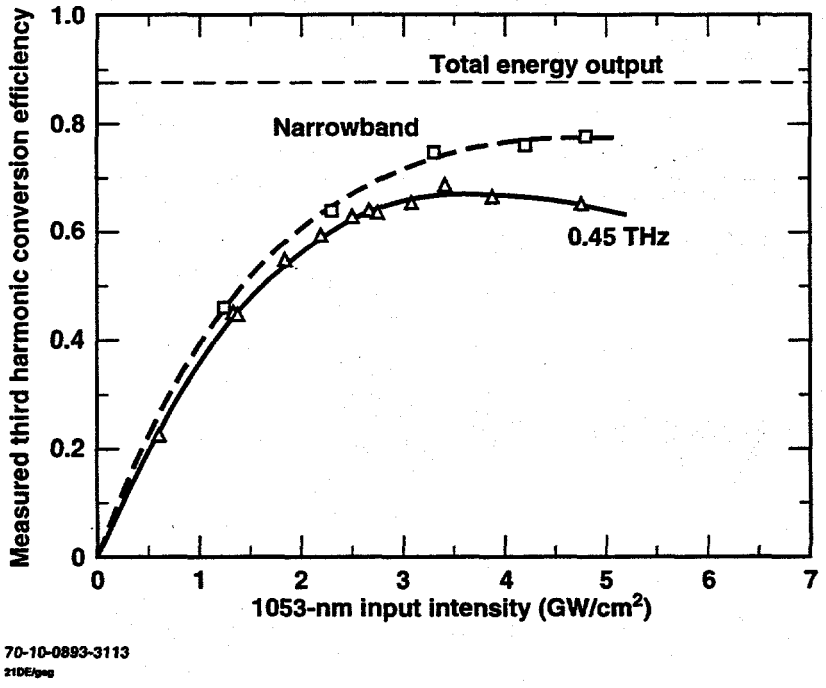

Figure 3-43. Experimental data on the conversion efficiency of a 10.5 mm/ 8.1 mm NIF-like tripler as a function of bandwidth. It shows a significant loss for 160-GHz input bandwidth.

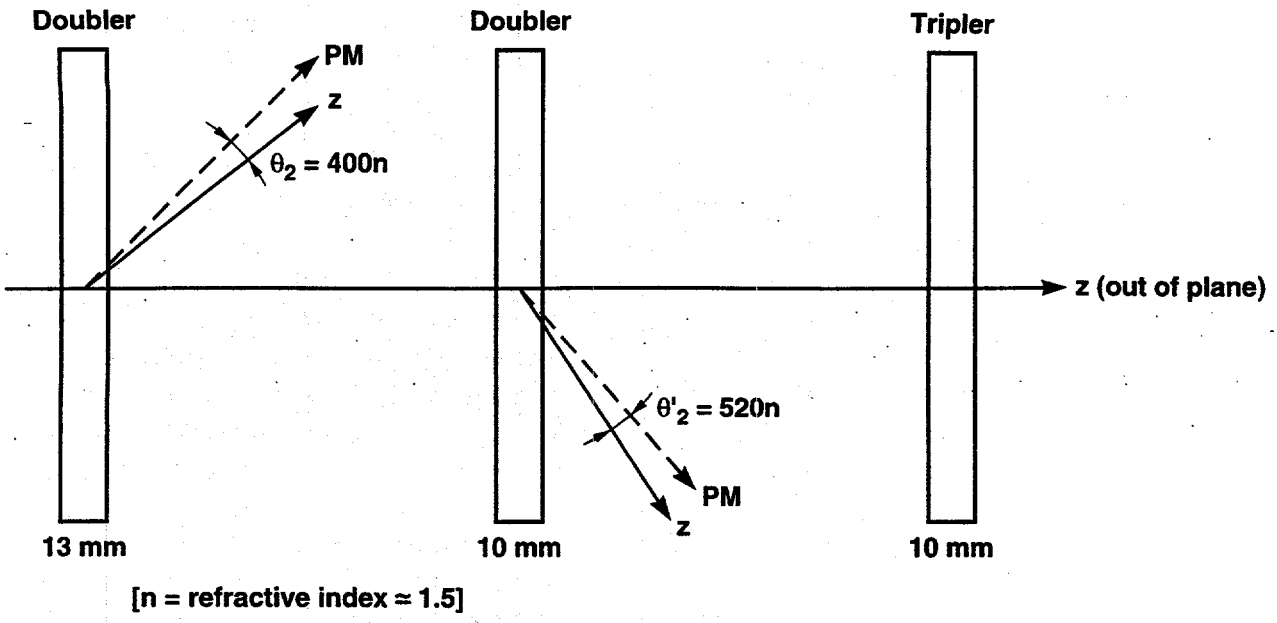

70-10-0495-0963 pb01

Figure 3-44. Three-crystal frequency convertors have higher bandwidth than the baseline design, and can potentially increase the conversion efficiency by 5% or more. The three-crystal scheme is an alternating-Z doubler pair both at large angular offset, followed by a single tripler. The alternating-Z doubler provides the correct mix ratio (2) over a larger range of intensity than the baseline does.

Table 3-11. Frequency Tripling Designs for NIF

Set	D(%)	L_2	θ_2	L'_2	θ'_2	L_3	θ_3	Efficiency
1	0	11	250	-	-	9	30	66.5
2	0	13	210	-	-	10	30	69
3	0	13	400	10	-520	13	30	74
4	70	13.5	380	10	-510	13	30	75

Units: Length in mm, Angles are internal in microradians

These designs maintain higher conversion at high bandwidth than the baseline. Figure 3-45 plots the conversion efficiency for various high dynamic range three-crystal triplers, and the baseline design; it appears to offer about a 5% improvement in conversion efficiency at high bandwidth.

There are other three-crystal tripling schemes that offer improvements in bandwidth such as single doubler followed by two triplers.[20] Calculations of these tripling schemes suggest that the single beam bandwidth can be as much as 1 THz at 3ω, with only a 5% penalty in conversion efficiency. The possibility of a system bandwidth in excess of 4 THz is exciting, and work is ongoing.

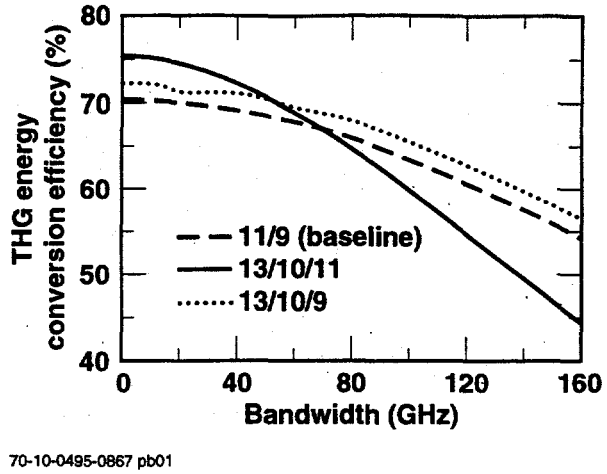

Figure 3-45. Energy conversion efficiency of the NIF baseline converter and two advanced designs shown are for the picket fence pulse shape, at peak input intensity = 3.25 GW/cm^2: NIF baseline (11/9), alternating-Z three crystal scheme (13/10/11), and alternating-Z three crystal scheme (13/10/9).

Another approach is to vary the bandwidth during the pulse. During the imprint phase, the bandwidth can be high, perhaps as much as 200 GHz (2.4 THz for a cluster of four beams at 3ω) without seriously impacting the energy efficiency. After the imprint phase the bandwidth can be reduced to about 100 GHz (1.2 THz per cluster) to allow high conversion efficiency for the main pulse, partially recovering both the energy and the peak power. This is perhaps the least expensive option for recovering from the bandwidth sensitivity of the triplers, and is attractive if it is acceptable to the target.

Figure 3-46 shows a contour plot of the peak power as a function of the bandwidth and added beam divergence. (We have assumed a thinner tripler than the baseline in anticipation of the needed redesign. The bandwidth penalty for the thinner tripler is assumed to be about half that for the baseline.) For SSD schemes, the bandwidth and added divergence are linearly related; if the bandwidth is reduced the beam divergence is also reduced. The interrelation of bandwidth and beam divergence implies that as the bandwidth is varied the added beam divergence may be different along the x- and y-directions so that beam in the pinhole may not be square. It can become a (time-dependent) rectangle. For Fig. 3-46, the relevant parameter is the maximum of the added divergences in any direction. As the bandwidth is varied, the system follows a line such as AB in Fig. 3-46. For the main pulse, the operating point should lie within a high power contour. During the foot, the peak power limits here are not the most significant, rather pinhole clipping and other linear sources of spatial modulation become important. Thus for higher bandwidth, the operating point can lie where the peak power is quite low. The key figure of merit determining allowable extent of bandwidth variation is essentially the high L-mode smoothness requirement for the main pulse. The target requirements for the main pulse alone have not yet been explored.

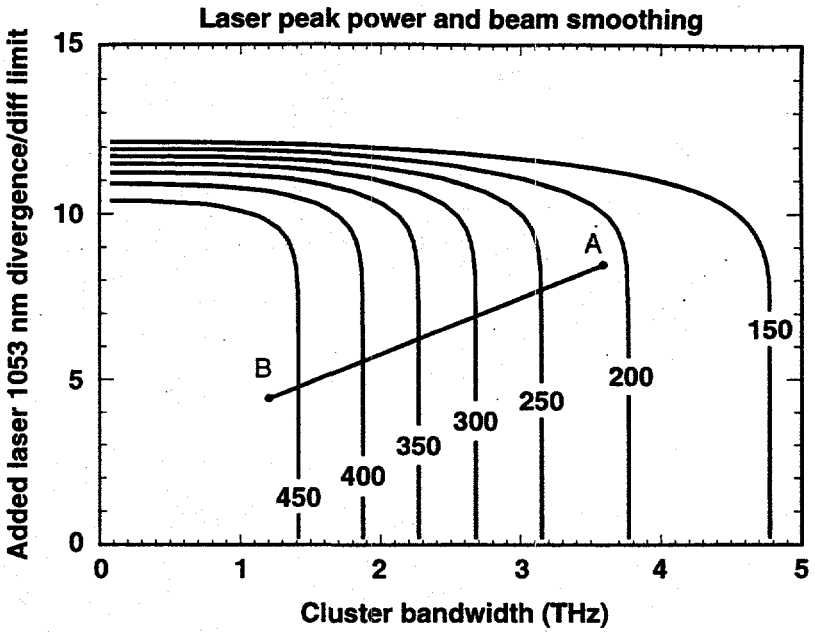

Figure 3-46. Contour plot of the peak power of the NIF as a function of the added beam divergence and the full bandwidth. The point (A) represents operation in the foot where the power is low, and point (B) represents the main pulse where the power is high. Both points assume the same laser hardware but a different bandwidth. Decreasing the bandwidth for the main pulse allows suppression of imprint without compromising the peak power in the main pulse.

4.0 Alternative Illumination Strategies

The peak power of the laser is reduced for bandwidths in excess of 2 THz, as shown in Fig. 3-46. The peak power on target can potentially be improved by reducing the size of the individual beams on the target, at a small cost in uniformity. Consider illuminating the target with beams whose size at the target plane is roughly the same as the final radius (critical surface) rather than the initial radius (solid density). Clearly much more of the laser power is absorbed by the target. In principle it is possible to envision increasing the absorption efficiency from about 35% to near 100% by decreasing the beam size. The peak power requirement on the laser would then be reduced from about 450 TW to about 150 TW. According to Fig. 3-46, this evidently permits increasing the bandwidth by as much as a factor of three, from 1.5 THz to 4.5 THz. The increased bandwidth increases the smoothing rate by about a factor of three. On the other hand, the smaller beam size decreases the number of overlapping beams. Calculations for the LLE target parameters indicate that the effective number of overlapping beams drops from 13 to 7 when the spot size is reduced to the final target radius. The smoothing rate increases by a factor of about 3, but the asymptotic level increases by about a factor of 2. The original asymptotic level can possibly be recovered by increasing the added beam divergence by about 20%, if desired. The low L-mode uniformity at early times will be increased by reducing the beam size, but it improves as the corona develops and is optimal during the main pulse. The overall nonuniformity, including the beam pointing and power balance contributions, will be only weakly affected by increasing the intrinsic nonuniformity from 0.15 to 0.3.

On balance, this strategy decreases the peak power requirement by a factor of three, but the uniformity is less strongly affected. Raising the peak power by a factor of 3 allows the adiabat to increase to counter the decrease in uniformity. By reducing the beam size, it is possible to carry out experiments on higher adiabats.

Another option is to use a time-dependent "zoom" focus to change the spot size during the pulse. The beams always match the effective target size, thereby maintaining the laser absorption efficiency. While the optical technology for "zoom" seems to present no overwhelming difficulty, this option has not received much attention to date in regard to implementation on NIF.

5.0 Primary Criteria and Functional Requirements for Direct Drive

A scientific basis for the primary criteria has been developed for direct-drive experiments. The primary criteria for direct-drive experiments at the NIF can be specified once a strategy has been selected. We have the following strategy in mind:

1. There will be a common target chamber with 72 ports. A 48-beam subset of these ports will be used for indirect-drive experiments with 2-LEH hohlraums. A different subset will be used in direct-drive experiments, and possibly a third subset for indirect-drive experiments with 4-LEH hohlraums, in that order of priority.
2. The bandwidth is adjustable between the foot and the main pulse.
3. The Front End will be made compatible today with subsequent implementation of beam modulation at a time when further technical data (such as from Nova or Omega or elsewhere) are available.

With this understanding, the primary criteria for direct drive are listed in Table 5-1, and the laser functional requirements for direct drive are listed in Table 5-2.

Table 5-1. Primary criteria for direct-drive experiments on NIF.

System parameter	
Laser pulse energy	1.5 MJ
Laser pulse peak power	450 TW
Laser wavelength	351 nm
Nonuniformity on target (All times, L-modes 1–20)	1%
Speckle smoothness (Δt = 1 ns, foot, L-modes 21-500)	1%
Speckle smoothness (Δt=1 ns, main drive pulse, L-modes 21–500)	2%
Number of full system shots	600–1200

Table 5-2. Laser system functional requirements for direct-drive experiments on NIF.

System parameter	Min	Max
Laser bandwidth (foot)	2 THz	4 THz
Laser bandwidth (main pulse)	1 THz	2 THz
Port location nonuniformity (σ_0)	-	0.2%
Beamlet power error (RMS, average over 1-ns interval)	-	5%
Beamlet positioning circle of error	-	50 μm
Added beam divergence associated with SSD	50 μrad	
Beamlet divergence at focus lens (full width, w/o SSD)	-	70 μrad
Beamlet spot size at TCC	1.0 mm	4.0 mm
Beam profile intensity error at TCC (L-modes 1-25) (relative to peak of profile)	-	4%
Laser pulse duration	-	30 ns
Laser pulse contrast ratio (main / foot)	50	200
Laser pulse background level (picket fence pulses, background /foot)	-	0.05
Laser pulse rise/fall time(10/90)	100 ps	-
Laser prepulse (-25 ns < t < 0)	-	100 mJ

Acknowledgments

The work described in this report is based on the contributions of the scientists and engineers at LLE, LLNL, NRL, and of many others to the ongoing effort in ICF. Their contribution is gratefully acknowledged. We also thank the following people who have contributed significantly to the writing of this document: Charles Verdon and Stan Skupsky, LLE; and Mike Key, Steve Weber, Josh Rothenberg, and David Eimerl, LLNL. We also thank Joy Perez for editing and reviewing the manuscript.

This work was performed under the auspices of the U.S. Department of Energy by Lawrence Livermore National Laboratory under contract No. W-7405-Eng. 48.

References

1. D. Eimerl, "Configuring NIF for Direct Drive," presentation at ICFAC meeting, 18 May 1994, University of Rochester.

2. S. W. Haan, "Onset of nonlinear saturation for Rayleigh-Taylor growth in the presence of a full spectrum of modes," *Phys. Rev* **A39**, 5812, (1989).

3. S. W. Haan, "Weakly nonlinear hydrodynamic instabilities in inertial fusion," *Phys. Fluids* **B3**, 2349,(1991).

4. S. V. Weber, "Figure of Merit for Direct Drive Ignition Targets", LLNL memorandum, March 1995.

5. D. W. Phillion and S. Pollaine, "Dynamical compensation of irradiation nonuniformities in a spherical hohlraum illuminated with tetrahedral symmetry by laser beams," *Phys. Plasmas*, **1**, 2963, (1994).

6. R. H. Lehmberg and S. P. Obenschain,"Use of induced spatial coherence for uniform illumination of laser fusion targets," *Optics Comm.* **46**, 27, (1983).

7. Y. Kato, K. Mima, N. Miyanaga, S. Arinaga, Y. Kitagawa, M. Nakatsuka, and C. Yamanaka,"Random phasing of high power lasers for uniform target acceleration and plasma-instability suppression," *Phys Rev Lett* **53**, 1057, (1984).

8. D. Veron, H. Ayral, C. Gouedard, D. Husson, J. Lauriou, O. Martin, B. Meyer, M. Rostang and C. Sauteret, "Optical Spatial Smoothing of Nd:Glass Laser Beam," *Optic Comm.* **65**, 42 (1988).

9. S. Skupsky, R. W. Short, T. Kessler, R. S. Craxton, S. Letzring, and J. M. Soures, "Improved Laser-Beam Uniformity Using the Angular Dispersion of Frequency Modulated Light," *J. Appl. Phys* **66**, 3456 (1989).

10. D. M. Pennington , "Effect of bandwidth on beam smoothing and frequency conversion at the third harmonic of the Nova laser," *Proc. Soc Photo-Opt Instrum Eng* .**1870**, 175.

11. S. Skupsky, LLE, Unpublished.

12. T. J. Kessler, Y. Lin, J. J. Armstrong, and B. Velasquez"Phase Conversion of Lasers with Low-Loss Distributed Phase Plates," in *Laser Coherence Control: Technology , and Applications*, eds. H. T. Powell and T. J. Kessler, vol **1870** p95 ff.

13. S. N. Dixit, J. K Lawson, K. R. Manes, H. T. Powell, and K. A. Nugent, "Kinoform phase plates for focal plane irradiance profile control," *Opt Lett* **19**, 417,(1994).

14. R. H. Lehmberg, A. J. Schmitt, and S. E. Bodner, "Theory of Induced Spatial Coherence", *J. Appl. Phys.* **62**, 2680 (1987).

15. J. Auerbach, LLNL, unpublished calculations.

16. S. Skupsy, LLE, unpublished.

17. J. E. Rothenberg, LLNL, unpublished.

18. D. Milam, LLNL, unpublished data.

19. D. Eimerl, LLNL, unpublished.

20. Peter Milonni, LANL, presented at the first Annual Conference on Solid-State Lasers for Application to Inertial Confinement Fusion, Paper T18.